Novel Applications of Advanced Bioimaging: Quantification of Intrathecal Solute Transport to the Brain and Magnetic Resonance Imaging of Ophthalmic Structural Changes in Long Duration Spaceflight Astronauts

A Thesis
Presented in Partial Fulfillment of the Requirements for the
Degree of Master of Science
with a
Major in Biological Engineering
in the
College of Graduate Studies
University of Idaho
by
Akari J. Seiner

Approved by:
Major Professor: Dev Shrestha, Ph.D.
Committee Members: Bryn Martin, Ph.D, Nathan Schiele, Ph.D
Department Administrator: Dev Shrestha, Ph.D.

December 2021

Abstract

The field of bioimaging science has been continually evolving over the recent years. Typically, bioimaging is used to noninvasively visualize biological processes in real time at multiple resolutions. Commonly used imaging techniques include those based in optics, photonics, magnetic resonance, spectroscopy, and others. Imaging processing and analysis are an integral part of bioimaging and allows for the quantification of anatomical and physiologically relevant parameters. In this thesis, we propose two novel applications of bioimaging: (1) quantification of intrathecal solute transport to the brain in a human model and (2) quantification of ophthalmic structural changes in long duration spaceflight astronauts. To address the first aim, a T2-weighted magnetic resonance imaging (MRI) sequence was used to acquire anatomical and cerebrospinal fluid (CSF) flow data. An optically clear 3D in vitro human model of the CSF in the subarachnoid space and subject specific oscillatory CSF flow waveforms were developed from the sequence. Several intrathecal drug delivery (ITDD) parameters, including (a) bolus volume and rate, (b) flush volume, timing, and rate, (c) injection location, and (d) type of device, were investigated. It was observed that a parametric increase in flush volume had the greatest impact on increasing solute transport to the brain. The findings of this study provide insight into the relationship between the anatomy and physiology of the CSF dynamics and ITDD injection parameters, which potentially allows for an improved detection and treatment of central nervous system disorders. To address the second aim, noninvasive MRI based techniques were developed to assess and quantify ophthalmic changes in healthy subjects under head down tilt as an analog to microgravity. This is critical as spaceflight has been shown to induce structural ophthalmic abnormalities in a condition known as Spaceflight Associated Neuro-ocular Syndrome (SANS). Prohibitive costs and physical limitations of inflight monitoring has created challenges in studying the pathology of SANS. Therefore, head down tilt (HDT) studies are currently being studied as spaceflight analogues due to its ability to simulate similar fluid redistributions observed in microgravity. In this study, HDT studies were used to quantify structural ophthalmic changes. Specifically, the following changes were quantified: (a) change in optic nerve sheath (ONS) and optic nerve (ON) cross sectional area, (b) change in ON deviation, (c) change in vitreous chamber depth, (d) an estimated Young's modulus, and (e) change in posterior globe volume displacement. The findings observed suggest that the CSF pressure was elevated in the bulbar subarachnoid space; however, the non-linear behavior of the soft tissue suggests that further increases in pressure may not lead to further ophthalmic changes. Furthermore, the effect of centrifugation as a countermeasure was investigated and no significant difference between the treatment groups was observed, suggesting that mitigation techniques may not be sufficient to reduce the severity of SANS.

Acknowledgments

I would like to dedicate my first thanks to both of my advisors, Dr. Dev Shrestha and Dr. Bryn Martin, for providing me with the opportunity to pursue these projects. Both have provided nothing but support, mentorship, and leadership that has allowed me to grow into a better engineer, researcher, and person. I am incredibly grateful for the opportunity to explore the realms of both Spaceflight Associated Neuro-ocular Syndrome and intrathecal drug distribution to the brain, as I feel diving into both projects has allowed me to learn so much more than I could have ever asked for. I owe you both so much for allowing my career to reach this point.

I would like to extend a special thanks to my final committee member, Dr. Nathan Schiele, for your time, support, and feedback throughout this entire process. I feel eternally thankful that I had the chance to learn from you, both inside the classroom and out, as you have taught me so much.

I would also like to thank everyone – past and present – in my lab for everything that they have contributed to allow me to stand where I am today. Particularly, Stuart Sater and Gabryel Natividad Conley for helping me hit the ground running on my first project at the university. Additionally, Goutham Burla and Ahmad Hammad for guiding me through the transition to my final project at the university and always providing me with constructive criticism and support throughout my time here. I would also like to thank Mohammadreza Khani and Lucas Sass for all their hard work and dedication during their time at the lab.

I would also like to extend a thanks to all of the collaborators that have made these projects possible including: Josh Horvath, Sabrina Wong, Mayumi Bowen, Brandon Macias, Michael Stenger, Karina Marshall-Goebel, Steve Laurie, C. Ross Ethier, John Oshinski, and Eric Bershad.

Finally, I would like to thank everyone who has provided me personally with endless support. I would like to thank my family: my mother, Noriko, for teaching me perseverance and dedication, my brother, Jason, for always challenging me and pushing me to be a better person, and my father, Yan, for instilling an excitement for math and science from a young age. I would also like to thank my best friends: Emily Locke, for always being there to answer the phone at any day and any time and for standing by my side for the last 17 years; Mandy Kiger, for always being excited to spitball ideas relating to engineering and science, for always hopping on a six hour Zoom call to listen to my rants and watch random shows (and occasionally study); Carson Silsby, for providing me with love and support throughout both my undergraduate and graduate degrees, for always having in depth, random conversations, and for always managing to put a smile on my face; and Ludwig Avendano,

for being my shoulder to lean on, for always providing memes at a moment’s notice to make me laugh, and for being a constant, never-ending source of love and support over the last several years. Lastly, I want to thank my beloved, Fox Avery, for the endless encouragement sparked by an equal share of excitement for the field of biomedical engineering, for being my rock, my best friend, and my everything through even the most challenging of times.

Dedication

I would like to dedicate this work to my mother, Noriko, who has always encouraged me to transcend boundaries and believe in myself, just like she did. She raised me immersed in language and culture: teaching me how to think differently, to be comfortable in an unfamiliar place, to adapt quickly, to ask questions without judging, to act with humility and humor, and to look at a problem from different perspectives to seek the best solution. I would not be where I am and who I am without her. I can only hope that someday I am as caring, kind, and heroic as she is.

Table of Contents

List of Tables

List of Figures

Statement of Contribution

This thesis consists of three multi-authored articles (Chapters 2, 4, and 5). For Chapter 2, Akari modified and reassembled the human model in vitro set up, including improving the lighting and camera set up. Additionally, she conducted all calibrations and experiments and analyzed all data in the study. She also took the lead role in the drafting of the manuscript for Chapter 2. For Chapter 4 and 5, she conducted data analysis, including radial reslicing, and point cloud and alignment plot generation. She also quantified posterior globe displacement and assisted in critical discussions for the data analysis of both studies. Critical revisions to both manuscripts in Chapters 4 and 5 were also carried out by Akari.

Chapter 1: Introduction to Intrathecal Drug Delivery for Central Nervous System Diseases

Cerebrospinal fluid (CSF) is a clear, colorless fluid that occupies the subarachnoid space (SAS) and the ventricular system in the brain. [1,2] It maintains central nervous system (CNS) homeostasis providing structural protection, immunological support, stabilization of the intracranial pressure, and transportation of nutrients and neurotransmitters across the CNS. [3–5] A detailed understanding of CSF dynamics is critical for the continued investigation of central nervous system (CNS) diseases such as multiple sclerosis, [6,7] cerebral ischemia, [8,9] traumatic brain injury, [10] subarachnoid hemorrhage, [11] Alzheimer disease, [12] hydrocephalus, [13,14] Chiari malformation, [15–17] and syringomyelia. [18,19]

1.1 Function of Cerebrospinal Fluid

CSF serves several functions in the intracranial and spinal space, including: a) support, b) protection, c) homeostasis, d) nutrition, and e) immune function. [20] First, CSF provides support to the brain, estimated to be approximately 1400-1500 g in an adult human by suspending it in neutral buoyancy. [20,21] This reduces the effective weight of the brain by 28X to approximately 25-50 g. [3,20] CSF also acts as a shock absorber and a cushion by preventing the brain from hitting the skull under trauma. [3,20] Furthermore, CSF provides additional protection in terms of regulating intracranial pressure (ICP): intracranial CSF volume adapts in response to changes in intracranial brain and blood volumes caused by obstructed venous outflow and/or expanding mass lesions and normalizes ICP. [3,22]

A second critical function of CSF is its role in maintaining metabolic, immunological, and biochemical homoeostasis. Nutrients such as glucose, proteins, lipids, electrolytes are transported to glial cells, in addition to neurotransmitters, hormones, and other biological substances, are transported throughout the CNS by the CSF. [3,23,24] Mononuclear and immunoglobulins are contained within the CSF and help to maintain immunological support. [20] Biochemical constituents maintain osmotic pressure and thereby normalize CSF pressure. [20] Biochemical waste products that cannot be removed through the blood brain barrier diffuse into the CSF are removed as the CSF is reabsorbed. [20,25–27]

1.2 Cerebrospinal Fluid Anatomy and Circulation

An overview of the CSF anatomy and circulation path can be seen in Figure 1. The key features to note include the subarachnoid space, arachnoid granulations, superior sagittal sinus, and the ventricular system. The subarachnoid space exists between the arachnoid membrane and the pia mater and is made up of a network of spiderweb like connective tissue that allows for the flow of

CSF. [28,29] Arachnoid granulations are growths into the superior sagittal sinus and provides a mean for which the CSF enters the venous system from the subarachnoid space. [28,30]

The four ventricles of the brain are lined by highly vascular ependymal cells that form a structure referred to as the choroid plexus. The four ventricles include the right and left lateral ventricles, third ventricle, and the fourth ventricle. The right and left lateral ventricles extend into the frontal, occipital, and temporal lobes of their respective hemispheres. The lateral ventricles are connected to the third ventricles via the foramen of Monro; the third ventricle is connected to the fourth ventricle via the cerebral aqueduct. The fourth ventricle drains into the spinal canal and the subarachnoid cisterns. [3]

According to a classical hypothesis, [25,31–33] CSF is primarily produced by the choroid plexus and follows the pathway connecting the ventricles of the brain: CSF flows from the lateral ventricles through the foramina of Monro to the third ventricles and then through the cerebral aqueduct to the fourth ventricle (Figure 1-1). [34] CSF then exits the ventricular system through the median aperture into the subarachnoid space and continues to move both inferiorly to the central canal of the spinal cord and superiorly to the arachnoid granulations in the superior sagittal sinus, where it enters the venous system. [35]

The CSF total volume in healthy adult humans has been reported to be approximately 150 mL by several medical textbooks [25,31,36–38] and review articles, [39] and is so standard that references are often omitted. [3,36,37] Many of the earlier studies investigated CSF total volume postmortem using crude, invasive, and inaccurate methods. [40–42] Perhaps due to the recent methods utilizing noninvasive, high resolution magnetic resonance imaging (MRI) techniques, [3] recent studies have reported higher CSF total volume, ranging from 250 – 400 mL. [36,43–46]

1.3 Cerebrospinal Fluid Pulsations

Phase contrast MRI has helped advance the study of CSF flow. It has been suggested that both the cardiac and respiratory cycles play a key role as CSF flow drivers by inducing a change in brain volume. [47–55] Several studies have found that CSF appears to move craniocaudally during cardiac systole and in the reverse direction during diastole [56–58] and a study by Mestre et al. found that the CSF flow is more closely aligned with the cardiac cycle than the respiratory cycle. [59] Other studies have investigated the impact of the respiratory cycle and found that deep inhalation and exhalation have a significant effect on thoracic pressure that is transmitted to the intracranial space. [4,52,53,60,61]

1.4 In Vivo Analysis of Cerebrospinal Fluid Dynamics

Lumbar punctures have been used to diagnose and treat certain conditions. A hollow needle is inserted through an area of numbed skin into the subarachnoid space of the lumbar region in the spine and withdraws CSF or injects a medication while the patient typically orients themselves in laterally. Lumbar punctures are typically used to test for appearance, total protein, white blood cell, glucose, and microorganism count, in addition to cancer cells. The same procedure can be conducted to treat a condition by delivering medication to the lumbar region of the spinal cord via a hollow needle, which has been increasingly investigated in drug delivery methods such as intrathecal.

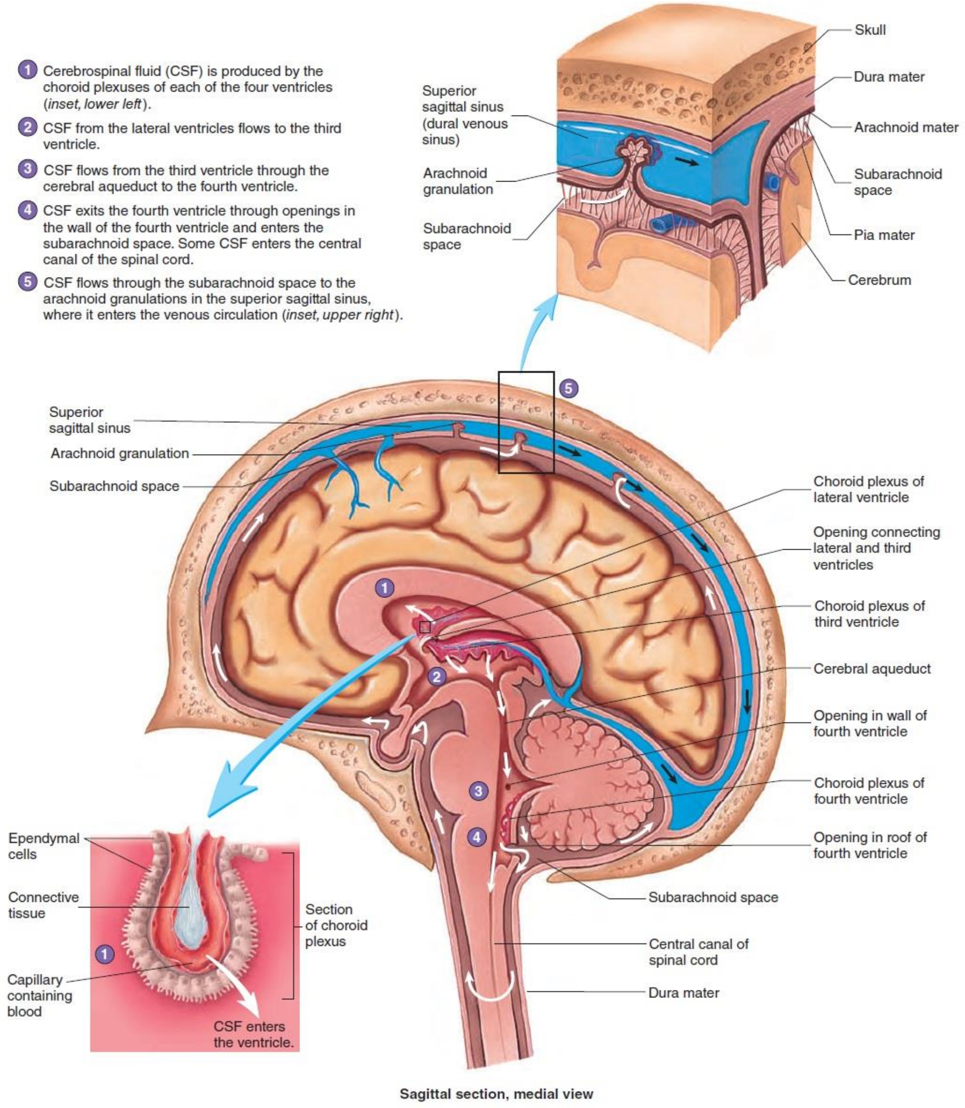

① Cerebrospinal fluid (CSF) is produced by the choroid plexuses of each of the four ventricles (*inset, lower left*).

② CSF from the lateral ventricles flows to the third ventricle.

③ CSF flows from the third ventricle through the cerebral aqueduct to the fourth ventricle.

④ CSF exits the fourth ventricle through openings in the wall of the fourth ventricle and enters the subarachnoid space. Some CSF enters the central canal of the spinal cord.

⑤ CSF flows through the subarachnoid space to the arachnoid granulations in the superior sagittal sinus, where it enters the venous circulation (*inset, upper right*).

CSF enters the ventricle.

Figure 1-1. Flow path of CSF. White arrows indicate the direction of CSF flow; black arrows indicate the direction of blood flow. Key features include the choroid plexus, subarachnoid space, and the arachnoid granulations. (Essentials of Anatomy and Physiology: Nervous System : Cerebrospinal fluid - Nervous System)

MRI has been used to quantify CSF dynamics in vivo. Currently, four-dimensional phase contrast MRI is used to measure the velocity of CSF in three dimensions over an entire volume. [15,62] The cerebral aqueduct has been found to have the highest peak velocity ranging from 4 – 20 cm/s in healthy adults. [14,63] In the spinal SAS, the peak CSF velocities ranging from 2 – 20 cm/s occur in the cervical spine. [3]

1.5 Solute Transport via Intrathecal Drug Delivery

When a solute is injected into the spinal SAS during intrathecal drug delivery (ITDD), it mixes with CSF and allows for bypassing of the blood brain barrier, which typically renders drugs delivered through the vascular system ineffective. [64–68] This method may also lead to lower doses, thereby decreasing side effects and drug toxicity, compared to conventional medication delivery methods. [65,69–72] Furthermore, it is considered a simpler surgical intervention compared to convection-enhanced drug delivery, deep brain stimulation, and intracerebroventricular. [3,73]

CSF solute transport has been investigated in several studies. Studies have found strong evidence that therapeutic proteins with large biomolecules may be ideal for ITDD. [65] Several animal studies have shown that ITDD has the potential to deliver solutes to the brain parenchyma [65,74–77] and direct measurements and noninvasive imaging techniques have been used to evaluate the pharmacokinetics and bioavailability of therapeutic enzymes. [78] Morphine, Ziconotide, and Baclofen have been recently approved by the Food and Drug Administration for delivery via the intrathecal route. [72] Nusinersen, a drug administered intrathecally, was recently approved to treat spinal muscular atrophy, a rare neuromuscular disorder. [79–81] There are also several ongoing clinical trials investigating the effect of intrathecal chemotherapy, [82–84] stem cell therapy, [85–91] and gene therapy. [92]

1.6 References

1. Khani, M. *et al.* In vitro and numerical simulation of blood removal from cerebrospinal fluid: Comparison of lumbar drain to Neurapheresis therapy. *Fluids and Barriers of the CNS* **17**, (2020).

2. Wright, B. L. C., Lai, J. T. F. & Sinclair, A. J. Cerebrospinal fluid and lumbar puncture: A practical review. *Journal of Neurology* vol. 259 (2012).

3. Martin, B. A. & Heidari Pahlavian, S. Anatomy and Physiology of Cerebrospinal Fluid Dynamics. in *Nervous System Drug Delivery: Principles and Practice* 73–89 (Elsevier, 2019). doi:10.1016/B978-0-12-813997-4.00005-0.

4. Yildiz, S. *et al.* Quantifying the influence of respiration and cardiac pulsations on cerebrospinal fluid dynamics using real-time phase-contrast MRI. *Journal of Magnetic Resonance Imaging* **46**, 431–439 (2017).

5. Wang, C. X. *et al.* Cerebrospinal fluid: Physiology, biomarker and methodology. in *Cerebrospinal Fluid: Functions, Composition and Disorders* (2012).

6. Freedman, M. S. *et al.* Recommended standard of cerebrospinal fluid analysis in the diagnosis of multiple sclerosis: A consensus statement. *Archives of Neurology* vol. 62 (2005).

7. Hatterer, E., Touret, M., Belin, M. F., Honnorat, J. & Nataf, S. Cerebrospinal fluid dendritic cells infiltrate the brain parenchyma and target the cervical lymph nodes under neuroinflammatory conditions. *PLoS ONE* **3**, (2008).

8. Simon, M. J. & Iliff, J. J. Regulation of cerebrospinal fluid (CSF) flow in neurodegenerative, neurovascular and neuroinflammatory disease. *Biochimica et Biophysica Acta - Molecular Basis of Disease* vol. 1862 (2016).

9. Hårdemark, H. G. *et al.* Neuron-specific enolase is a marker of cerebral ischemia and infarct size in rat cerebrospinal fluid. *Stroke* **19**, (1988).

10. Zetterberg, H., Smith, D. H. & Blennow, K. Biomarkers of mild traumatic brain injury in cerebrospinal fluid and blood. *Nature Reviews Neurology* **9**, (2013).

11. Klimo, P., Kestle, J. R. W., Macdonald, J. D. & Schmidt, R. H. Marked reduction of cerebral vasospasm with lumbar drainage of cerebrospinal fluid after subarachnoid hemorrhage. *Journal of Neurosurgery* **100**, (2004).

12. Weller, R. O. Pathology of cerebrospinal fluid and interstitial fluid of the CNS: Significance for alzheimer disease, prion disorders and multiple sclerosis. *Journal of Neuropathology and Experimental Neurology* **57**, (1998).

13. Bradley, W. G., Kortman, K. E. & Burgoyne, B. Flowing cerebrospinal fluid in normal and hydrocephalic states: Appearance on MR images. *Radiology* **159**, (1986).

14. Bradley, W. G. *et al.* Normal-pressure hydrocephalus: Evaluation with cerebrospinal fluid flow measurements at MR imaging. *Radiology* **198**, (1996).

15. Bunck, A. C. *et al.* Magnetic resonance 4D flow characteristics of cerebrospinal fluid at the craniocervical junction and the cervical spinal canal. *European Radiology* **21**, (2011).

16. Shaffer, N. *et al.* Cerebrospinal fluid flow impedance is elevated in type i chiari malformation. *Journal of Biomechanical Engineering* **136**, (2014).

17. Shaffer, N., Martin, B. & Loth, F. Cerebrospinal fluid hydrodynamics in type I chiari malformation. *Neurological Research* vol. 33 (2011).

18. Clarke, E. C., Stoodley, M. A. & Bilston, L. E. Changes in temporal flow characteristics of CSF in Chiari malformation Type I with and without syringomyelia: Implications for theory of syrinx development - Clinical article. *Journal of Neurosurgery* **118**, (2013).

19. Stoodley, M. A., Gutschmidt, B. & Jones, N. R. Cerebrospinal fluid flow in an animal model of noncommunicating syringomyelia. *Neurosurgery* **44**, (1999).

20. Adigun, O. O. & Al-Dhahir, M. A. *Anatomy, Head and Neck, Cerebrospinal Fluid*. *StatPearls* (2019).

21. Wright, E. M. The Concept of a Blood-Brain Barrier. Michael Bradbury . *The Quarterly Review of Biology* **55**, (1980).

22. Mokri, B. The Monro-Kellie hypothesis: Applications in CSF volume depletion. *Neurology* vol. 56 (2001).

23. Johnston, M., Zakharov, A., Koh, L. & Armstrong, D. Subarachnoid injection of Microfil reveals connections between cerebrospinal fluid and nasal lymphatics in the non-human primate. *Neuropathology and Applied Neurobiology* **31**, (2005).

24. Knigge, K. M. *et al.* Role of the Ventricular System in Neuroendocrine Processes: Synthesis and Distribution of Thyrotropin Releasing Factor (TRF) in the Hypothalamus and Third Ventricle. *Canadian Journal of Neurological Sciences / Journal Canadien des Sciences Neurologiques* **1**, (1974).

25. Davson, H., Segal, M. B. Physiology of the CSF and blood-brain-barriers. *Diabetes Care* **33**, (1995).

26. Segal, M. B. & Pollay, M. The secretion of cerebrospinal fluid. *Experimental Eye Research* **25**, (1977).

27. Segal, M. B. Extracellular and cerebrospinal fluids. *Journal of Inherited Metabolic Disease* **16**, (1993).

28. Shafique, S. & Rayi, A. *Anatomy, Head and Neck, Subarachnoid Space*. *StatPearls* (2020).

29. Mortazavi, M. M. *et al.* Subarachnoid Trabeculae: A Comprehensive Review of Their Embryology, Histology, Morphology, and Surgical Significance. *World Neurosurgery* vol. 111 (2018).

30. Chin, S. C. *et al.* Giant arachnoid granulation mimicking dural sinus thrombosis in a boy with headache: MRI. *Neuroradiology* **40**, (1998).

31. CSERR, H. F. Role of Secretion and Bulk Flow of Brain Interstitial Fluid in Brain Volume Regulation. *Annals of the New York Academy of Sciences* **529**, (1988).

32. Cushing, H. Studies on the Cerebro-Spinal Fluid : I. Introduction. *Journal of Medical Research* 1–19 (1914).

33. DANDY, W. E. EXPERIMENTAL HYDROCEPHALUS. *Annals of Surgery* **70**, (1919).

34. Khasawneh, A., Garling, R. & Harris, C. Cerebrospinal fluid circulation: What do we know and how do we know it? *Brain Circulation* **4**, (2018).

35. Brinker, T., Stopa, E., Morrison, J. & Klinge, P. A new look at cerebrospinal fluid circulation. *Fluids and Barriers of the CNS* vol. 11 (2014).

36. Levi Chazen, J. *et al.* Automated segmentation of MR imaging to determine normative central nervous system cerebrospinal fluid volumes in healthy volunteers. *Clinical Imaging* **43**, (2017).

37. Sass, L. R. *et al.* A 3D subject-specific model of the spinal subarachnoid space with anatomically realistic ventral and dorsal spinal cord nerve rootlets. *Fluids and Barriers of the CNS* **14**, (2017).

38. Guyton, A. C. & Hall, J. E. *TextBook in Medical Physiology*. *Textbook of Medical Physiology* (2006).

39. Johanson, C. E. *et al.* Multiplicity of cerebrospinal fluid functions: New challenges in health and disease. *Cerebrospinal Fluid Research* vol. 5 (2008).

40. Last, R. J. & Tompsett, D. H. Casts of the cerebral ventricles. *British Journal of Surgery* **40**, (1953).

41. Wyper, D. J., Pickard, J. D. & Matheson, M. Accuracy of ventricular volume estimation. *Journal of Neurology Neurosurgery and Psychiatry* **42**, (1979).

42. Grant, R. *et al.* Human cranial CSF volumes measured by MRI: Sex and age influences. *Magnetic Resonance Imaging* **5**, (1987).

43. Hodel, J. *et al.* Imaging of the entire cerebrospinal fluid volume with a multistation 3D SPACE MR sequence: Feasibility study in patients with hydrocephalus. *European Radiology* **23**, (2013).

44. Courchesne, E. *et al.* Normal brain development and aging: Quantitative analysis at in vivo MR imaging in healthy volunteers. *Radiology* **216**, (2000).

45. Coffey, C. E. *et al.* Sex differences in brain aging: A quantitative magnetic resonance imaging study. *Archives of Neurology* **55**, (1998).

46. Pfefferbaum, A. *et al.* A Quantitative Magnetic Resonance Imaging Study of Changes in Brain Morphology from Infancy to Late Adulthood. *Archives of Neurology* **51**, (1994).

47. Rennels, M. L., Gregory, T. F., Blaumanis, O. R., Fujimoto, K. & Grady, P. A. Evidence for a "Paravascular" fluid circulation in the mammalian central nervous system, provided by the rapid distribution of tracer protein throughout the brain from the subarachnoid space. *Brain Research* **326**, (1985).

48. Hadaczek, P. *et al.* The "Perivascular Pump" Driven by Arterial Pulsation Is a Powerful Mechanism for the Distribution of Therapeutic Molecules within the Brain. *Molecular Therapy* **14**, (2006).

49. Iliff, J. J. *et al.* Cerebral arterial pulsation drives paravascular CSF-Interstitial fluid exchange in the murine brain. *Journal of Neuroscience* **33**, (2013).

50. Arbel-Ornath, M. *et al.* Interstitial fluid drainage is impaired in ischemic stroke and Alzheimer's disease mouse models. *Acta Neuropathologica* **126**, (2013).

51. Bedussi, B., Almasian, M., de Vos, J., VanBavel, E. & Bakker, E. N. T. P. Paravascular spaces at the brain surface: Low resistance pathways for cerebrospinal fluid flow. *Journal of Cerebral Blood Flow and Metabolism* **38**, (2018).

52. Yamada, S. *et al.* Influence of respiration on cerebrospinal fluid movement using magnetic resonance spin labeling. *Fluids and Barriers of the CNS* **10**, (2013).

53. Dreha-Kulaczewski, S. *et al.* Inspiration is the major regulator of human CSF flow. *Journal of Neuroscience* **35**, (2015).

54. Avezaat, C. J. J., van Eijndhoven, J. H. M. & Wyper, D. J. Cerebrospinal fluid pulse pressure and intracranial volume-pressure relationships. *Journal of Neurology, Neurosurgery and Psychiatry* **42**, (1979).

55. Portnoy, H. D., Chopp, M., Branch, C. & Shannon, M. B. Cerebrospinal fluid pulse waveform as an indicator of cerebral autoregulation. *Journal of Neurosurgery* **56**, (1982).

56. Enzmann, D. R. & Pelc, N. J. Normal flow patterns of intracranial and spinal cerebrospinal fluid defined with phase-contrast cine MR imaging. *Radiology* **178**, (1991).

57. Greitz, D., Franck, A. & Nordell, B. On the pulsatile nature of intracranial and spinal CSF-circulation demonstrated by MR imaging. *Acta Radiologica* **34**, (1993).

58. Nitz, W. R. *et al.* Flow dynamics of cerebrospinal fluid: Assessment with phase-contrast velocity MR imaging performed with retrospective cardiac gating. *Radiology* **183**, (1992).

59. Mestre, H. *et al.* Flow of cerebrospinal fluid is driven by arterial pulsations and is reduced in hypertension. *Nature Communications* **9**, (2018).

60. Williams, B. Simultaneous cerebral and spinal fluid pressure recordings - I. Technique, physiology, and normal results. *Acta Neurochirurgica* **58**, (1981).

61. Chen, L., Beckett, A., Verma, A. & Feinberg, D. A. Dynamics of respiratory and cardiac CSF motion revealed with real-time simultaneous multi-slice EPI velocity phase contrast imaging. *NeuroImage* **122**, (2015).

62. Heidari Pahlavian, S. *et al.* Accuracy of 4D Flow Measurement of Cerebrospinal Fluid Dynamics in the Cervical Spine: An In Vitro Verification Against Numerical Simulation. *Annals of Biomedical Engineering* **44**, (2016).

63. Kurtcuoglu, V. *et al.* Computational investigation of subject-specific cerebrospinal fluid flow in the third ventricle and aqueduct of Sylvius. *Journal of Biomechanics* **40**, (2007).

64. Papisov, M. I., Belov, V. v. & Gannon, K. S. Physiology of the intrathecal bolus: The leptomeningeal route for macromolecule and particle delivery to CNS. *Molecular Pharmaceutics* **10**, (2013).

65. Calias, P., Banks, W. A., Begley, D., Scarpa, M. & Dickson, P. Intrathecal delivery of protein therapeutics to the brain: A critical reassessment. *Pharmacology and Therapeutics* vol. 144 (2014).

66. Pizzichelli, G. *et al.* Numerical study of intrathecal drug delivery to a permeable spinal cord: effect of catheter position and angle. *Computer Methods in Biomechanics and Biomedical Engineering* **20**, (2017).

67. Verma, A. *et al.* Intrathecal 99mTc-DTPA imaging of molecular passage from lumbar cerebrospinal fluid to brain and periphery in humans. *Alzheimer's and Dementia: Diagnosis, Assessment and Disease Monitoring* **12**, (2020).

68. Brumback, R. A. Book Reviews: The Physiology and Pathophysiology of the Cerebrospinal Fluid, by H. Davson, K. Welch, and M.B. Segal. Published in 1987 by Churchill Livingstone Inc, New York, 1013 pages, $198.00. *Journal of Child Neurology* **3**, (1988).

69. Soderquist, R. G. & Mahoney, M. J. Central nervous system delivery of large molecules: Challenges and new frontiers for intrathecally administered therapeutics. *Expert Opinion on Drug Delivery* vol. 7 (2010).

70. Gulur, P., Bhatia, G., Lau, M. E. & Koury, K. M. Intrathecal Drug Delivery (ITDD) systems for cancer pain. *F1000Research* **2**, (2014).

71. Simpson, K. H. & Jones, I. Intrathecal drug delivery for management of cancer and noncancer pain. *Journal of Opioid Management* vol. 4 (2008).

72. Bottros, M. M. & Christo, P. J. Current perspectives on intrathecal drug delivery. *Journal of Pain Research* vol. 7 (2014).

73. Belov, V. *et al.* Large-Volume Intrathecal Administrations: Impact on CSF Pressure and Safety Implications. *Frontiers in Neuroscience* **15**, (2021).

74. Calias, P. *et al.* CNS penetration of intrathecal-lumbar idursulfase in the monkey, dog and mouse: Implications for neurological outcomes of lysosomal storage disorder. *PLoS ONE* **7**, (2012).

75. Kakkis, E. *et al.* Intrathecal enzyme replacement therapy reduces lysosomal storage in the brain and meninges of the canine model of MPS I. *Molecular Genetics and Metabolism* **83**, (2004).

76. Dickson, P. *et al.* Intrathecal enzyme replacement therapy: Successful treatment of brain disease via the cerebrospinal fluid. *Molecular Genetics and Metabolism* **91**, (2007).

77. Hemsley, K. M. *et al.* Effect of cisternal sulfamidase delivery in MPS IIIA Huntaway dogs-A proof of principle study. *Molecular Genetics and Metabolism* **98**, (2009).

78. Xie, H., Chung, J. K., Mascelli, M. A. & McCauley, T. G. Pharmacokinetics and bioavailability of a therapeutic enzyme (idursulfase) in cynomolgus monkeys after intrathecal and intravenous administration. *PLoS ONE* **10**, (2015).

79. Neil, E. E. & Bisaccia, E. K. Nusinersen: A novel antisense oligonucleotide for the treatment of spinal muscular atrophy. *Journal of Pediatric Pharmacology and Therapeutics* vol. 24 (2019).

80. Claborn, M. K., Stevens, D. L., Walker, C. K. & Gildon, B. L. Nusinersen: A Treatment for Spinal Muscular Atrophy. *Annals of Pharmacotherapy* vol. 53 (2019).

81. Li, Q. Nusinersen as a therapeutic agent for spinal muscular atrophy. *Yonsei Medical Journal* vol. 61 (2020).

82. Qian, L. Therapeutic Effects of R-IDARAM and Intrathecal Immunochemotherapy on Elderly Patients with PCNSL. *ClinicalTrials.gov Identifier: NCT02836158* https://clinicaltrials.gov/ct2/show/NCT02836158?term=intrathecal&recrs=a&draw=1&rank=1 (2016).

83. Qian, L. Treatment of PCNSL WIth R-IDARAM and Intrathecal Immunochemotherapy. *ClinicalTrials.gov Identifier: NCT02657785* https://clinicaltrials.gov/ct2/show/NCT02657785?term=intrathecal&recrs=a&draw=1&rank=2 (2016).

84. Qian, J. Intrathecal Chemotherapy for Central Nervous System Metastasis in Retinoblastoma. *ClinicalTrials.gov Identifier: NCT04903678* https://clinicaltrials.gov/ct2/show/NCT04903678?term=intrathecal&recrs=a&draw=1&rank=5 (2021).

85. Kurtzberg, J. UCB Transplant of Inherited Metabolic Diseases With Administration of Intrathecal UCB Derived Oligodendrocyte-Like Cells (DUOC-01). . *ClinicalTrials.gov Identifier: NCT02254863* https://clinicaltrials.gov/ct2/show/NCT02254863?term=intrathecal&recrs=a&draw=2&rank=11 (2014).

86. Rong, L. Intrathecal Transplantation of UC-MSC in Patients With Late Stage of Chronic Spinal Cord Injury. *ClinicalTrials.gov Identifier: NCT03505034* (2018).

87. Staff, N. Intrathecal Autologous Adipose-derived Mesenchymal Stromal Cells for Amyotrophic Lateral Sclerosis (ALS). *ClinicalTrials.gov Identifier: NCT03268603* (2017).

88. Rong, L. Intrathecal Transplantation of UC-MSC in Patients With Sub-Acute Spinal Cord Injury. *ClinicalTrials.gov Identifier: NCT03521336* (2018).

89. Rong, L. Intrathecal Transplantation of UC-MSC in Patients With Early Stage of Chronic Spinal Cord Injury. *ClinicalTrials.gov Identifier: NCT03521323* (2018).

90. Prodromos, C. Safety of Cultured Allogeneic Adult Umbilical Cord Derived Mesenchymal Stem Cell Intrathecal Injection for ALS. *ClinicalTrials.gov Identifier: NCT05003921* (2021).

91. Lu, X. Autologous Bone Marrow-derived Mononuclear Cells for Acute Spinal Cord Injury. *ClinicalTrials.gov Identifier: NCT04528550* (2020).

92. Sehgal, A. First-in-Human Study of TSHA-101 Gene Therapy for Treatment of Infantile Onset GM2 Gangliosidosis. *ClinicalTrials.gov Identifier: NCT04798235* (2021).

Chapter 2: Quantification of Pharmacokinetic Solute Transport

** This is forthcoming in the Journal of Neuropharmacology under the title: In vitro pharmacokinetic quantification of human intrathecal solute transport: parametric investigation of injection parameters and infusion catheter versus lumbar puncture needle*

2.1 Introduction

According to the World Health Organization, disorders of the CNS including neuroinflammatory, neurodegenerative, and neurovascular conditions impact approximately one billion people in the world, making it the world's leading cause of disability. [1–3] Many of these neurological disorders require treatment. However, the human body's blood-brain barrier (BBB) tightly regulates transport of substances from the blood to the brain to precisely control CNS homeostasis, [4] often rendering oral and parenteral drug administration ineffective. [1,5] To overcome the BBB, two strategies have been proposed: 1) the development of drugs that can pass through the barrier; and 2) utilizing alternative drug delivery routes, such as intracerebroventricular, intranasal, intra-cisterna magna, and intrathecal drug delivery (ITDD). [1]

2.1.1 Intrathecal Drug Delivery

At present, ITDD is primarily utilized clinically for the treatment of three conditions: 1) chronic non-malignant pain; 2) muscle spasticity; and 3) cancer related pain. [6] Subcutaneous ports/electronic pumps or single dose injections through the interspinous ligaments in the L3-L5 region (similar to a typical lumbar puncture) are common administration methods for ITDD. [7] ITDD has been considered a viable option in solving the brain drug delivery problem as it allows for bypassing of the BBB to directly access the CNS. [8,9] It works by delivering the substance directly into the cerebrospinal fluid (CSF) within the spinal subarachnoid space (SAS). This route has been found to potentially reduce the required dose 100 to 300X compared to oral administration, which may lead to lower drug toxicity and reduced side effects while remaining effective. [1,3,10,11] Furthermore, ITDD can be considered less invasive compared to other drug delivery methods such as intracerebroventricular and intraparenchymal administrations. [7]

ITDD has been investigated in several additional applications. A study by Whiteside et al. investigated the efficacy of hyperbaric solutions as spinal anesthesia via the intrathecal route. [12] Previous studies have shown that lumbar intrathecal (IT) administration into the CSF reached the hypothalamus in baboons and dogs. [13,14] A study by Munoz-Rojas et al. found that a patient with Hunter syndrome who received intrathecal (IT) injections of loranidase showed improved walk test distance and pulmonary parameters, decreased numbing and tingling, increased stability, and a decreased need for pain medication. [15] Another study by Muenzer et al. showed that after 6 months, mean CSF glycosaminoglycans reduced in patients with Hunter syndrome after intrathecal treatment of idursulfase-IT. [16] Furthermore, the benefits of ITDD for cancer patients has been investigated. [17,18] The benefits associated with ITDD compared to conventional pain medication administration methods allowed patients to undergo more aggressive chemotherapy/radiation treatment and henceforth increased patient life expectancy. [17,19] The Food and Drug Administration recently approved morphine, ziconotide, and baclofen for use via the intrathecal route. [20] In 2016, nusinersen became the first approved drug to treat spinal muscular atrophy, a rare neuromuscular disorder, and is administered intrathecally as a 5 mL dose at the lumbar level. [21–23] Currently, there are several clinical trials that are investigating intrathecal chemotherapy, [24–26] stem cell therapy, [27–33] gene therapy, [34] and others. [35,36]

2.1.2 Modeling of CSF Transport

A thorough understanding of CSF flow dynamics may lead to improved detection and treatment of CNS disorders. [2,37] Solute transport in the CSF has been shown to play an important role in ensuring drug distribution to the target site. [38] CSF is a clear fluid that resides in the subarachnoid space (SAS) of the brain and spine. [39] It has several important purposes, including acting as a "shock absorber" to stabilize intracranial pressure, [39,40] providing protection and suspension of neural tissue, [37] and maintaining immunological and biochemical homeostasis. [41] The importance of CSF dynamics in CNS disorders has been investigated in several studies. [42–47] It is believed that CSF is produced primarily within the ventricles and absorbed at the arachnoid granulations on the surface of the superior sagittal sinus. [48] CSF pulsates in sync with intracranial cardiac and respiratory cycles and has approximately zero net flow. [2,39]

Several modeling studies have been conducted to assess intrathecal solute transport in the spinal CSF. In 1996, Myers and colleagues used an idealized 3D elliptical geometry to investigate the impact of injection flow rate, catheter size, and catheter angle. [49] An early study by Tangen et al. [50] used a patient specific SAS model to investigate the effects of spinal microanatomy on flow patterns and stirring effects. A later study by Tangen et al. [51] investigated the effect of injection volume and CSF pulsations. Hsu et al. [52] assessed the impacts of CSF pulsations on ITDD using a 2D geometric model from anatomical images. Pizzichelli et al. and Haga et al. investigated the effect of catheter position and angle, tissue permeability, and injection flow rates. [5,53] Kuttler and colleagues investigated the impact of a slow versus fast bolus. [54]

A precise understanding of the impact of injection parameters on pharmacokinetics may help optimize intrathecal solute transport and provide drug distribution to the target site of pharmacologic action. [51,54,55] Therefore, the goal of the present study was to investigate the impact of several lumbar puncture (LP)-based injection parameters and the injection device types on intrathecal solute transport to the brain in a subject-specific 3D anatomically realistic human in vitro model of the SAS. Here, we investigate the effect of bolus injection volume and rate, flush volume, rate, and timing, type of device, and location of injection.

2.2 Methods

The overarching approach was to utilize a subject specific 3D human model to investigate the impact of the following parameters on solute distribution to the brain via CSF using a simulated small molecule model of fluorescein: bolus injection volume and rate, flush volume, rate, and timing, injection location, type of device (Table 2-1). The brain was considered the target region for therapeutic benefit of the injected solute. Each experiment was conducted over the course of three hours and the solute distribution was observed via a spatial temporal slice average concentration and quantified in terms of the percent of the injected dose (%ID). A period of three hours was chosen to represent initial pharmacokinetic transport of the solute within the system, neglecting biology of solute uptake into the CNS tissue within this model.

Table 2-1. List of protocols to test the injection parameters. Red indicates the change in parameter between protocols. PA represents the posterior-anterior direction, IS represents the inferior to superior direction. LP represents lumbar puncture, indicating the needle was utilized.

Exp. Num.	Exp. Name	Inj. Loc.	Inj. Conc. (μM)	Inj. Dir.	Device	Bolus Vol. (mL)	Bolus Rate (mL/min)	Flush Vol. (mL)	Flush Rate (mL/min)
1	**1HUM1**	L3-L4	331.02	PA	LP	5	5	0	0
2	**1HUM2**	L3-L4	331.02	PA	LP	5	5	5	2.5
3	**1HUM3**	L3-L4	331.02	PA	LP	5	5	5	5
4	**2HUM1**	L3-L4	82.75	PA	LP	20	5	0	0
5	**2HUM2**	L3-L4	82.75	PA	LP	20	13.3	0	0
6	**3HUM1**	L3-L4	331.02	IS	Cath	5	5	0	0
7	**3HUM2**	L3-L4	82.75	IS	Cath	20	7	2	2.5
8	**3HUM3**	L3-L4	331.02	IS	Cath	5	5	12	5
9	**4HUM2**	L1-L2	331.02	IS	Cath	5	5	12	5
10	**5HUM1**	L3-L4	331.02	PA	LP	5	5	15	5
11	**5HUM4**	L3-L4	331.02	PA	LP	5	5	15 mL, 15 min	5

2.2.1 Model Geometry

The development of the subject-specific 3D model used in this study has been previously described by Sass et al. [56] and Khani et al. [2] In brief, a healthy 23-year-old female underwent a high-resolution T2 weighted magnetic resonance (MR) imaging sequence that was used to quantify subject-specific CSF flow data. [56] The model was developed by combining the result of the high-resolution MR images with 31 pairs of anatomically realistic dorsal and ventral nerve roots, thecal sac, and filum terminale. [2,56] Stereolithography was used to print the model as a 2 mm thick transparent shell in three parts: cranial, upper thoracic, and lower spine, to avoid exceeding the limit of the 3D printer. [2] Once combined, the model was 76 cm in length and had a total CSF space of approximately 330 mL.

2.2.2 Overall System Layout

The in vitro system layout has been previously used by our group has been briefly described by Khani et al. [2] In brief, the following system modifications were made in this study: a) the addition of a respiration component of CSF pulsations, b) the addition of two infusion pumps for implementation of the bolus injection and flush, c) CSF waveform verification, d) utilization of two cameras to image the system, e) implementation of an algorithm for image stitching from the two cameras. The current in vitro set up can be observed in Figure 2-1.

2.2.3 Flow Input Boundary Conditions and Verification

Cardiac-induced and respiratory CSF flow oscillations have been found to dominate long term solute spread. [54] Therefore, a respiration component of CSF pulsation was combined with the cardiac components of CSF pulsations under natural breathing for this study through a pulsatile waveform derived from Yildiz et al. [40] Custom built cardiac and respiratory oscillatory pumps utilizing the CSF waveform were combined at the caudal end of the model and a scaled down (1/36th) CSF waveform was imparted onto a custom ventricular oscillating pump to simulate the cardiac and respiratory components in the ventricles. [2,56,57] Both waveforms were in sync. Two off-the-shelf syringe pumps were used as the bolus and flush infusion pumps. An additional off-the-shelf pump continuously infused 0.4 mL/min representing CSF production in the lateral ventricles, a CSF production rate previously quantified in the literature (Figure 1). [58–60] To mimic solute transport in the CSF, an aqueous solution of fluorescein sodium was injected to represent a drug tracer. The usage of fluorescein as an injection tracer agrees with previous studies. [61–63] Given that solute transport within the CSF is dependent on pulsations and vorticity, thereby independent of the chemical composition of the bulk fluid, all experiments and solute injections were conducted using deionized water. [64]

To quantify CSF oscillatory waveform reliability, five repetitions using an inline flow sensor (Transonic, 4PXN) with a multi-channel research console (Transonic, T402) was conducted. Similarly, a smaller inline flow sensor (Transonic, 1PXN) was used to conduct five repetitions to verify CSF waveform imparted to the ventricles. All infusion and CSF production pumps were verified via a stopwatch and bucket test before and after all experiments were conducted.

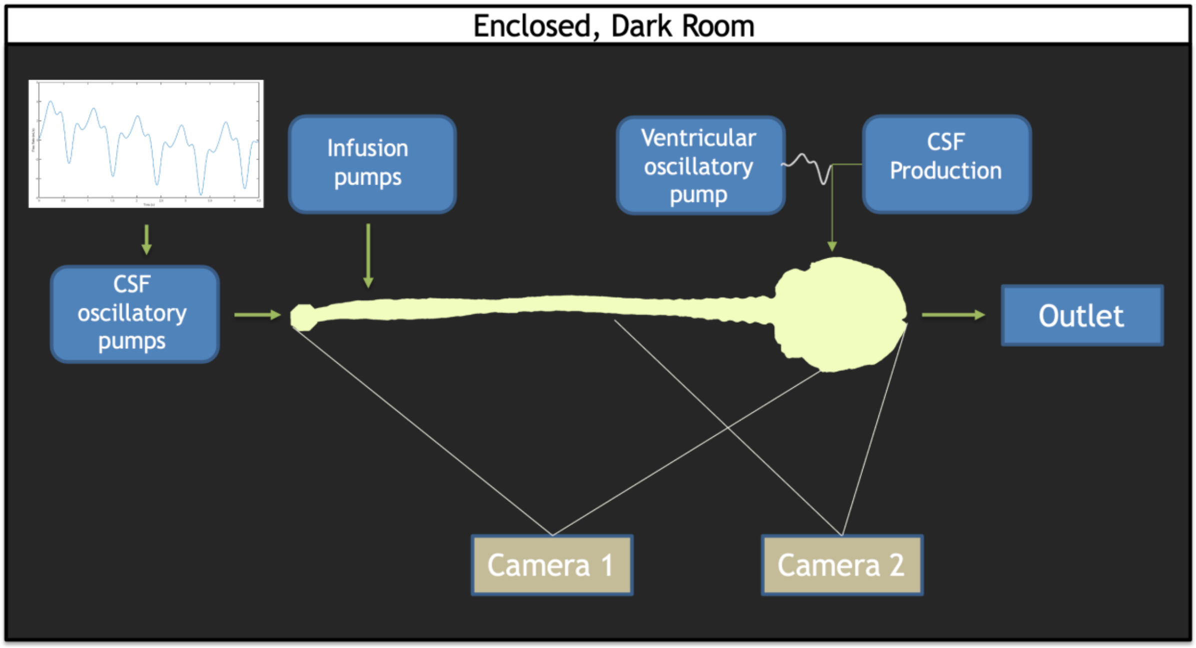

Figure 2-1. Overview of the in vitro model set up. The CSF waveform comprised of the cardiac and respiratory components is imposed by the CSF oscillatory pumps at the caudal end of the model. Infusion pumps consisting of both the bolus and flush pumps are located at the lumbar region. A ventricular oscillatory pump utilizes the identical CSF oscillations at the caudal end, but at 1/36th the scale. A CSF production pump set to infuse 0.4 mL/min into the ventricles. A CSF reservoir tank to capture the overflow rests at the cranial end of the model. Two cameras were used: one to capture the full span of the model (Camera 1) and one to capture the lower concentrations within the brain (Camera 2).

2.2.4 Imaging Configuration, Calibration and Post-processing

As previously described by Khani et al., [2,65] an imaging camera was used to quantify axial distribution of fluorescein tracer concentration over time. In brief, the system utilized two high-resolution cameras with one focused on the brain and the other focused on the spine (Figure 2-1). Each camera was optimized to attain maximum dynamic range within its respective imaging locations. The model was filled with a known concentration of fluorescein and imaged so that the raw pixel intensities could be converted to molar concentrations based on interpolation of pixel intensity values. Each calibration was repeated three times to improve the accuracy of the dynamic range for the experiments. To analyze both images from the brain and spine camera, the images were stitched (Figure 2-2). Stitched and non-stitched calibrations were compared to ensure the only region of difference occurred in the brain region.

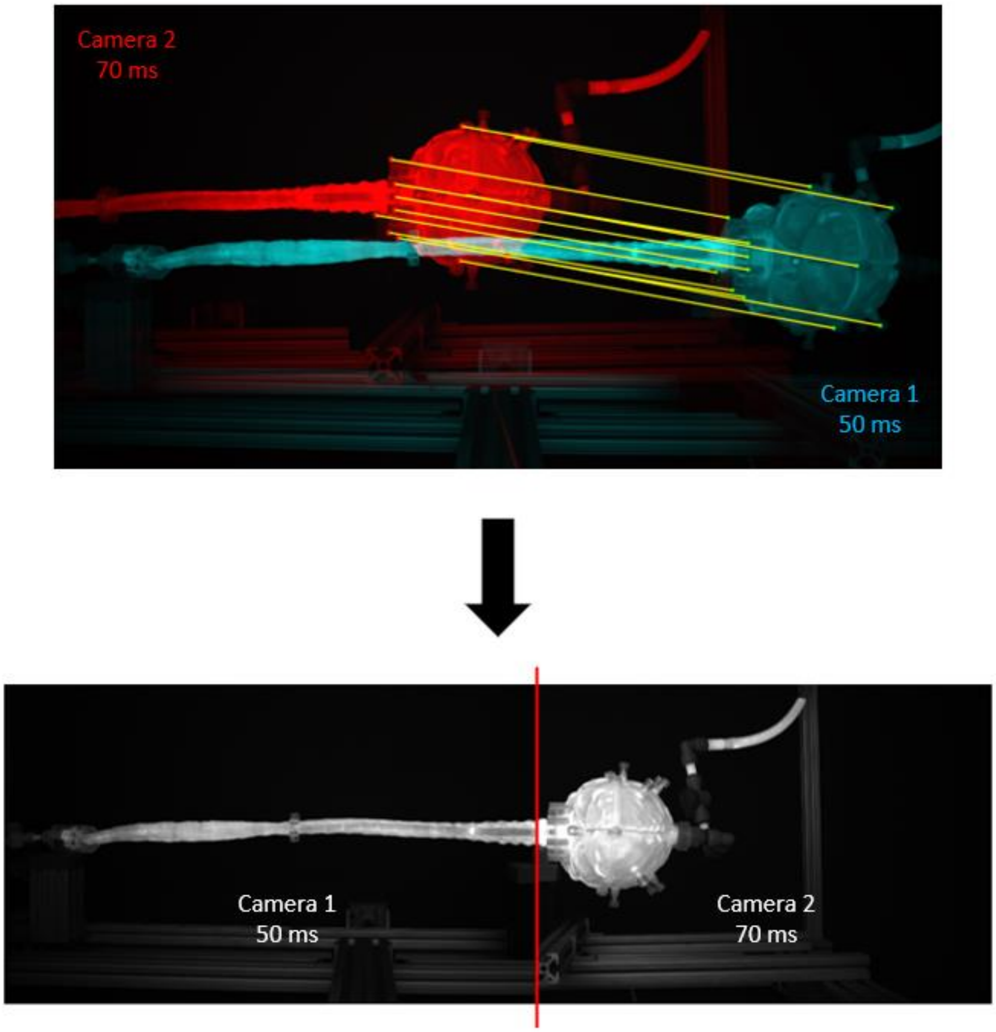

Figure 2-2. Results of the image stitching process. Twelve matching points from each camera are manually segmented and input to a MATLAB stitching algorithm to produce a stitched image at the C1 level. Camera 1 corresponds to the full model camera; camera 2 corresponds to the brain camera. There are twelve matching points, including: 1) brain cap center, 2) top port, 3) bottom port, 4) top of the cap, 5) bottom of the cap, 6) phalange middle, 7) phalange top, 8) flange bottom, 9) left mount corner, 10) very top of the flange, 11) very bottom of the phalange, 12) right mount corner.

2.2.5 Outline of the Injection Parameters

The outline of the tested parameters is shown in Table 2-2. These parameters included a) bolus injection rate and volume, b) flush volume, rate, and timing, c) infusion device either lumbar puncture needle or lumbar catheter, and d) infusion location within the lumbar spine. The baseline bolus volume and rate were set to 5 mL and 5 mL/min, respectively (1HUM1), values based on the protocol administered for nusinersen in spinal muscular atrophy. [21] This experiment was utilized as a standard for which to make comparisons across experiments.

To study the effect of bolus injection volume, the bolus injection rate was held constant at 5 mL/min and the bolus volume increased by four times from 5 mL to 20 mL (1HUM1 to 2HUM1). Injection bolus rate was observed by increasing the rate from 5 mL/min to 13.3 mL/min while maintaining a constant 20 mL bolus volume (2HUM1 to 2HUM2). To study the effect of flush volume, a 12 mL flush was added to the baseline case (3HUM1 to 3HUM3). Flush rate was observed by increasing the rate from 2.5 mL/min to 5 mL/min (1HUM2 to 1HUM3). The effect of device type was observed by switching the 3.5" 22-gauge spinal needle (approximately 0.4 mm ID, Jorgensen Labs, J-529 H, SNM1018-046) in the baseline case to a 3.5 Fr (0.6 mm ID x 1.1 mm OD) rounded tip polyurethane catheter (Access Technologies, CNC-3.5PR-36") (1HUM1 to 3HUM1). Injection location was compared by moving the catheter tip from L3-L4 to L1-L2 (3HUM3 to 4HUM2). The impact of a delayed flush was also compared by injecting a 15 mL flush immediately after the bolus injection and 15 minutes after the bolus injection (5HUM1 to 5HUM4).

Table 2-2. Experimental design of tested ITDD injection parameters. The parameter, its associated protocols, and the range analyzed are included.

Num.	Parameter	Protocol 1	Protocol 2	Range Analyzed
1	Bolus Volume	1HUM1	2HUM1	5 – 20 mL
2	Bolus Rate	2HUM1	2HUM2	5 – 13.3 mL/min
3	Flush Volume	3HUM1	3HUM3	0 – 12 mL
4	Flush Rate	1HUM2	1HUM3	2.5 – 5 mL/min
5	Device	1HUM1	3HUM1	Needle - Cath
6	Injection Location	3HUM3	4HUM2	L3/L4 – L1/L2
7	Flush Timing	5HUM1	5HUM4	0 – 15 min

2.2.6 Repeatability and Reliability

To verify repeatability of experimental results three repetitions for each experiment were conducted with an average time delay of six days between each experiment. A detailed comparison of repetitions was performed by the following correlation analysis: the standard deviation for all three repetitions at each z-location and time was calculated and plotted as a spatial temporal plot to visualize the location of variability between repetitions. Additionally, an array of the mean at each z-location and time for all three repetitions was generated and each individual repetition of an experiment was subtracted from this mean and plotted as a Bland-Altman plot in terms of spatial temporal differences of concentration and location over three hours post injection. The standard deviation and the 95% confidence interval (95% CI) of the mean of the repetitions was calculated. Furthermore, the percent of the dynamic range (%DR) was calculated as:

$$\% DR = \frac{95\%\ CI}{C_{max}} * 100 \qquad \text{(Eqn. 1)}$$

where C_{max} represents the maximum concentration. Ideally, the %DR is less than 5%. The root mean square error (RMSE) was quantified based on the measured CSF oscillatory waveforms.

2.2.7 Quantification of Intrathecal Solute Transport

To quantify the intrathecal solute transport to the brain at three hours post injection, the percent of the injected dose (%ID) was used and was calculated as:

$$Injection\ Mass\ (g) = Injection\ Volume\ (mL) * Injection\ Concentration\ (\frac{g}{mL}) \qquad \text{(Eqn. 2)}$$

$$Slice\ Mass\ (g) = Slice\ Volume\ (mL) * Slice\ Concentration\ (\frac{g}{mL}) \qquad \text{(Eqn. 3)}$$

$$Slice\ Sum\ (g) = \Sigma\ Slice\ Mass\ (g) \qquad \text{(Eqn. 4)}$$

$$\%ID\ to\ brain\ = \left(\frac{Slice\ Sum}{Total\ Injected\ Mass}\right) * 100 \qquad \text{(Eqn. 5)}$$

The brain portion of the model was defined as everything superior to the craniocervical junction located at model position 0 cm. Solute exposure to the brain was calculated as the trapezoidal integral value of the tracer concentration over three hours and is hereon referred to as the area under the curve (AUC).

2.2.8 Statistical Analysis

The mean, standard deviation, and 95% confidence interval in terms of %ID was calculated for each experiment. To assess the significance of a given parameter, the pooled variance was calculated using the following analysis. First, a variance check was conducted in STATGRAPHICS and the variances were found to be equal. The common standard deviation was then estimated by the pooled standard deviation. The populations were assumed to be independent and normal, such to allow the assumption that the population followed a t-distribution with $n_1 + n_2 - 2$ degrees of freedom. The (1-α)100% confidence interval for $\mu_1 - \mu_2$ for pooled variances could be calculated as: $\overline{x_1} - \overline{x_2} \pm t_{\frac{\alpha}{2}} s_p \sqrt{\frac{1}{n_1} + \frac{1}{n_2}}$, where x_1 is the mean from sample 1, x_2 is the mean from sample 2, $t_{\frac{\alpha}{2}}$ comes from a t-distribution with $n_1 + n_2 - 2$ degrees of freedom, s_p is the pooled standard deviation, and n_1 and n_2 correspond to the sample sizes of population 1 and 2, respectively. A one-way analysis of variance in MATLAB was conducted to test significant differences between parameters. An α = 0.05 was used to indicate significance.

2.3 Results

2.3.1 Verification of Boundary Conditions and Repeatability

The CSF oscillatory waveforms were verified using the Transonic flow meter with a RMSE of 56% and 15% for the CSF waveform at the caudal end of the model and the ventricles, respectively. Overall, good agreement was seen between the input of the in vitro model and the ideal waveform (Figure 2-3). Variations in peaks can be accounted for by the direction of the oscillatory pumps used in the in vitro set up/model. A stopwatch and bucket test was used to calculate the error as percent of average CSF production rate and was found to be 0.02%. Strong repeatability was seen between experiment repetitions (Table 2-3). The greatest standard deviation and 95% confidence interval observed was 1.68 and 3.29 micromoles, respectively, and error as a %DR did not exceed 6.87% for all experiments conducted (Table 2-3). Agreement of solute distribution with respect to time and location across repetitions can be observed as a spatial temporal plot in Figure 2-4A. The location with greatest variance for repeated experiments was near the injection location (Figure 2-4B).

2.3.2 Effect of Injection Parameters

Impact of injection parameters on solute transport to the brain are shown in Table 2-4. From the conducted protocols, flush volume was the most important factor leading to increased solute delivery to the brain, followed by flush rate, bolus injection volume, location, device, and bolus injection rate (Figure 2-5). By increasing the flush volume from 0 to 12 mL (3HUM1 to 3HUM3), solute transport increased in the brain by 3.9% (95% CI 1.6%ID to 6.1%ID, p = 0.009, *Supplementary Figure 1*). Additional flush volume protocols were conducted, and similar trends were observed. An increase of flush rate from 2.5 to 5 mL/min (1HUM2 to 1HUM3) increased 1.6 %ID (95% CI 0.2 %ID to 2.9 %ID, p = 0.038, *Supplementary Figure 2*). Using a catheter increased solute transport to the brain by 1.5 % ID (95% CI 0.3 % ID to 2.7 % ID, p = 0.026, *Supplementary Figure 3*). By increasing the bolus injection volume from 5 to 20 mL (2HUM1 to 2HUM2) increased solute transport to the brain by 1.3% (95% CI -0.7 %ID to 3.2 %ID, *Supplementary Figure 4*). Moving the catheter tip from L3-L4 to L1-L2 (3HUM3 to 4HUM2) increased by 1.2% (95% CI -1.9 %ID to 4.4 %ID, *Supplementary Figure 5*). An additional location experiment was conducted, and similar trends were observed. An increase in bolus injection rate had the least impact on solute delivery to the brain; an increase from 5 to 13.3 mL/min (2HUM1 to 2HUM2) showed a decrease in %ID to the brain by 0.6% (95% CI -2.3 %ID to 1.2 %ID, *Supplementary Figure 6).* Similar results were observed when comparing the average AUC in the brain at three hours (Table 2-4). An increase of 1.2 %ID (95% CI -3.2 %ID to 5.6 %ID, *Supplementary Figure 7*) was seen with a delayed flush. The bolus injection volume, type of device, location of injection, and bolus injection rate were not statistically significant. In addition, % ID observed in the protocols relating to a lumbar catheter (3HUM1 without flush – 4HUM2 with flush) ranged from 6.0 – 11.6%, while the % ID observed in the protocols relating to a lumbar needle (1HUM1 with lower bolus injection volume and rate – 2HUM2 with higher bolus injection volume and rate) ranged from 4.9 – 6.5% (*Supplementary Figure 8*). These differences were statistically significant ($p < 0.05$).

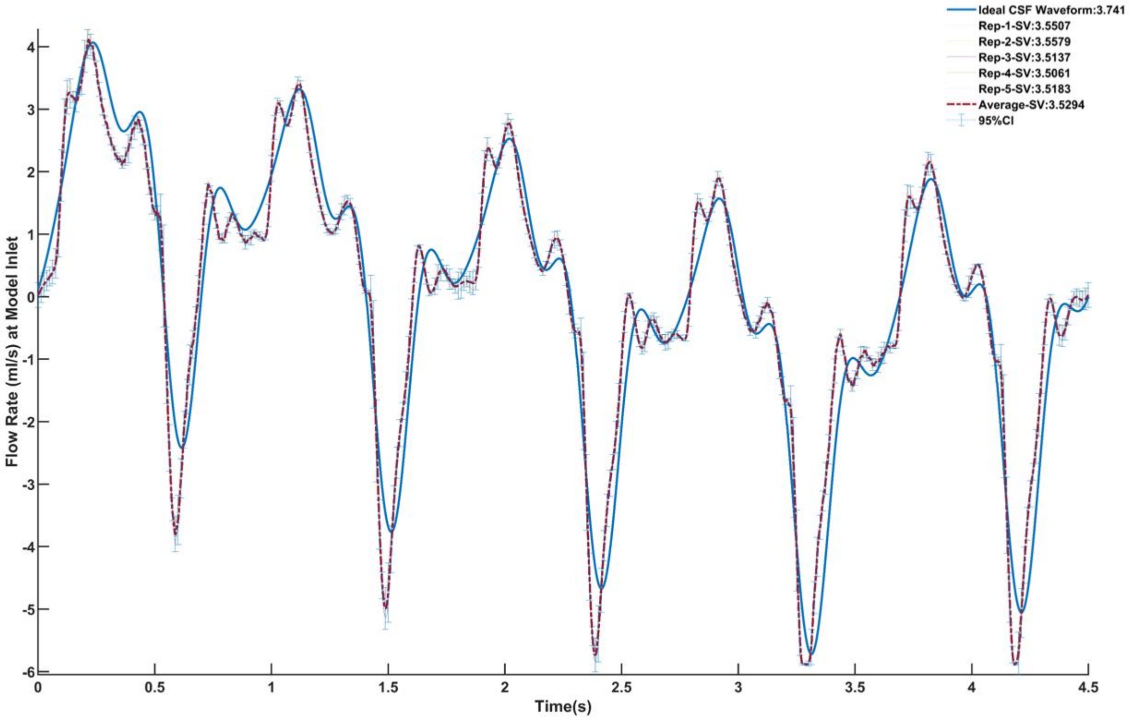

Figure 2-3. Verification of the CSF oscillatory waveform at the caudal end of the model using five repetitions. The ideal waveform derived from MRI measurements is outlined in blue. Each repetition is shown and the relative stroke volume is calculated. The average of all five repetitions is outlined in the red dashed line. The 95% confidence interval for the average of the repetitions is also shown.

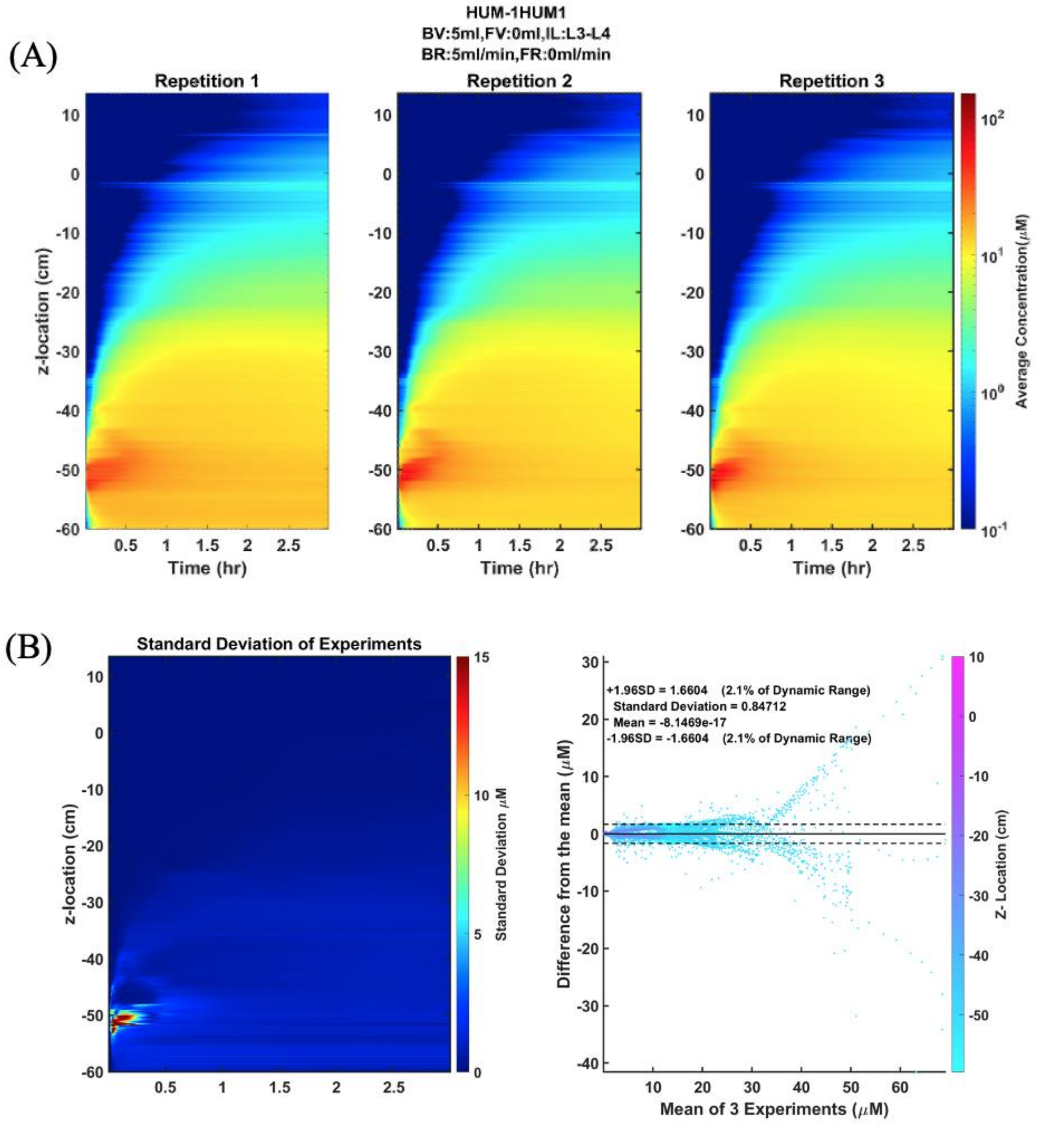

Figure 2-4. Repeatability and reliability across repetitions of an experiment. A) The spatial temporal plot representing the average concentration of each slice by position and time for each repetition is shown to visualize the distribution of the solute over time. B) The standard deviation spatial temporal plot indicating the regions of greatest variance across the three repetitions, in addition to a Bland-Altman plot showing the difference of each repetition from the mean of the repetitions.

2.3.3 AUC Trends and Impact of Time Duration Analyzed

Across all experiments, a ~2 log difference in solute concentration was present between the concentration of solute within the spine compared to the brain over the three-hour period (Figure 2-6). AUC values near the injection site were greatest for all experiments and AUC values around the brain dropped precipitously with a minimum amount located near the superior aspect of the brain. Protocols with the greatest solute transport to the brain displayed the lower AUC values in the lumbar region at one and three hours post injection (Figure 2-6). For all cases, the solute distribution differences decreased over time (Figure 2-7). In 1HUM1 at 10 minutes, the solute spread to approximately the thoracic region (T8/T9); in 4HUM2 at 10 minutes, the solute started to spread to the cervical region (C7). However, at three hours post injection, the distribution of the solute appeared similar with both cases spreading around the brain to some degree.

Table 2-3. Repeatability and reliability between the repetitions for each in vitro experiment. The standard deviation and 95% confidence interval are calculated in terms of micromoles and % ID.

Exp. Num.	Exp. Name	By (µM)		By %ID	
		|SD| (µM)	95% CI (µM) (Error as %DR)	|SD| (%ID)	95% CI (%ID)
1	**1HUM1**	0.7965	1.561 (2.03%)	0.65	1.28
2	**1HUM2**	1.1319	2.218 (1.82%)	0.69	1.36
3	**1HUM3**	0.6484	1.271 (1.01%)	0.55	1.08
4	**2HUM1**	1.6804	3.294 (3.15%)	1.00	1.96
5	**2HUM2**	1.6301	3.195 (2.23%)	0.41	0.80
6	**3HUM1**	1.2837	2.516 (5.2%)	0.40	0.78
7	**3HUM2**	0.6595	1.293 (2.4%)	1.26	2.47
8	**3HUM3**	0.7450	1.460 (3.01%)	1.35	2.64
9	**4HUM2**	0.9928	1.946 (1.24%)	1.42	2.79
10	**5HUM1**	1.476	2.893 (6.87%)	1.18	2.32
11	**5HUM4**	1.3723	2.689 (4.26%)	2.46	4.83

2.4 Discussion

Intrathecal drug delivery to the brain has been increasingly utilized and investigated in part due to its potential for comparably low required dosages to achieve the desired pharmacological response. [6] This may potentially translate into increased efficacy and reduced side effects relative to oral and parenteral administration of the same agent. [6,51] Despite this trend, there still exists a dearth of knowledge regarding the effect of injection parameters on solute transport. Therefore, guidelines to assist clinicians in the selection of specific administration parameters may further improve treatment outcomes for patients. [51] Our approach was to model early drug pharmacokinetic distribution within the CSF system, neglecting drug absorption into the tissue of the CNS, using a subject specific patient model to parametrically assess the effects of 1) bolus injection volume and rate; 2) flush volume, rate, and timing; 3) lumbar spine injection location; 4) type of device. The key findings of this study include:

1. Under all injection scenarios analyzed, relatively little solute reached the brain (less than 12%ID).
2. Flush volume increased solute distribution to the brain to a greater degree than other parameters analyzed.
3. Increasing bolus injection rate did not increase % ID solute to the brain.
4. Use of a lumbar placed catheter for injection of the solute resulted in greater solute distribution to the brain compared to lumbar puncture needle.

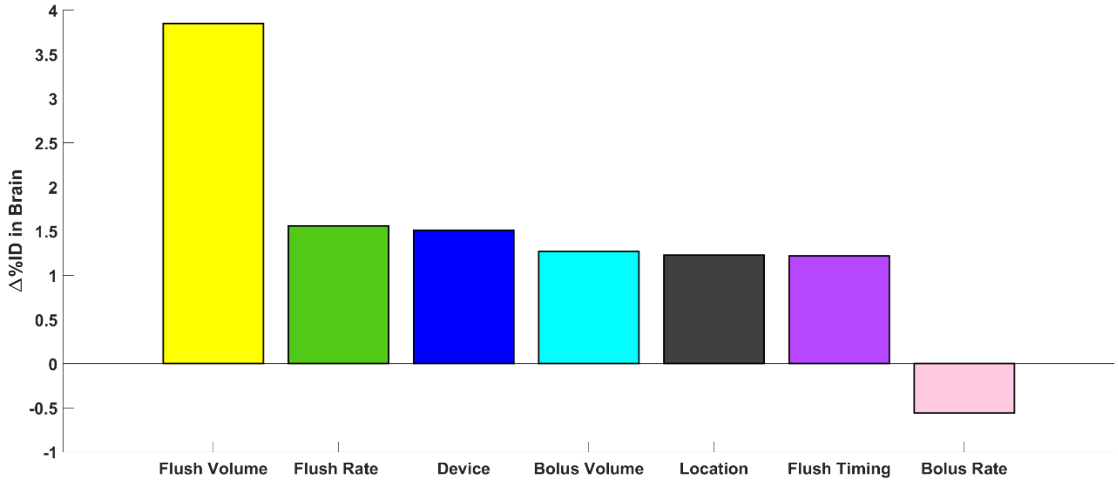

Figure 2-5. Parametric comparison of parameters. Represented as the change in % ID in the brain at three hours, the impact of all parameters tested can be visualized.

2.4.1 Relatively little solute reached the brain

Across all experiments conducted in this study, the goal was to maximize the amount of solute transport to the brain. Regardless of protocol, all LP simulations resulted in limited distribution to the brain. Indeed, the range of % ID observed in the brain at three hours post injection was 5.0 – 11.6% in the protocols tested. This indicates that most of the injected solute remains in the spinal region. In the case of spinal cord injury or disease, this may be a desirable result as the target is within the spinal region. In cases of targeting the brain, the efficiency of solute transport observed in this study was, at best, ~10 %ID and dosing decisions would need to account for this limited distribution. Parametric changes in %ID induced by flush volume, rate, and timing, bolus volume and rate, location of lumbar injection, and type of lumbar device did modify solute transport to the brain bya range of -0.6 – 3.9 %ID. While these changes are small, the degree of change in terms of percent from standard LP injection protocol could be considerable. Indeed, if 5% of the total solute is delivered to the brain, a parametric change in %ID of 3.9% equates to a 78% increase in solute transport to the brain. In this context, one can see how readily optimization of solute transport to the brain can be attained. This demonstrates an opportunity in which a small change in injection parameter can make substantial percentwise improvements in brain delivery.

Table 2-4. Quantification of parametric comparison by ranking. Relevant information includes the parameter investigated, range of the given parameter, the names of the protocols used to investigate the parameter, and the % ID and average AUC in the brain at three hours for each protocol. The change in % ID and average AUC are calculated and used to compare the impact of the given parameter.

Rank	Parameter	Range of parameter analyzed	Protocol names	%ID to brain @ 3hrs (Δ%ID)	Avg brain AUC (μM-hr) @ 3hrs (ΔAUC)	Statistical Significance, α = 0.05
1	Flush Volume	0 vs 12 mL	3HUM1 vs 3HUM3	6.53 vs 10.38 (+3.85)	0.67 vs 1.20 (+0.53)	p=0.009 *
2	Flush Rate	2.5 vs 5 mL/min	1HUM2 vs 1HUM3	4.90 vs 6.46 (+1.56)	0.50 vs 0.64 (+0.14)	p=0.038 *
3	Device	Needle vs Cath	1HUM1 vs 3HUM1	5.02 vs 6.53 (+1.51)	0.48 vs 0.67 (+0.19)	p=0.026 *
4	Bolus Volume	5 vs 20 mL	1HUM1 vs 2HUM1	5.02 vs 6.29 (+1.27)	0.48 vs 0.66 (+0.18)	p=0.14
5	Location	L3/L4 vs L1/L2	3HUM3 vs 4HUM2	11.61 vs 10.38 (+1.23)	1.20 vs 1.37 (+0.17)	p=0.39
6	Flush Timing	0 vs 15 min	5HUM1 vs 5HUM4	6.00 vs 7.22 (+1.22)	0.69 vs 0.86 (+0.17)	p=0.48
7	Bolus Rate	5 vs 13.3 mL/min	2HUM1 vs 2HUM2	6.29 vs 5.73 (-0.56)	0.66 vs 0.65 (-0.01)	p=0.42

2.4.2 Flush volume was the single most important factor for solute transport

Flushing the injection device may help rinse out residual drug volume and ensure device integrity and is therefore often part of ITDD protocols. [66–68] Our results showed that an increase in flush volume consistently and significantly (p = 0.009) increased the solute distribution to the brain

(Figure 2-5). This is most likely caused by volumetric displacement of fluid along the neuroaxis and agrees with pre-clinical study findings. [69] Tangen et al. utilized a computational model to investigate two protocols related to flush. [51] Their first protocol with a 5 mL bolus injection and a 5 mL flush showed high drug concentration spread between the C3 and T5 region; their second protocol with a 5 mL bolus injection and a 10 mL flush at the same injection rate showed spread to the upper cervical spine and the brain parenchyma, ensuring drug delivery to the brain within one hour post injection. [51] Similar protocols were conducted for our in vitro study relating to flush volume. For both protocols conducted in our study with the 5 mL flush, the solute spread reached the C1-C4 levels at one hour post injection, and for a higher flush volume of 15 mL, the solute reached the brain within one hour post injection, which is in good agreement with the Tangen study. The effect of flush volume has also been investigated in vivo. A study by Wolf et al. utilized a variety of imaging methods to track neuraxial exposure following an IT lumbar bolus injection in rats. [70] A protocol consisting of a 30 µL bolus followed by a 40 µL saline flush was tested. Immediately following injection, the bolus filled the entire SAS of the spine and reached the cranial CSF spaces within two hours, which lead to a greater distribution of solute to the brain than the protocol without flush.

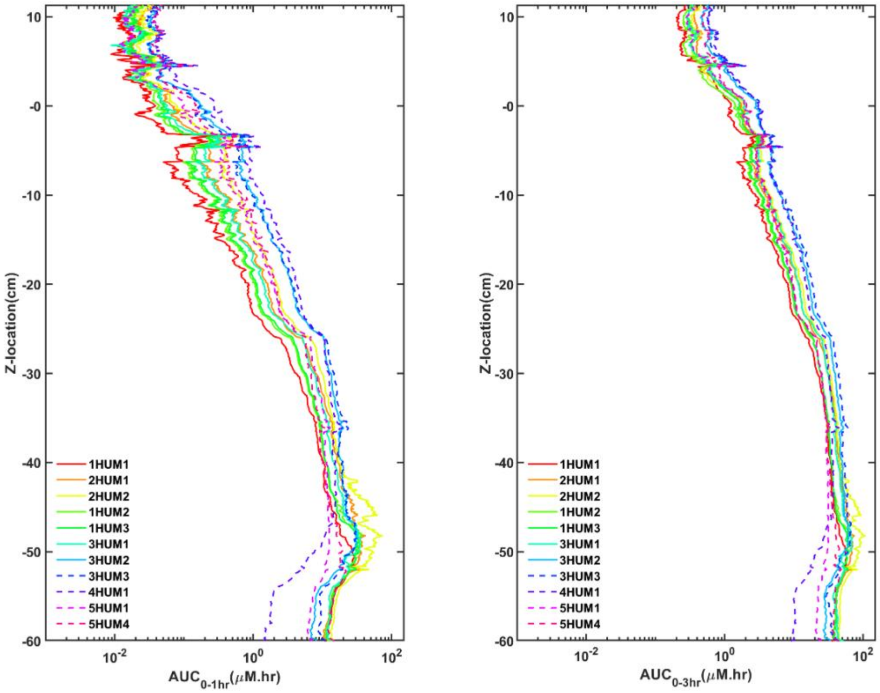

Figure 2-6. AUC trends for all cases at A) one-hour and three hours for all cases and B) one and three-hours for the best/worst case. There is good agreement of the trends and a significant difference between the best and worst case.

A continued investigation into the impact of flush volume is important for improved gene therapies and enzyme replacements targeting the brain parenchyma. [51,70,71] Therefore, a series of additional administration protocols were conducted to investigate the effect of a second flush in this study (data not shown). In brief, 15 minutes after an initial bolus injection and flush infusion, a second 10 mL flush was added. A substantial increase by 2.4 %ID in solute transport to the brain was observed for the second flush, which was expected and further supported the potential impact of flush volume. Independent of the flush administration timing (0, 15, or 30 minutes after bolus injection), a benefit of the flush was observed. While multiple flushes and flush timing has not been either non-clinically or clinically investigated to our knowledge, repeated bolus injections have been shown to have a therapeutic effect in context of intrathecal pain and spasticity therapeutics: improved functional scores, lower 24-hour opioid dose, and less dose escalation. [72] Additionally, multiple bolus doses showed reduced potential for intrathecal fibrosis in dogs when compared to continuous infusion, though this may be accounted for by a drug specific effect and may not hold true for all drugs. [73] Repeated bolus injections, and therefore perhaps flushes, may also allow lower injection volumes and more rapid CSF pressure recovery post-injection.

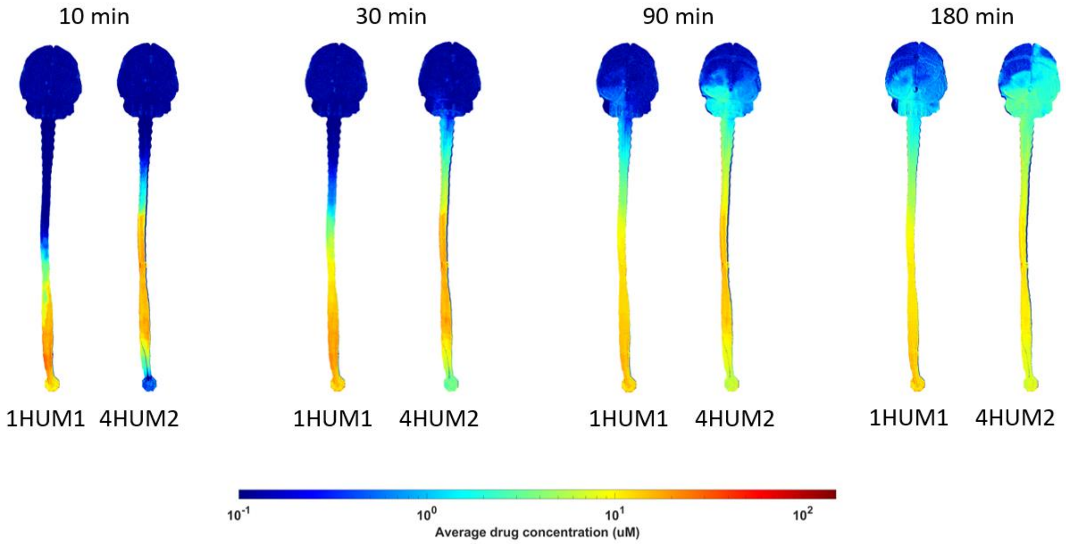

Figure 2-7. Difference in distribution over time. Solute transport for 1HUM1 (left) and 4HUM2 (right) are shown at 10 minutes, 30 minutes, 1.5 hours, and 3 hours. There is a significant difference between the protocols at the 10 minutes and 30 minutes time points, however, at 1.5 and 3 hours, this difference decreases.

2.4.3 Increasing bolus rate by ~2X had little impact on solute transport

Increasing bolus injection rate did not increase solute transport to the brain (Figure 2-5, Table 2-4). It is commonly reported among clinicians that the rate of bolus injection can increase solute spread, particularly within the spinal anesthesia literature. The phenomenon has been conjectured to be a result of increased turbulence at the tip of the needle that could, in principle, increase diffusion and mixing of the injected solute. [74,75] Similarly, within intrathecal drug delivery, investigators have considered that increasing an acute bolus injection rate may increase solute transport to the brain. In the present study, we increased the bolus injection rate from 5 to 13.3 mL/min and did not observe any statistically significant differences between the rates. The difference in findings may be a result of differing flow regimes. Typically, intrathecal drug delivery has been used to treat chronic pain and, in those cases, pain medication is often administered chronically in slow doses over the course of several hours or even days on the order of 0.01 to 0.02 mL/min. [74,76] This is a value 200-300X slower than that imposed in our acute dosing study that ranged from 5 to 13 mL/min, and thus may not be directly comparable for the scenarios analyzed.

2.4.4 Use of a lumbar placed catheter resulted in greater solute distribution to the brain compared to LP needle

On average, the results for the lumbar puncture catheter experiments delivered approximately twice as much solute to the brain compared to the results of the lumbar puncture needle experiments (*Supplementary Figure 8*). We hypothesize that this is primarily a result of the catheter and needle orientations. An alternative explanation may be the differences in the inner diameters between the types of devices, which were 0.4 mm and 0.6 mm for the LP needle and catheter, respectively. To test these hypotheses, an additional experiment was conducted testing the effect of catheter orientation. In a typical lumbar puncture, the needle is oriented posterior to anterior; catheters are typically oriented inferior to superior. In one additional experiment, the LP catheter was oriented anterior to posterior and compared to an equivalent LP needle protocol to test whether the device geometry may play a role. While there was a slight increase of 0.23 %ID with the LP catheter compared to the LP needle, no significant differences were observed. When the catheter was oriented inferior to superior with the equivalent protocol, a statistically significant ($p = 0.026$) increase of 1.3 %ID to the brain was quantified. Furthermore, the results agree with a study conducted by Pizzichelli et al. [5] They tested the effect of catheter angle and position in a subject specific model and found that higher drug penetration to the spinal cord was achieved when the catheter was oriented perpendicularly. When the catheter is oriented inferior to superior, the jet velocities are also oriented in that direction, perhaps pushing the drug in the direction of the brain during the period of injection. Therefore, we hypothesize that the observation that the LP catheter resulting in greater solute transport to the brain than compared to LP needle may be explained primarily by the LP catheter and needle orientations, though it should be noted that the geometry of the devices are different, which in principle would result in slightly different velocities and did show to have a minor effect for the conditions analyzed.

All individual parameters showed an impact on solute transport to the brain; however, this effect was relatively little (the greatest increase was 3.9% of the injected dose). The case that showed the greatest solute transport to the brain in this study was 4HUM2, which utilized a combination of injection parameters including: a) a higher injection location, b) a lumbar puncture catheter, and c) an increased flush volume. This is indicative that rather than a single parameter, a combination of the injection parameters may have the greatest impact on increasing solute transport to the brain and thereby needs to be investigated further.

2.4.5 Early pharmacokinetic solute transport in the CSF agrees with in vivo human studies

Research has indicated that patient specific CSF flow can be a factor leading to changes in CSF solute transport within humans. [77–80] Thus, because the current study was formulated based on subject-specific CSF flow boundary conditions, we expect results to be representative in vivo flow phenomena, but not identical. A study by Verma et al. quantified CSF-brain molecular exchange, neuraxial spread, and CSF-peripheral clearance in 15 healthy human volunteers after intrathecal injection of artificial CSF and Technetium-99 DPTA and observed signal translocation within the cranial cisterns and the brain parenchyma by three hours post injection. [8] Another study measured glymphatic flow in a single 55-year-old male and found traces of gadobutrol delivered intrathecally in the cisterna magna between 1-3 hours post injection. [81] A study by Ringstad et al. observed contrast of gadobutrol in the foramen magna after 20 minutes and a later study by the group observed contrast in the cerebellum between 2-4 hours post IT administration in eight healthy volunteers. [82,83] In the present study, we observed solute transport within the cranial region between 1-3 hours post injection, indicating gross agreement with these in vivo studies.

2.4.6 Limitations

There are several in vitro modeling limitations that have been previously described by our group. [56] A primary limitation of the study was that the subject specific 3D model used in this study neglects to assess drug absorption into the tissues of the CNS. Our approach was therefore to quantify early solute transport within a short time scale after injection. Depending on the solute absorption the results can vary substantially and could be modeled in future work by integrating molecular action of the solute and the CNS. All experiments were conducted at room temperature in a rigid model, which would result in slightly different molecular diffusion and viscosity compared to human body temperature. Furthermore, drug specific kinetics have been shown to play an important role in the rate of drug dispersion and tissue uptake. [51] This study consisted of a generalized model of solute transport using an aqueous solution of fluorescein to represent a small molecule drug. Additionally, studies have shown that the pulsation rate has a significant effect on solute transport. [51,52] A singular, consistent, and idealized waveform was used in this study for which to make parametric comparisons across injection scenarios. Future work should validate the results of this study with differing CSF pulsations and differing subject specific models. Furthermore, in vivo studies have tracked drug dispersion up to 80 hours [81] and in vitro studies up to 24 hours. [65] Longer duration in vitro studies could be conducted to further confirm the agreement between the trends observed in vitro and in vivo. Even with these limitations, the overall solute transport dynamics within a short timeframe post injection had many similarities with in vivo, as discussed.

2.4.7 Conclusions and Future Work

We addressed ITDD injection parameters within a complete CSF system of a 3D subject specific human model. These parameters included: bolus injection volume and rate, flush volume and rate, injection location, type of device, and flush timing. For all simulations analyzed, the overall efficiency of solute delivery to the brain was limited with <10% of ID reaching the intracranial space. Because delivery efficiency to the brain was low, even small improvements in %ID to the brain due to injection protocols were found to potentially have substantial impact. Within that context, flush volume had the most significant impact on increasing solute transport to the brain within three hours (+3.9 %ID, p=0.009). This was followed by flush rate (+1.6 %ID, p=0.038), type of device (+1.5 %ID, p=0.026). Bolus injection volume (+1.3 %ID), injection location (+1.2 %ID), flush timing (+1.2 %ID), and bolus injection rate (-0.6 %ID) did not show a statistically significant impact. In combination, these findings indicate that LP-based ITDD injection protocols can be optimized by modest changes in injection parameters and devices to improve therapeutic delivery of drugs to the brain.

2.5 References

1. Calias, P., Banks, W. A., Begley, D., Scarpa, M. & Dickson, P. Intrathecal delivery of protein therapeutics to the brain: A critical reassessment. *Pharmacology and Therapeutics* vol. 144 (2014).

2. Khani, M. *et al.* In vitro and numerical simulation of blood removal from cerebrospinal fluid: Comparison of lumbar drain to Neurapheresis therapy. *Fluids and Barriers of the CNS* **17**, (2020).

3. Soderquist, R. G. & Mahoney, M. J. Central nervous system delivery of large molecules: Challenges and new frontiers for intrathecally administered therapeutics. *Expert Opinion on Drug Delivery* vol. 7 (2010).

4. Daneman, R. & Prat, A. The blood–brain barrier. *Cold Spring Harbor Perspectives in Biology* **7**, (2015).

5. Pizzichelli, G. *et al.* Numerical study of intrathecal drug delivery to a permeable spinal cord: effect of catheter position and angle. *Computer Methods in Biomechanics and Biomedical Engineering* **20**, (2017).

6. Shah, N. & Padalia, D. *Intrathecal Delivery System*. *StatPearls* (2019).

7. Belov, V. *et al.* Large-Volume Intrathecal Administrations: Impact on CSF Pressure and Safety Implications. *Frontiers in Neuroscience* **15**, (2021).

8. Verma, A. *et al.* Intrathecal 99mTc-DTPA imaging of molecular passage from lumbar cerebrospinal fluid to brain and periphery in humans. *Alzheimer's and Dementia: Diagnosis, Assessment and Disease Monitoring* **12**, (2020).

9. Brumback, R. A. Book Reviews: The Physiology and Pathophysiology of the Cerebrospinal Fluid, by H. Davson, K. Welch, and M.B. Segal. Published in 1987 by Churchill Livingstone Inc, New York, 1013 pages, $198.00. *Journal of Child Neurology* **3**, (1988).

10. Gulur, P., Bhatia, G., Lau, M. E. & Koury, K. M. Intrathecal Drug Delivery (ITDD) systems for cancer pain. *F1000Research* **2**, (2014).

11. Simpson, K. H. & Jones, I. Intrathecal drug delivery for management of cancer and noncancer pain. *Journal of Opioid Management* vol. 4 (2008).

12. Whiteside, J. B., Burke, D. & Wildsmith, J. A. W. Spinal anaesthesia with ropivacaine 5 mg ml-1 in glucose 10 mg ml-1 or 50 mg ml-1. *British Journal of Anaesthesia* **86**, (2001).

13. LeBel, C., Bourdeau, A., Lau, D. & Hunt, P. Biologic response to peripheral and central administration of recombinant human leptin in dogs. *Obesity Research* **7**, (1999).

14. McCarthy, T. J. *et al.* Positron emission tomography shows that intrathecal leptin reaches the hypothalamus in baboons. *Journal of Pharmacology and Experimental Therapeutics* **301**, (2002).

15. Munoz-Rojas, M. V. *et al.* Intrathecal enzyme replacement therapy in a patient with mucopolysaccharidosis type I and symptomatic spinal cord compression. *American Journal of Medical Genetics, Part A* **146**, (2008).

16. Muenzer, J. *et al.* A phase I/II study of intrathecal idursulfase-IT in children with severe mucopolysaccharidosis II. *Genetics in Medicine* **18**, (2016).

17. Smith, T. J. *et al.* Randomized clinical trial of an implantable drug delivery system compared with comprehensive medical management for refractory cancer pain: Impact on pain, drug-related toxicity, and survival. *Journal of Clinical Oncology* **20**, (2002).

18. Rauck, R. L. *et al.* Long-Term Intrathecal Opioid Therapy With a Patient-Activated, Implanted Delivery System for the Treatment of Refractory Cancer Pain. *Journal of Pain* **4**, (2003).

19. Deer, T. R. *et al.* Comprehensive consensus based guidelines on intrathecal drug delivery systems in the treatment of pain caused by cancer pain. *Pain Physician* vol. 14 (2011).

20. Bottros, M. M. & Christo, P. J. Current perspectives on intrathecal drug delivery. *Journal of Pain Research* vol. 7 (2014).

21. Neil, E. E. & Bisaccia, E. K. Nusinersen: A novel antisense oligonucleotide for the treatment of spinal muscular atrophy. *Journal of Pediatric Pharmacology and Therapeutics* vol. 24 (2019).

22. Claborn, M. K., Stevens, D. L., Walker, C. K. & Gildon, B. L. Nusinersen: A Treatment for Spinal Muscular Atrophy. *Annals of Pharmacotherapy* vol. 53 (2019).

23. Li, Q. Nusinersen as a therapeutic agent for spinal muscular atrophy. *Yonsei Medical Journal* vol. 61 (2020).

24. Qian, L. Therapeutic Effects of R-IDARAM and Intrathecal Immunochemotherapy on Elderly Patients with PCNSL. *ClinicalTrials.gov Identifier: NCT02836158* https://clinicaltrials.gov/ct2/show/NCT02836158?term=intrathecal&recrs=a&draw=1&rank=1 (2016).

25. Qian, L. Treatment of PCNSL WIth R-IDARAM and Intrathecal Immunochemotherapy. *ClinicalTrials.gov Identifier: NCT02657785* https://clinicaltrials.gov/ct2/show/NCT02657785?term=intrathecal&recrs=a&draw=1&rank=2 (2016).

26. Qian, J. Intrathecal Chemotherapy for Central Nervous System Metastasis in Retinoblastoma. *ClinicalTrials.gov Identifier: NCT04903678* https://clinicaltrials.gov/ct2/show/NCT04903678?term=intrathecal&recrs=a&draw=1&rank=5 (2021).

27. Kurtzberg, J. UCB Transplant of Inherited Metabolic Diseases With Administration of Intrathecal UCB Derived Oligodendrocyte-Like Cells (DUOC-01). . *ClinicalTrials.gov Identifier: NCT02254863* https://clinicaltrials.gov/ct2/show/NCT02254863?term=intrathecal&recrs=a&draw=2&rank=11 (2014).

28. Rong, L. Intrathecal Transplantation of UC-MSC in Patients With Late Stage of Chronic Spinal Cord Injury. *ClinicalTrials.gov Identifier: NCT03505034* (2018).

29. Staff, N. Intrathecal Autologous Adipose-derived Mesenchymal Stromal Cells for Amyotrophic Lateral Sclerosis (ALS). *ClinicalTrials.gov Identifier: NCT03268603* (2017).

30. Rong, L. Intrathecal Transplantation of UC-MSC in Patients With Sub-Acute Spinal Cord Injury. *ClinicalTrials.gov Identifier: NCT03521336* (2018).

31. Rong, L. Intrathecal Transplantation of UC-MSC in Patients With Early Stage of Chronic Spinal Cord Injury. *ClinicalTrials.gov Identifier: NCT03521323* (2018).

32. Prodromos, C. Safety of Cultured Allogeneic Adult Umbilical Cord Derived Mesenchymal Stem Cell Intrathecal Injection for ALS. *ClinicalTrials.gov Identifier: NCT05003921* (2021).

33. Lu, X. Autologous Bone Marrow-derived Mononuclear Cells for Acute Spinal Cord Injury. *ClinicalTrials.gov Identifier: NCT04528550* (2020).

34. Sehgal, A. First-in-Human Study of TSHA-101 Gene Therapy for Treatment of Infantile Onset GM2 Gangliosidosis. *ClinicalTrials.gov Identifier: NCT04798235* (2021).

35. Study of Intrathecal Administration of Onasemnogene Abeparvovec-xioi for Spinal Muscular Atrophy. *ClinicalTrials.gov Identifier: NCT03381729* (2021).

36. McCarthy, T. & Charlesworth, D. FDA Approves Brineura (cerliponase alfa) for the Treatment of CLN2 Disease, a Form of Batten Disease and Ultra-Rare Pediatric Brain Disorder in Children . *ClinicalTrials.gov: NCT02963350* (2017).

37. Khani, M. *et al.* Characterization of intrathecal cerebrospinal fluid geometry and dynamics in cynomolgus monkeys (macaca fascicularis) by magnetic resonance imaging. *PLoS ONE* **14**, (2019).

38. Jose, D. A., Luciano, P., Vicente, V., Juan Marcos, A. S. & Gustavo, F. C. Role of catheter's position for final results in intrathecal drug delivery. Analysis based on CSF dynamics and specific drugs profiles. *Korean Journal of Pain* vol. 26 (2013).

39. Martin, B. A. & Heidari Pahlavian, S. Anatomy and Physiology of Cerebrospinal Fluid Dynamics. in *Nervous System Drug Delivery: Principles and Practice* 73–89 (Elsevier, 2019). doi:10.1016/B978-0-12-813997-4.00005-0.

40. Yildiz, S. *et al.* Quantifying the influence of respiration and cardiac pulsations on cerebrospinal fluid dynamics using real-time phase-contrast MRI. *Journal of Magnetic Resonance Imaging* **46**, 431–439 (2017).

41. Engelhardt, B. & Coisne, C. Fluids and barriers of the CNS establish immune privilege by confining immune surveillance to a two-walled castle moat surrounding the CNS castle. *Fluids and Barriers of the CNS* vol. 8 (2011).

42. Freedman, M. S. *et al.* Recommended standard of cerebrospinal fluid analysis in the diagnosis of multiple sclerosis: A consensus statement. *Archives of Neurology* vol. 62 (2005).

43. Hatterer, E., Touret, M., Belin, M. F., Honnorat, J. & Nataf, S. Cerebrospinal fluid dendritic cells infiltrate the brain parenchyma and target the cervical lymph nodes under neuroinflammatory conditions. *PLoS ONE* **3**, (2008).

44. Simon, M. J. & Iliff, J. J. Regulation of cerebrospinal fluid (CSF) flow in neurodegenerative, neurovascular and neuroinflammatory disease. *Biochimica et Biophysica Acta - Molecular Basis of Disease* vol. 1862 (2016).

45. Hårdemark, H. G. *et al.* Neuron-specific enolase is a marker of cerebral ischemia and infarct size in rat cerebrospinal fluid. *Stroke* **19**, (1988).

46. Zetterberg, H., Smith, D. H. & Blennow, K. Biomarkers of mild traumatic brain injury in cerebrospinal fluid and blood. *Nature Reviews Neurology* **9**, (2013).

47. Klimo, P., Kestle, J. R. W., Macdonald, J. D. & Schmidt, R. H. Marked reduction of cerebral vasospasm with lumbar drainage of cerebrospinal fluid after subarachnoid hemorrhage. *Journal of Neurosurgery* **100**, (2004).

48. del Bigio, M. R. Ependymal cells: Biology and pathology. *Acta Neuropathologica* vol. 119 (2010).

49. Myers, M. R. A numerical investigation into factors affecting anesthetic distribution during spinal anesthesia. *Journal of Biomechanics* **29**, (1996).

50. Tangen, K. M., Hsu, Y., Zhu, D. C. & Linninger, A. A. CNS wide simulation of flow resistance and drug transport due to spinal microanatomy. *Journal of Biomechanics* **48**, (2015).

51. Tangen, K. M., Leval, R., Mehta, A. I. & Linninger, A. A. Computational and in vitro experimental investigation of intrathecal drug distribution: Parametric study of the effect of injection volume, cerebrospinal fluid pulsatility, and drug uptake. *Anesthesia and Analgesia* **124**, (2017).

52. Hsu, Y., Hettiarachchi, H. D. M., Zhu, D. C. & Linninger, A. A. The frequency and magnitude of cerebrospinal fluid pulsations influence intrathecal drug distribution: Key factors for interpatient variability. *Anesthesia and Analgesia* **115**, (2012).

53. Haga, P. T. *et al.* A numerical investigation of intrathecal isobaric drug dispersion within the cervical subarachnoid space. *PLoS ONE* **12**, (2017).

54. Kuttler, A. *et al.* Understanding pharmacokinetics using realistic computational models of fluid dynamics: Biosimulation of drug distribution within the CSF space for intrathecal drugs. in *Journal of Pharmacokinetics and Pharmacodynamics* vol. 37 (2010).

55. Hocking, G. & Wildsmith, J. A. W. Intrathecal drug spread. *British Journal of Anaesthesia* vol. 93 (2004).

56. Sass, L. R. *et al.* A 3D subject-specific model of the spinal subarachnoid space with anatomically realistic ventral and dorsal spinal cord nerve rootlets. *Fluids and Barriers of the CNS* **14**, (2017).

57. Khani, M. *et al.* Anthropomorphic Model of Intrathecal Cerebrospinal Fluid Dynamics Within the Spinal Subarachnoid Space: Spinal Cord Nerve Roots Increase Steady-Streaming. *Journal of Biomechanical Engineering* **140**, (2018).

58. Huang, T. Y. *et al.* Supratentorial cerebrospinal fluid production rate in healthy adults: Quantification with two-dimensional cine phase-contrast MR imaging with high temporal and spatial resolution. *Radiology* **233**, (2004).

59. Brinker, T., Stopa, E., Morrison, J. & Klinge, P. A new look at cerebrospinal fluid circulation. *Fluids and Barriers of the CNS* vol. 11 (2014).

60. Liu, G. *et al.* Direct Measurement of Cerebrospinal Fluid Production in Mice. *Cell Reports* **33**, (2020).

61. Bagger, M. A. & Bechgaard, E. The potential of nasal application for delivery to the central brain - A microdialysis study of fluorescein in rats. *European Journal of Pharmaceutical Sciences* **21**, (2004).

62. Aaron, J.-J. & Trajkovska, S. Fluorescence Studies of Anti-Cancer Drugs - Analytical and Biomedical Applications. *Current Drug Targets* **7**, (2006).

63. Sun, Y., Nakashima, M. N., Takahashi, M., Kuroda, N. & Nakashima, K. Determination of bisphenol A in rat brain by microdialysis and column switching high-performance liquid chromatrography with fluorescence detection. *Biomedical Chromatography* **16**, (2002).

64. Tangen, K. *et al.* Clearance of Subarachnoid Hemorrhage from the Cerebrospinal Fluid in Computational and In Vitro Models. *Annals of Biomedical Engineering* **44**, (2016).

65. Khani, M. *et al.* Impact of Neurapheresis System on Intrathecal Cerebrospinal Fluid Dynamics: A Computational Fluid Dynamics Study. *Journal of Biomechanical Engineering* **142**, (2020).

66. Slavc, I. *et al.* Best practices for the use of intracerebroventricular drug delivery devices. *Molecular Genetics and Metabolism* **124**, (2018).

67. Chung, J. K., Brown, E., Crooker, B., Palmieri, K. J. & McCauley, T. G. Biodistribution of idursulfase formulated for intrathecal use (Idursulfase-IT) in cynomolgus monkeys after intrathecal lumbar administration. *PLoS ONE* **11**, (2016).

68. Hemley, S. J., Bilston, L. E., Cheng, S. & Stoodley, M. A. Aquaporin-4 expression and blood-spinal cord barrier permeability in canalicular syringomyelia: Laboratory investigation. *Journal of Neurosurgery: Spine* **17**, (2012).

69. Hinderer, C. *et al.* Widespread gene transfer in the central nervous system of cynomolgus macaques following delivery of AAV9 into the cisterna magna. *Molecular Therapy - Methods and Clinical Development* **1**, (2014).

70. Wolf, D. A. *et al.* Dynamic dual-isotope molecular imaging elucidates principles for optimizing intrathecal drug delivery. *JCI Insight* **1**, (2016).

71. Miller, T. *et al.* A Phase I, Randomised, First-in-Human Study of an Antisense Oligonucleotide Directed Against SOD1 Delivered Intrathecally in SOD1-Familial ALS Patients. *Lancet Neurology* **12**, (2013).

72. McRoberts, P. W., Pope, J. & Apostol, C. Reinstituting the bolus – New reasoning for an existing technique. *Pain Physician* vol. 20 (2017).

73. Hildebrand, K. R. *et al.* Characterization of Effect of Repeated Bolus or Continuous Intrathecal Infusion of Morphine on Spinal Mass Formation in the Dog. *Neuromodulation* **22**, (2019).

74. Buchser, E., Durrer, A., Chédel, D. & Mustaki, J. P. Efficacy of intrathecal bupivacaine: How important is the flow rate? *Pain Medicine* **5**, (2004).

75. Eisenach, J. C., Hood, D. D., Curry, R. & Shafer, S. L. Cephalad movement of morphine and fentanyl in humans after intrathecal injection. *Anesthesiology* **99**, (2003).

76. Flack, S. H. & Bernards, C. M. Cerebrospinal fluid and spinal cord distribution of hyperbaric bupivacaine and baclofen during slow intrathecal infusion in pigs. *Anesthesiology* **112**, (2010).

77. Eide, P. K. *et al.* Clinical application of intrathecal gadobutrol for assessment of cerebrospinal fluid tracer clearance to blood. *JCI Insight* **6**, (2021).

78. Halvorsen, M. *et al.* Off-label intrathecal use of gadobutrol: safety study and comparison of administration protocols. *Neuroradiology* **63**, (2021).

79. Edeklev, C. S. *et al.* Intrathecal use of gadobutrol for glymphatic MR imaging: Prospective safety study of 100 patients. *American Journal of Neuroradiology* **40**, (2019).

80. Ringstad, G. & Eide, P. K. Safety of Intrathecal Gadolinium-based Contrast Agents and Benefit versus Risk. *Radiology* vol. 299 (2021).

81. Watts, R., Steinklein, J. M., Waldman, L., Zhou, X. & Filippi, C. G. Measuring glymphatic flow in man using quantitative contrast-enhanced MRI. *American Journal of Neuroradiology* **40**, (2019).

82. Ringstad, G., Vatnehol, S. A. S. & Eide, P. K. Glymphatic MRI in idiopathic normal pressure hydrocephalus. *Brain* **140**, (2017).

83. Ringstad, G. *et al.* Brain-wide glymphatic enhancement and clearance in humans assessed with MRI. *JCI insight* **3**, (2018).

Chapter 3: Introduction to Spaceflight Associated Neuro-ocular Syndrome

3.1 Eye Anatomy

The human eye is the main organ of the visual system (Figure 3-1). The aqueous humor is the clear fluid filling space in the front of the eye between the lens and the cornea. The vitreous humor is the clear, gelatinous substance that fills the central cavity of the eye. The choroid is the blood vessel containing layer that lines the eye and is located between the retina and the sclera. The retina is the nerve layer lining at the back of the eye and is responsible for sensing light and generating electrical impulses that are sent to the brain. The sclera is the outer coat of the eye that surrounds the iris. The optic disk, referred to from here on out as the optic nerve head (ONH) is the point of exit for the ganglion cell axons leaving the eye. The optic nerve (ON) is a bundle of nerve fibers that carry the signals from the eye to the brain.

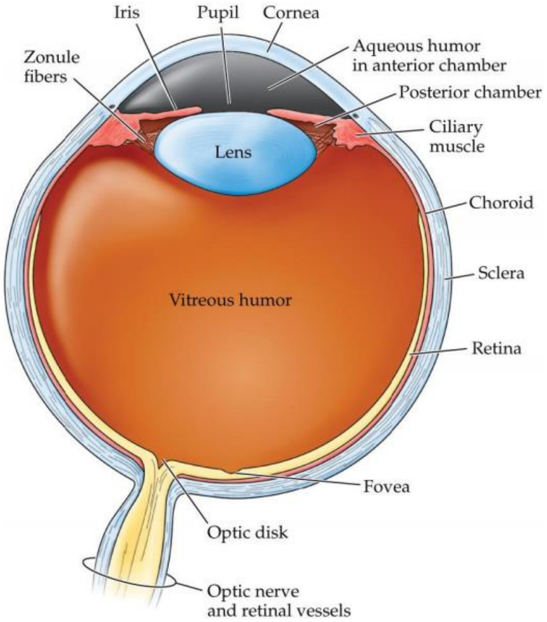

Figure 3-1. Human eye anatomy. The important features to note are the aqueous humor, vitreous humor, choroid, retina, sclera, and the optic nerve and optic nerve head, as these are the features that appear on the magnetic resonance imaging (MRI) scans.

3.2 Eye Anatomy in Magnetic Resonance Imaging

Magnetic resonance imaging (MRI) is the primary imaging method used in our research lab for the analysis of posterior globe flattening. In the MRI scans of the optic globe, only the fluid filled cavities appear. These include the aqueous and vitreous humor, and the CSF filled optic nerve sheath (ONS). However, other features are easily distinguishable. For instance, in Figure 3-2 the lens, ONH, and ON can be easily recognized: the lens is the dark space between the aqueous and vitreous humor;

the ONH is the center point between the end of the optic globe and the start of the optic nerve; and the ON is the dark space surrounded by ONS. These features are important for the MRI reformatting process.

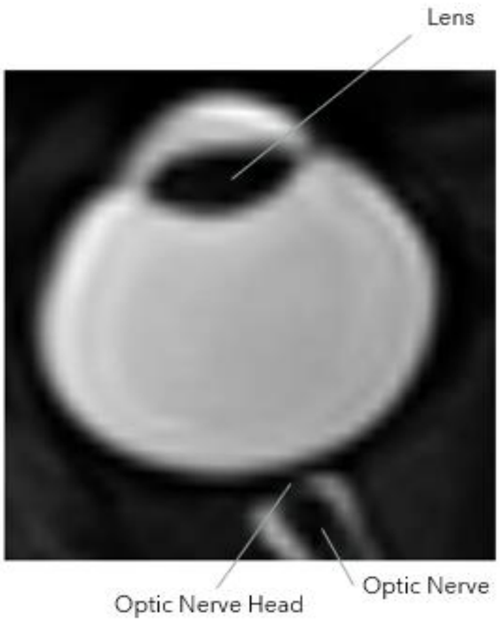

Figure 3-2. Eye anatomy in MRIs. As previously described, the lens, optic nerve head, and optic nerve, can be observed. Shown above is an ideal optic globe, as the foreground is easily distinguished from the background.

3.3 SANS Overview

The exact proportion of astronauts diagnosed with SANS has varied over time due to its ongoing, changing definition as new information has emerged, but has hovered around 40%. [1] Typically, unilateral and bilateral optic disc edema, choroidal and retinal folds, hyperopic refractive error shifts, focal areas of ischemic retina (cotton wool spots), and specifically, posterior globe flattening (Figure 3-3), are ophthalmic abnormalities that have been documented over the past decade in multiple reports associated with SANS. [2] Several imaging techniques, such as optical coherence tomography (OCT), ultrasonography, MRI, and cranial MRI have been used to document these findings. [2]

In some subjects, these findings have not resolved even long after return to Earth, though the severity of these symptoms may be dependent on spaceflight duration. [3,4] Therefore, a clearer understanding of the pathology of SANS and mitigation techniques are needed before long-term interplanetary expeditions are attempted.

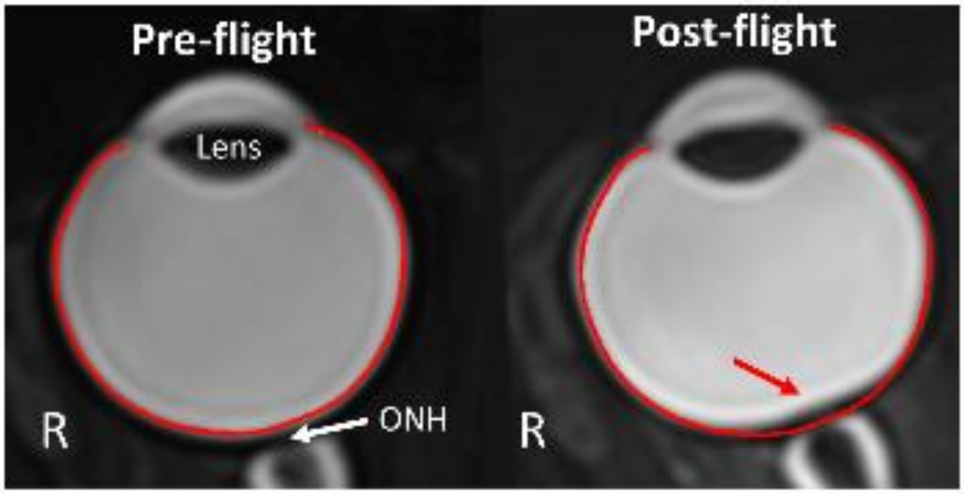

Figure 3-3. Posterior globe flattening. An MRI scan of the same right optic globe is shown. On the left, the preflight scan is shown. On the right, the postflight scan is shown. A preflight contour was generated and applied to the postflight scan.

3.4 Significance of Posterior Globe Flattening

Posterior globe flattening is defined by Lee et al. as: "when the convexity of the posterior sclera is reduced compared with the spherical shape of the remainder of the normal globe". [2] One study found that posterior globe flattening was present in 12 out of 52 astronauts following long duration spaceflight. Furthermore, the study also found that mild, bilateral posterior globe flattening was documented only 10 days into spaceflight. Lastly, in one case, posterior globe flattening was present for 7 years after return to Earth in three astronauts. [5]

Another study found that posterior globe flattening had the strongest diagnostic value of a terrestrial condition known as Idiopathic Intracranial Hypertension (IIH). [6] IIH is a disorder where the pressure in the brain is abnormally high, leading to many of the same symptoms as SANS. Because posterior globe flattening is present in a terrestrial and microgravity environment, it has been measured in head down tilt (HDT) participants and astronauts.

3.5 SANS Etiology

The cause of SANS has been extensively studied yet is not well understood. [1] Two basic hypotheses have been offered, but the prevailing theory suggests that a headward fluid shift that occurs in microgravity due to the loss of a hydrostatic pressure gradient is the main contributor of SANS (Figure 3-4). As a result of this headward fluid shift, the pressure inside a person's skull, referred to as the intracranial pressure (ICP), increases to a mild but chronic level. This elevation in ICP may result in the reversal of the trans-laminar pressure difference (TLPD) at the posterior eye.

Typically, the pressure inside the eye, called intraocular pressure, or IOP, is greater than ICP. When the TLPD is reversed, IOP becomes greater than ICP, leading to flattening of the sclera. [7, 8]

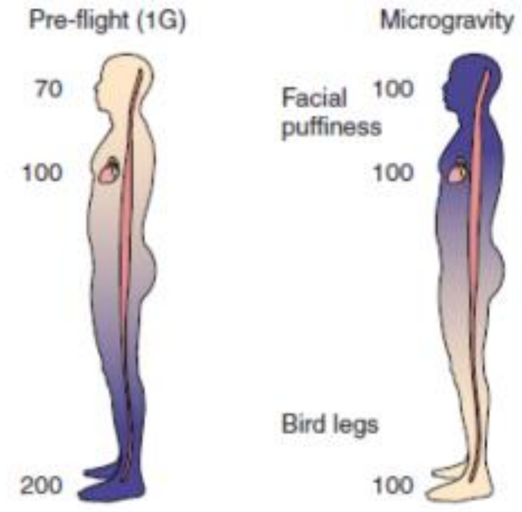

Figure 3-4. Fluid shift hypothesis. The human body has natural mechanisms in place to keep the CSF and other fluids in the brain, and fluids in lower body are influenced by gravity. However, in a microgravity environment, there is a fluid redistribution.

3.6 SANS and IIH

Both SANS and IIH are characterized by increased ICP, resulting in a decrease or even a reversal of the TLPD. Papilledema, a condition where the ON swells due to a buildup of pressure in the brain, and posterior globe flattening have both been observed in IIH and SANS. However, some common symptoms of IIH, including chronic headaches, transient visual obscurations, tinnitus, and diplopia have not been documented in astronauts. [9] These discrepancies suggest that SANS cannot be explained by increased ICP alone and is most likely multifactorial. [1]

3.7 Head Down Tilt Studies

One of the major limitations in studying the etiology of SANS is the prohibitive costs and capabilities of inflight monitoring. Currently, MRI scans cannot be taken inflight aboard the International Space Station (ISS). Because of this, head down tilt (HDT) studies are used as a spaceflight analog to investigate the development of the symptoms of SANS. Previous studies have shown that HDT showed good fidelity in simulating the fluid redistributions experienced in microgravity. [10, 11] The tilt angle, duration, and ambient environmental controls can vary from one HDT study to the next, but 6º is the most common because it produces a gravitational force of approximately -0.1 Gz. [12]

3.8 References

1. Lee AG, Mader TH, Gibson CR, Tarver W, Rabiei P, Riascos RF, et al. Spaceflight associated neuro-ocular syndrome (SANS) and the neuro-ophthalmologic effets of microgravity: a review and an update. *NPJ Microgravity* (2020).
2. Lee AG, Mader TH, Gibson CR, Brunstetter TJ, Tarver WJ. Space flight-associated neuro-ocular syndrome (SANS). Eye (Lond). 2018;32(7):1164-7. Epub 2018/03/13.
3. Macias BR, Patel NB, Gibson CR, Samuels BC, Laurie SS, Otto C, et al. Association of Long-Duration Spaceflight With Anterior and Posterior Ocular Structure Changes in Astronauts and Their Recovery. JAMA Ophthalmol. 2020. Epub 2020/04/03.
4. Mader TH, Gibson CR, Barratt MR, Miller NR, Subramanian PS, Killer HE, et al. Persistent Globe Flattening in Astronauts following Long-Duration Spaceflight. Neuro-Ophthalmology. 2020:1-7.
5. Shen Q, Cheng H, Pardue MT, Chang TF, Nair G, Vo VT, et al. Magnetic resonance imaging of tissue and vascular layers in the cat retina. J Magn Reson Imaging. 2006;23(4):465-72. Epub 2006/03/09.
6. Thomas H. Mader , C. Robert Gibson , Michael R. Barratt , Neil R. Miller , Prem S. Subramanian , Hanspeter E. Killer , William J. Tarver , Ashot E. Sargsyan , Kathleen Garcia , Stephen F. Hart , Larry A. Kramer , Roy Riascos , Tyson J. Brunstetter , William Lipsky , Peter Wostyn & Andrew G. Lee (2020): Persistent Globe Flattening in Astronauts following LongDuration Spaceflight, Neuro-Ophthalmology, DOI: 10.1080/01658107.2020.1791189.
7. Marshall-Goebel K, Mulder E, Bershad E, Laing C, Eklund A, Malm J, et al. Intracranial429and Intraocular Pressure During Various Degrees of Head-Down Tilt. Aerosp Med Hum Perform. 2017;88(1):10-6. Epub 2017/01/08.
8. Johannesson G, Eklund A, Linden C. Intracranial and Intraocular Pressure at the Lamina Cribrosa: Gradient Effects. Curr Neurol Neurosci Rep. 2018;18(5):25. Epub 2018/04/14.
9. Mader TH, Gibson CR, Miller NR, Subramanian PS,Patel NB, Lee AG. An overview of spaceflight-associated neuro-ocular syndrome (SANS). Neurol India. 2019;67(Supplement):S206-S11. Epub 2019/05/29.
10. Watenpaugh DE. Analogs of microgravity: head-down tilt and water immersion. J Appl Physiol (1985). 2016;120(8):904-14. Epub 2016/02/13.
11. Schneider SM, Lee SM, Feiveson AH, Watenpaugh DE, Macias BR, Hargens AR. Treadmill exercise within lower body negative pressure protects leg lean tissue mass and extensor strength and endurance during bed rest. Physiol Rep. 2016;4(15).
12. Nelson ES, Myers JG, Jr., Lewandowski BE, Ethier CR, Samuels BC. Acute effects of posture on intraocular pressure. PLoS One. 2020;15(2):e0226915. Epub 2020/02/07.

Chapter 4: Quantification of Ophthalmic Changes

Citation: Sater Stuart H., Sass Austin M., Seiner Akari, Natividad Gabryel Conley, Shrestha Dev, Fu Audrey Q., Oshinski John N., Ethier C. Ross and Martin Bryn A. 2021 MRI-based quantification of ophthalmic changes in healthy volunteers during acute 15° head-down tilt as an analogue to microgravity. J. R. Soc. Interface. **18:** 20200920. 20200920.

4.1 Introduction

Extended spaceflight is known to result in abnormal physiologic adaptations in humans. For instance, musculoskeletal deconditioning and cardiovascular adaptations have been extensively studied and they have pathologies that are relatively well defined. [1-4] More recently, neuro-ocular functional and structural changes have been identified in a condition referred to as Spaceflight Associated Neuro-ocular Syndrome (SANS). [5] Crewmembers with SANS often present with choroidal folds, hyperopic shifts, posterior globe flattening, and optic disc edema. These effects can persist long after return to Earth, although some recovery has been shown to occur. [6-10] SANS increases the risk associated with 6-month missions to the International Space Station (ISS), requiring mitigation before long-term space habitation or interplanetary expeditions are attempted.

SANS pathophysiology has been studied extensively yet is not well understood. [11] A prevailing theory suggests that cephalad fluid shifts occurring in microgravity result in mild but chronically elevated intracranial pressure (ICP) that elicits adaptations of ophthalmic structures, including distension of the bulbar region of the optic nerve sheath (ONS). [12, 13] Significant increases in ICP may also result in a decrease in the trans-laminar pressure gradient, contributing to hyperopic shift and optic disc edema. [14, 15] This hypothesis has been supported by elevated lumbar puncture opening pressures postflight, [6] and some similarities in clinical signs and symptoms of SANS and idiopathic intracranial hypertension (IIH), such as papilledema and posterior globe flattening. [7] However, some common symptoms of IIH have not been documented in crewmembers, including chronic headache, transient visual obscurations, tinnitus, and diplopia. [16] The discrepancies between SANS and IIH suggest that the etiology of SANS cannot be explained by elevated ICP alone and is likely multifactorial, requiring further evaluation. [11]

To help evaluate the role of ICP in SANS, head-down tilt (HDT) studies have been routinely implemented to simulate the headward fluid redistributions experienced in microgravity. [17] However, microgravity has multiple physiological effects, and HDT is only a partial analogue of the more complex situation that occurs in microgravity. There is evidence suggesting that HDT overestimates the fluid shifts experienced under microgravity. For example, Laurie et al. found an overrepresentation of optic disc edema in subjects who participated in strict 6º HDT for 30 days (45%), when compared to the prevalence in astronauts (15%). [9] HDT studies can vary substantially in the tilt angle, duration, ambient environmental controls, use of anesthesia, and ICP measurement methodology (Table 4-1). [18-20]

The present study adds to previous work by utilizing a novel image processing technique to quantify changes to ophthalmic structures beyond the ONS under acute application of 15° HDT. Finite element biomechanical modeling was previously applied to the same set of subjects to estimate the stiffness of the ONS. [20] The present study applied a less sophisticated yet relevant method to estimate ONS stiffness from MR images. We hypothesized that features of elevated ICP would manifest under HDT in the form of ONS distension and decreased vitreous chamber depth. Changes in other parameters such as optic nerve (ON) cross-sectional area, ON deviation, and gaze angles were also assessed. The findings in this study can be compared to those from astronaut studies to identify similarities and differences between HDT and microgravity and will help further our understanding of the effects of ICP on ophthalmic structures.

4.2 Methods

4.2.1 MRI Protocol

High resolution MRI scans were collected from healthy volunteers on a 3 Tesla MRI scanner (Prisma, Siemens Healthineers, Malvern, PA), using a 20-channel receiving coil. MRI data collection for this study was approved by the Georgia Institute of Technology, Emory University, the University of Idaho, and NASA institutional review boards and adhered to the tenets of the Declaration of Helsinki. Written informed consent was obtained from all participants under IRB-approved protocol and all subjects were de-identified before data transfer to the University of Idaho for analysis. Identical scans were previously used in a study by Lee et al. [20] Each subject was scanned in a supine position after 30 minutes of acclimation. Supine scanning was followed by a 30-minute acclimation period in 15º HDT position before a second scan was obtained. Fifteen degrees was chosen to ensure a significant elevation in ICP, thus increasing the chance that observable changes in the ONS would occur, required for the ONS Young's modulus calculation. To minimize motion artifacts due to changes in gaze angles during MRI scans, subjects were instructed to focus on a visual target central to their field of view. For quantification of ON and ONS cross-sectional areas, vitreous chamber depth, and ONS Young's modulus, T2-weighted oblique coronal images were collected with 600 μm slice thickness and spacing, and 253 μm in-plane isotropic pixel size (field of view (FOV) 65 cm^2) (Figure 4-1A). Additional sequence parameters included 170º flip-angle, 820 ms repetition time, and 118 ms echo time. For quantification of ON deviation and gaze angles, T1-weighted sagittal images were collected with 900 μm slice thickness and spacing, and 488 μm isotropic pixel size (FOV 250 x 250 pixels). Additional sequence parameters included a 9º flip-angle, 1900 ms repetition time, and 2.32 ms echo time.

Table 4-1. Summary of prior HDT and astronaut studies. Comparison table of related studies that includes details on the study name, study subjects, experimental conditions, the inclusion of ICP measurements, use of anesthesia, and key findings.

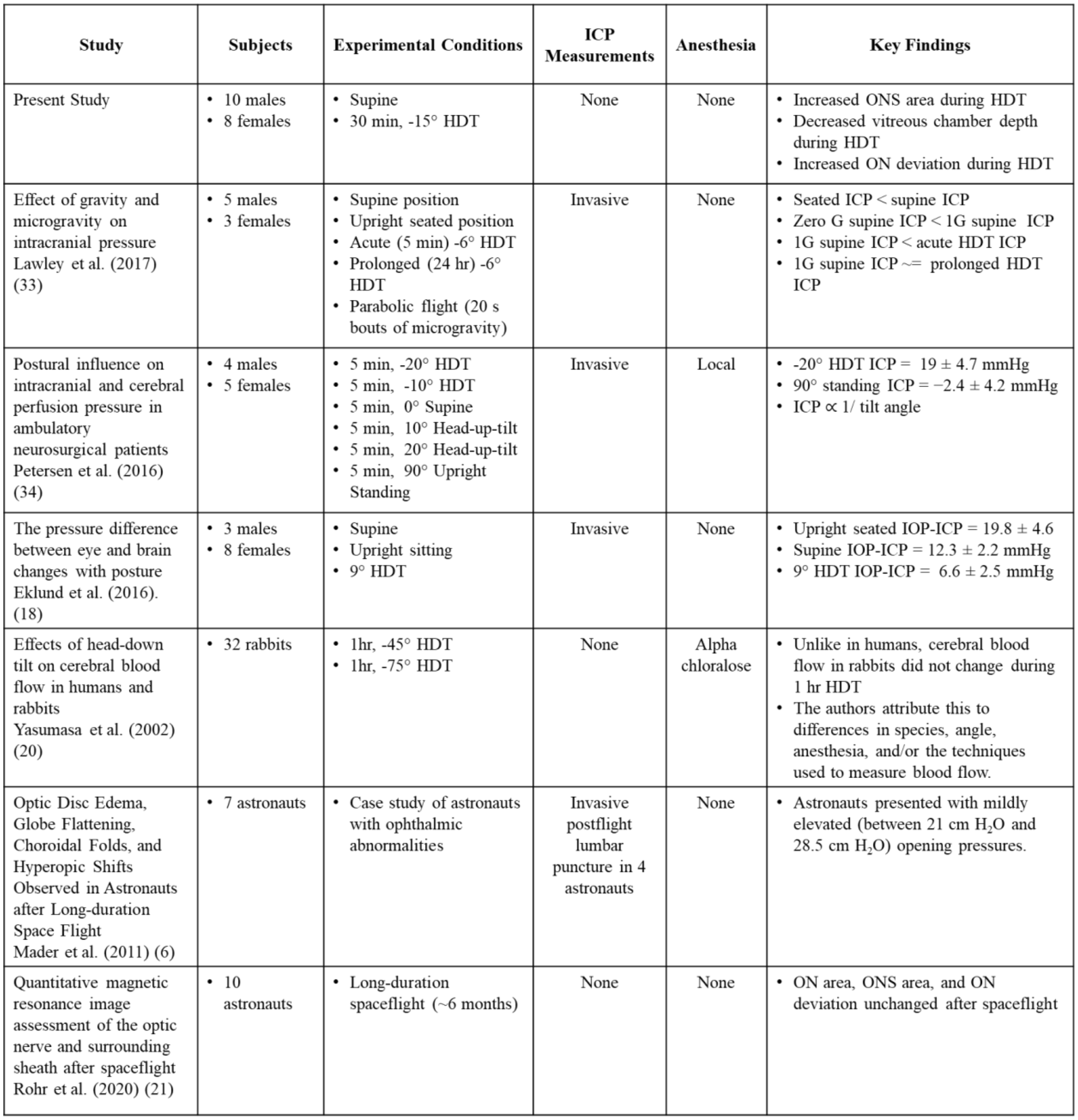

Study	Subjects	Experimental Conditions	ICP Measurements	Anesthesia	Key Findings
Present Study	• 10 males • 8 females	• Supine • 30 min, -15° HDT	None	None	• Increased ONS area during HDT • Decreased vitreous chamber depth during HDT • Increased ON deviation during HDT
Effect of gravity and microgravity on intracranial pressure Lawley et al. (2017) (33)	• 5 males • 3 females	• Supine position • Upright seated position • Acute (5 min) -6° HDT • Prolonged (24 hr) -6° HDT • Parabolic flight (20 s bouts of microgravity)	Invasive	None	• Seated ICP < supine ICP • Zero G supine ICP < 1G supine ICP • 1G supine ICP < acute HDT ICP • 1G supine ICP ~= prolonged HDT ICP
Postural influence on intracranial and cerebral perfusion pressure in ambulatory neurosurgical patients Petersen et al. (2016) (34)	• 4 males • 5 females	• 5 min, -20° HDT • 5 min, -10° HDT • 5 min, 0° Supine • 5 min, 10° Head-up-tilt • 5 min, 20° Head-up-tilt • 5 min, 90° Upright Standing	Invasive	Local	• -20° HDT ICP = 19 ± 4.7 mmHg • 90° standing ICP = −2.4 ± 4.2 mmHg • ICP $\propto$ 1/ tilt angle
The pressure difference between eye and brain changes with posture Eklund et al. (2016). (18)	• 3 males • 8 females	• Supine • Upright sitting • 9° HDT	Invasive	None	• Upright seated IOP-ICP = 19.8 ± 4.6 • Supine IOP-ICP = 12.3 ± 2.2 mmHg • 9° HDT IOP-ICP = 6.6 ± 2.5 mmHg
Effects of head-down tilt on cerebral blood flow in humans and rabbits Yasumasa et al. (2002) (20)	• 32 rabbits	• 1hr, -45° HDT • 1hr, -75° HDT	None	Alpha chloralose	• Unlike in humans, cerebral blood flow in rabbits did not change during 1 hr HDT • The authors attribute this to differences in species, angle, anesthesia, and/or the techniques used to measure blood flow.
Optic Disc Edema, Globe Flattening, Choroidal Folds, and Hyperopic Shifts Observed in Astronauts after Long-duration Space Flight Mader et al. (2011) (6)	• 7 astronauts	• Case study of astronauts with ophthalmic abnormalities	Invasive postflight lumbar puncture in 4 astronauts	None	• Astronauts presented with mildly elevated (between 21 cm H_2O and 28.5 cm H_2O) opening pressures.
Quantitative magnetic resonance image assessment of the optic nerve and surrounding sheath after spaceflight Rohr et al. (2020) (21)	• 10 astronauts	• Long-duration spaceflight (~6 months)	None	None	• ON area, ONS area, and ON deviation unchanged after spaceflight

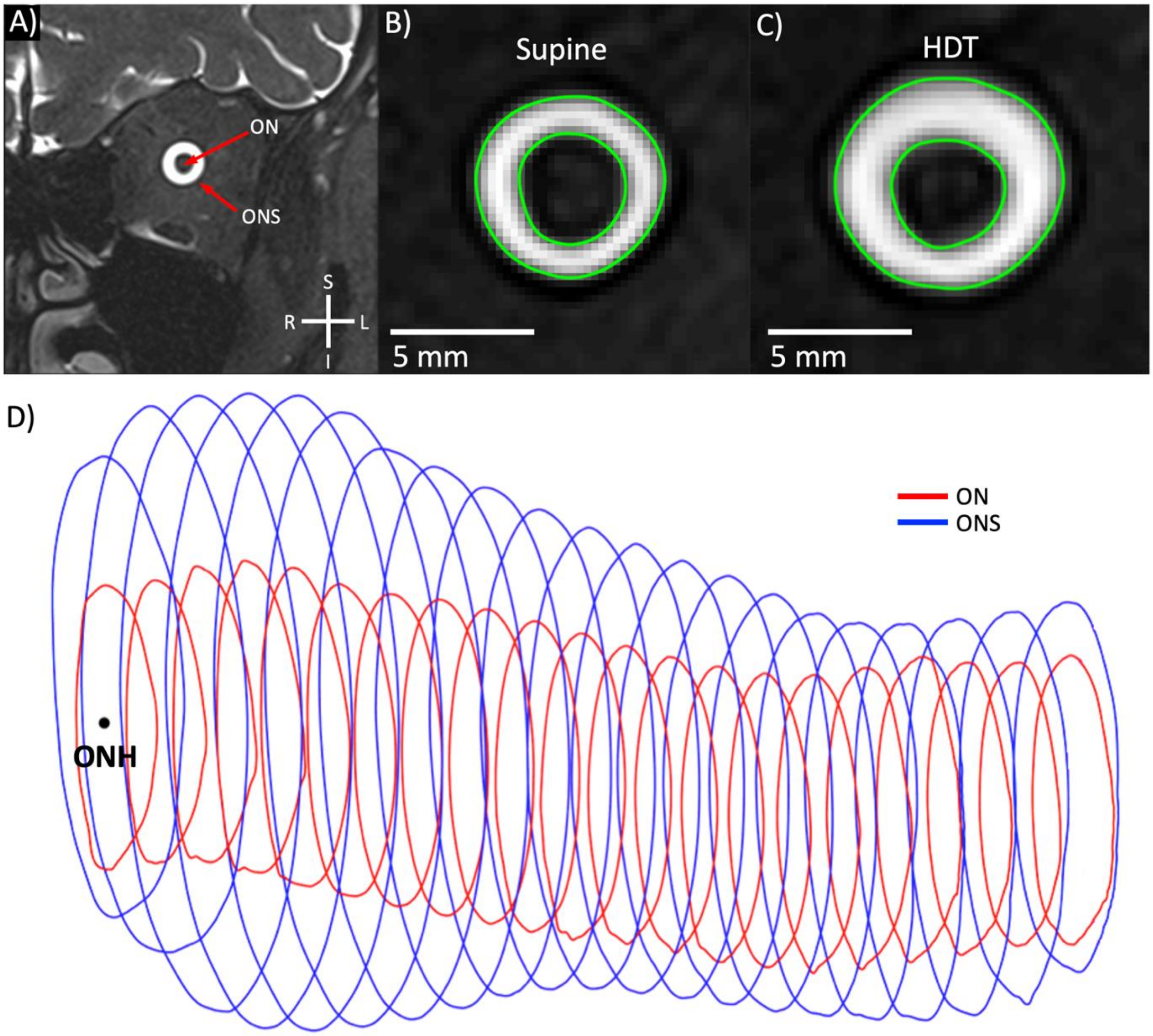

Figure 4-1. ON and ONS Cross Sectional Area Parameters. Methods for analysis of ON and ONS areas showing (A) example coronal MRI with ON and ONS labeled, (B) supine and (C) HDT contours resulting from largest ONS area changes, (D) 3D ON/ONS trajectory.

4.2.2 ON and ONS Cross Sectional Area, Vitreous Chamber Depth, and ONS Young's Modulus Estimation

Three-dimensional geometries of the ONS and ON were generated using a semi-automated method previously described by Rohr et al. [21] In brief, average background pixel intensity for each scan was selected with a slice-by-slice mask relative to the peak frequency in the pixel intensity histogram, with the intensity ranging from 0 to 4095 (12-bit image). A global threshold was computed and used to contour each MRI slice and contours were filtered based on an isoperimetric difference quotient and point count threshold (Figure 4-1 B, C). Linear interpolation between contours (600 μm slice spacing) was applied to obtain the inner and outer contour of the bulbar subarachnoid space located 3 mm posterior to the ONH along the ON trajectory. This 3 mm posterior outer and inner contour was used to quantify the ONS and ON cross sectional areas (Figure 4-1D). This contour was chosen to be consistent with standard ultrasound procedures in which ONS diameter is measured at 3mm posterior to the ONH, an area of maximum contrast. [22]

We measured the change in vitreous chamber depth under HDT as a quantitative indirect indicator of globe flattening. Specifically, we manually measured the distance between the ONH and lens center from T1-weighted MRIs. A negative change in vitreous chamber depth under HDT represented shortening of the vitreous chamber. The lens center and ONH locations were identified in 3D based on multiplanar visual inspection. The lens center was identified as the centroid of the lens and the ONH was identified as the interface between the centerline of the ON and the outermost boundary of posterior globe (Figure 4-2). The ONH point was located in the same way for both the vitreous chamber depth measurement and ON/ONS measurements, but these locations were not the same for all measurements and were identified on their respective scans.

ONS Young's modulus (E) was estimated at a location 3 mm posterior to the ONH utilizing the Law of Laplace assuming a thick-walled cylinder, namely $E = 3{r_i}^2 r_o \left(\frac{\Delta P}{2\Delta r_o}\right) / ({r_o}^2 - {r_i}^2)$, with inner ($r_i$) and outer radii ($r_o$) of the ONS measured in the supine position, and pressure change (ΔP) estimated at the optic axial plane as previously described by Lee et al. [20] Dura thickness (t) was specified as 0.4 mm; [23] thus, the outer radius was defined as $r_o = r_i + 0.4\ mm$. [20]

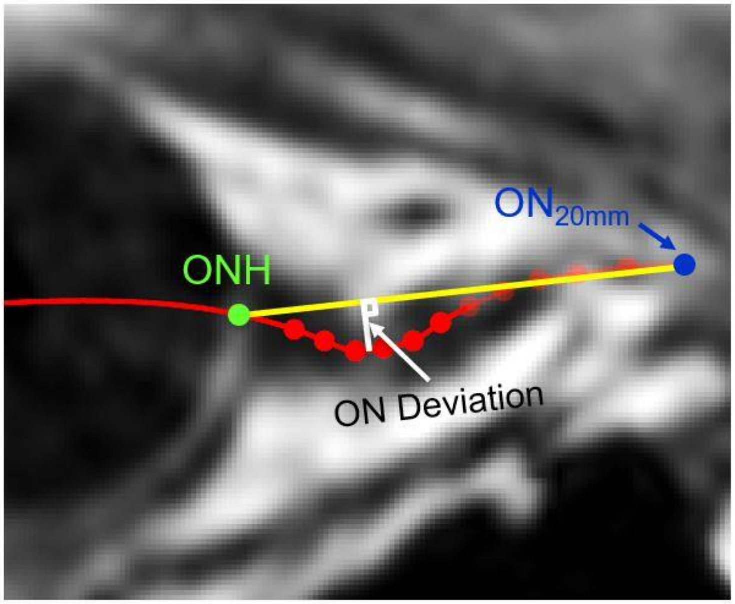

Figure 4-2. ON Deviation Analysis. Manual selection of the ON centerline trajectory (red) and the straight line trajectory (yellow) that connects the ONH (green) and the location on the ON 20 mm posterior to the ONH (blue).

4.2.3 ON Deviation and Gaze Angle Quantification

The maximum orthogonal distance between the curved ON trajectory and a straight line trajectory was used to determine ON deviation and is based on the methods described by Rohr et al (Figure 4-2). [24] In brief, >20 mm of the centerline trajectory of the ON was manually selected with ~1 to 2 mm point spacing using MPR visualization of the T1-weighted MRI sequence described above. The trajectory was up-sampled using spline curve fitting and truncated at 20 mm posterior to the ONH. A trajectory length of 20 mm was used because it includes the region of ON kinking previously reported to be present in astronauts. [7] Manual selections were performed by two operators and then cross-inspected by each operator to confirm data point selection. Operators were blind to subject identity but were not blind to body posture. Inter and intra-operator reliability was previously found to be good for these methods. [21]

Lateral and vertical gaze angles for the left and right eye were quantified with reference to the Frankfort horizontal plane [24] (Figure 4-3A) to determine whether changes in ophthalmic structures were attributable to changes in gaze between supine and HDT postures. Positive and negative lateral gaze values were defined as projections directed in the left and right anatomical field of view. Positive and negative vertical gaze values were similarly defined as projections directed in the field of view superior and inferior to the Frankfort horizontal plane (Figure 4-3B).

4.2.4 Statistics

A linear mixed-effects model that accounts for repeated measurements from the same individual was developed:

$$y_i = \beta_0 + \beta_1 x_{1i} + \beta_2 x_{2i} + \beta_3 x_{3i} + \beta_4 x_{4i} + \beta_5 x_{5i} + z_{0i} + z_{1i} x_{2i} + \epsilon_i$$

where y_i is the measurement of a parameter of interest, β_0 is the baseline (left eye of a male subject in supine position), x_{1i} is the posture group of HDT, x_{2i} denotes the right eye, x_{3i}, x_{4i}, and x_{5i} are the age, body mass index (BMI), and sex (female) of the *i*th subject, respectively. While coefficient β represents fixed effect sizes, coefficient z represents the random effects and follows a multivariate normal distribution with mean of 0 and a symmetric variance-covariance matrix:

$$\begin{pmatrix} z_{0i} \\ z_{1i} \end{pmatrix} \sim N\left(\begin{pmatrix} 0 \\ 0 \end{pmatrix}, \begin{pmatrix} \sigma_0^2 & \sigma_{01} \\ \sigma_{01} & \sigma_1^2 \end{pmatrix}\right).$$

The “*fitlme*” function in Matlab (Ver. R2019a Mathworks Corp., Natick, MA) was used to estimate the coefficients and variances in this linear mixed-effects model and test the hypotheses.

This model treats the subjects as random with repeated measurements (on the left and right eye), which allows us to account for the variability across subjects and dependence between the two eyes for each subject. It takes posture group, eye, age, BMI, and sex as fixed effects, with the corresponding coefficient indicating the effect size. We further tested whether the true effect size was significantly different from zero, which implies that there was a statistically significant difference in the associated parameter between the two posture groups or between the two eyes, or that there was a statistically significant impact of age, BMI, or sex on the parameter of interest.

Using this linear mixed-effects model, we calculated p-values for the following 6 parameters: ON area, ONS area, ON deviation, lateral gaze angle, vertical gaze angle, and vitreous chamber depth. Some of these p-values were dependent due to dependence among several parameters of interest. We ignored such dependence and accounted for multiple comparison with Bonferroni correction, in order to derive more conservative results. To apply Bonferroni correction, we adjusted the threshold for p values to be α/m, where α is the experimentwise type I error rate and m is the number of p values under consideration. With six parameters and five fixed-effect sizes per parameter, we have $m = 30$, and we considered an $\alpha = 0.10$.

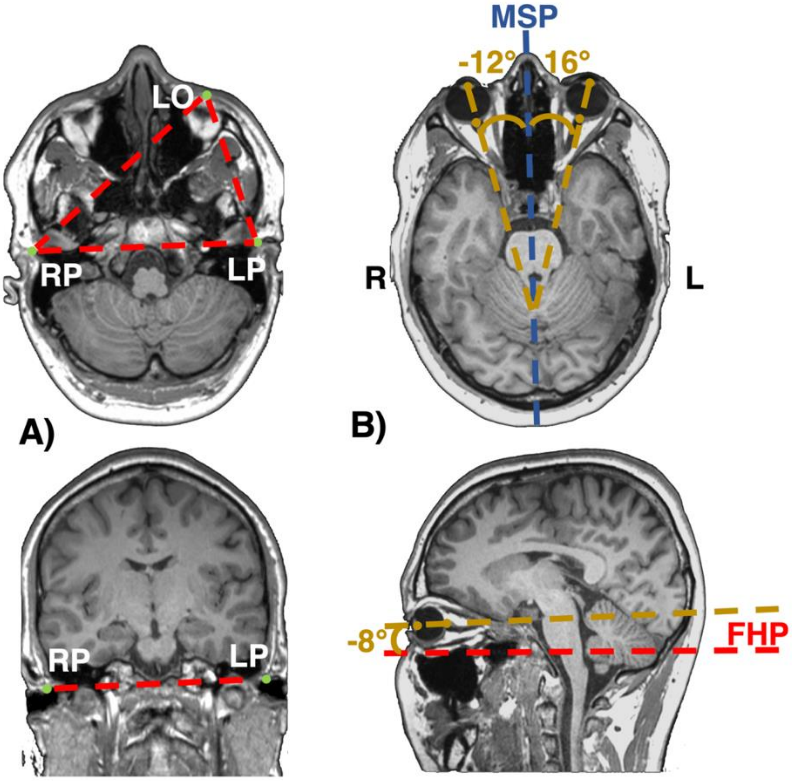

Figure 4-3. Frankfort Plane and Gaze Angle Calculations. Lateral and vertical gaze angles were measured with respect to the Frankfort horizontal plane of the skull.

4.3 Results

MR images were collected at supine and 15º HDT for 18 subjects (10 Males, 8 Females) with average height, weight, and age of 1.63 ± 0.37 m, 67.5 ± 18.3 kg, and 29 ± 12 years, respectively. A summary of all parameter results can be found in Table 4-2. One subject was omitted from the ON and ONS cross-sectional area analysis and two subjects were omitted from the remaining analyses due to motion artifacts in the images.

Table 4-2. Summary of Quantified Chagnes Occurring Under HDT. The parameter of interest, mean measurements in the supine and HDT position, 95% confidence interval and statistical significance is shown.

Parameter	**Supine Mean**	**HDT Mean**	**Mean Change**	**95% CI**	**p-value**	**N, eyes**
ON Cross-sectional Area (mm^2)	9.41	9.49	0.15	-0.12 to 0.43	0.271	17, 33
ONS Cross-sectional Area (mm^2)	29.15	32.33	4.04	2.88 to 5.21	0.000	17, 33
ON Deviation (mm)	1.55	1.75	0.20	0.08 to 0.33	0.002	16, 32
Lateral Gaze Angle (degrees)	-2.46	-1.39	0.89	-0.39 to 2.19	0.169	16, 32
Vertical Gaze Angle (degrees)	-5.75	-5.41	0.10	1.85 to 2.04	0.921	16, 32
Vitreous Chamber Depth (mm)	19.72	19.55	-0.11	-0.21 to -0.03	0.009	16, 32

4.3.1 ON and ONS Cross Sectional Areas and ONS Young's Modulus Estimation

There was a moderate linear correlation ($R^2 = 0.64$) of ON cross-sectional area between supine and HDT postures (Figure 4-4A). Change in the cross-sectional area of the ON due to postural change was insignificant, with an average change of 0.15 mm^2 (95% CI -0.12 mm^2 to 0.43 mm^2, p = 0.271). ONS areas tended to increase during HDT for the majority of subjects excluding a few cases with minimal change (Figure 4-5D). Average change in ONS cross-sectional area was 4.04 mm^2 (95% CI 2.88 mm^2 to 5.21 mm^2, p < 0. 000). There was strong linear correlation ($R^2 = 0.81$) in ONS area between supine and HDT postures.

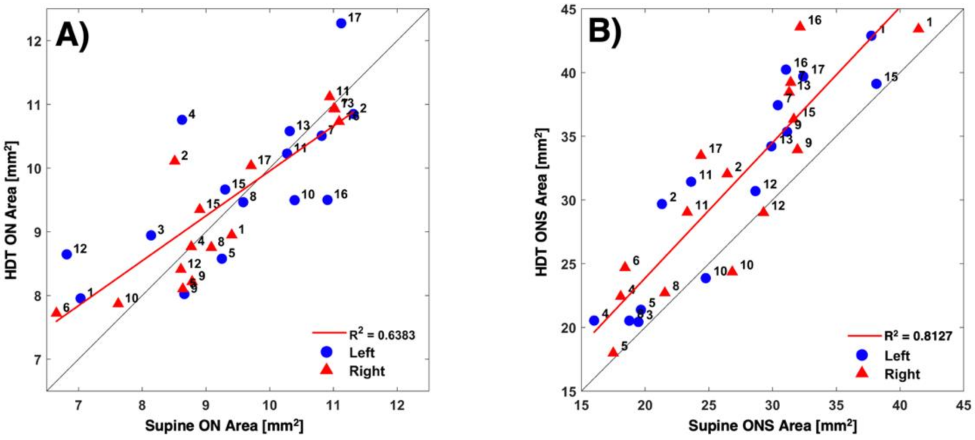

Figure 4-4. Concordance Plots for ON and ONS Area Parameters. (A) ON and (B) ONS cross sectional areas at 3 mm posterior to the ONH under supine and HDT conditions. Linear regression is shown in red. Blue circles and red triangles represent left and right eyes.

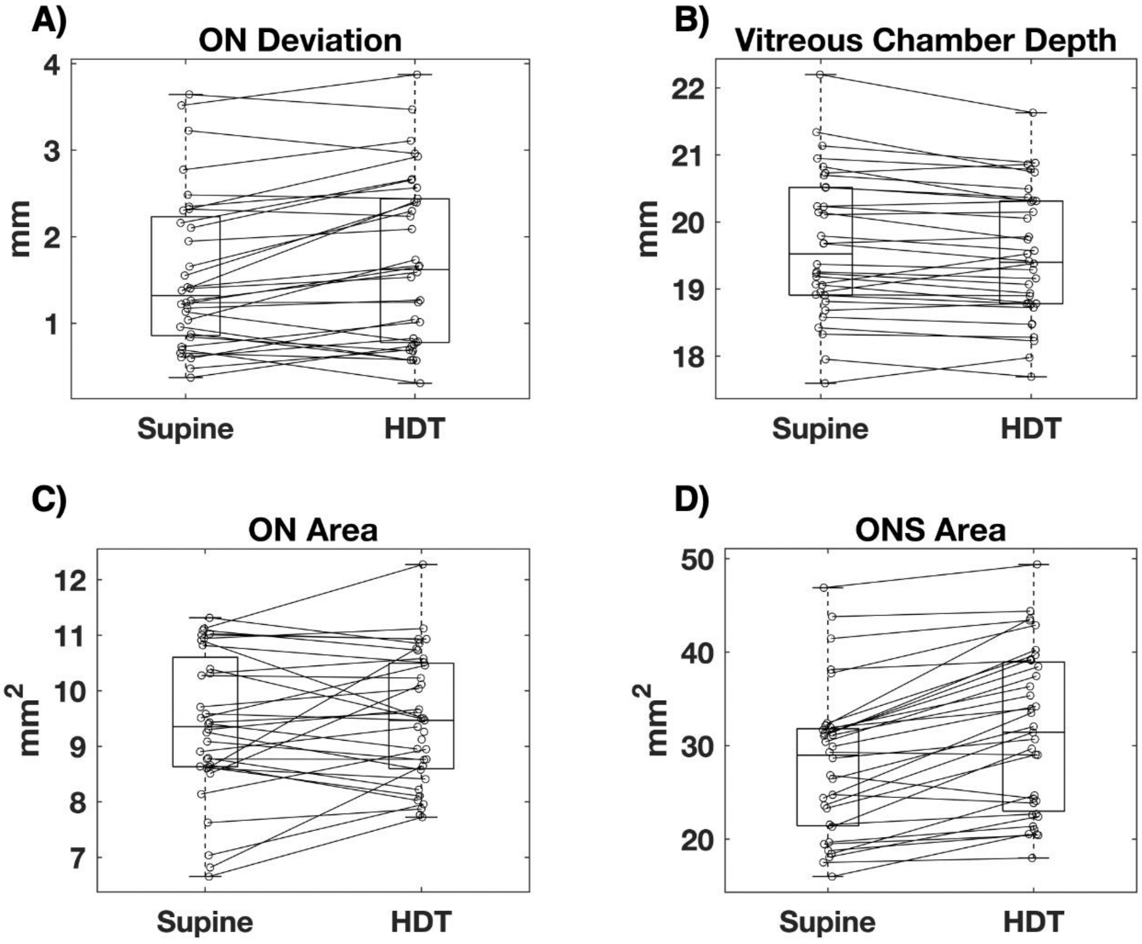

Figure 4-5. Boxplots for ON Deviation, Vitreous Chamber Depth, ON area, and ONS Area During Supine and HDT. (A) ON deviation, (B) Vitreous chamber depth, (C) ON area, (D) ONS area.

Young's Modulus for the ONS at a location 3 mm posterior to the ONH was estimated for 16 subjects (N = 29 eyes). Subjects were omitted when ONS area was unchanged or decreased during HDT, since the estimate for modulus becomes undefined in such situations. The mean and standard deviation of ONS Young's modulus was 85.0 ± 115.7 kPa.

4.3.2 ON Deviation, Gaze Angles, and Vitreous Chamber Depth

ON deviation, Gaze Angles, and Vitreous Chamber Depth were quantified in 16 of the 18 subjects (N = 32 eyes). ON deviation increased by an average of 0.20 mm when moving to HDT posture (95% CI 0.08 mm to 0.33 mm, p = 0.002) (Figure 4-5A). A strong linear correlation (R^2 = 0.86) between ON deviation in supine and HDT was observed (Figure 4-6A). Changes in lateral and vertical gaze angles (Figure 4-3B) were insignificant, with an average change in vertical gaze angle of 0.10° (95% CI -1.85° to 2.04°, p = 0.91) and an average change in lateral gaze angle of 0.89° (95% CI -0.39° to 2.19°, p = 0.169). Vitreous chamber depth showed an average change of -0.11mm (95% CI -

0.21 mm to -0.03 mm, p = 0.009) during HDT (Figure 4-5B). There was a strong linear correlation between supine and HDT measurements ($R^2 = 0.95$) and subjects with the largest supine vitreous chamber depths had the largest decreases under HDT (Figure 4-6B).

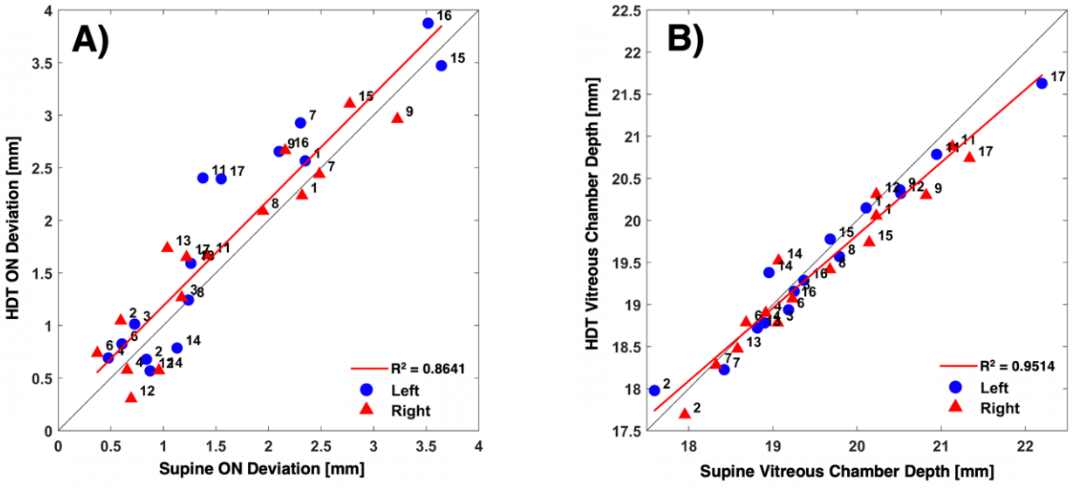

Figure 4-6. Concordance Plots of ON Deviation and Vitreous Chamber Depth. (A) ON deviation and (B) Vitreous Chamber Depth. Linear regression between both conditions is shown in red. Blue circles and red triangles represent left and right eyes, respectively.

4.3.3 Demographic Effects and Eye Unilaterality

All parameters were assessed for covariates including BMI, age, sex, and eye to determine whether any of the observed changes could be partially attributed to demographic differences or unilaterality. With Bonferroni correction at $\alpha = 0.10$, BMI accounted for a significant decrease in ON area, with an effect size of -0.14 mm^2 (p = 0.030) and a significant decrease in ON deviation with an effect size of -0.15 mm (p = 0.005). Females had a significant decrease of in ONS area with an effect size of -10.98 mm^2 ($p < 0.005$) and a significant decrease in vitreous chamber depth with an effect size of -1.39 mm (p = 0.003) when compared to males. A statistically significant difference in lateral gaze angle between the left and right eyes of 28.45° ($p < 0.000$) was present as a result of subjects focusing at a medial point in their field of view. All other covariates were insignificant including differences between the left and right eyes.

4.4 Discussion

Non-invasive automated and manual techniques were developed and applied to MR images to quantify changes in ophthalmic structures during acute HDT and to estimate Young’s modulus of the ONS. Three-dimensional reconstructions of the ON and ONS were generated to measure their cross-sectional areas at a location 3 mm posterior to the ONH. Changes in ONS area under due to HDT were used to estimate the mechanical properties of the ONS. The curved trajectory of the ON was manually defined to identify ON shape changes occurring to the ON under HDT. Vitreous chamber depth was measured as the distance between the manually selected lens center and the ONH locations. The ONS cross-sectional area was found to increase under HDT while the ON cross-sectional area remained unchanged. ON deviation was found to increase, an indication of increased tortuosity in HDT. While changes in lateral and vertical gaze angles were observed, no significant trends were identified between supine and HDT. A decrease in vitreous chamber depth suggests that acute application of HDT may contribute to alterations in the geometry of the optic globe. A thick-walled cylinder assumption of the law of Laplace was applied to estimate an average ONS Young's modulus of 85.0 kPa. The findings reported here can be compared to structural changes observed in astronauts to better understand the role of CSF redistribution in the development of SANS.

The ONS is known to be sensitive to changes in ICP due to communication between the orbital subarachnoid space surrounding the optic nerve and cranial subarachnoid space. [25] Thus, the ONS distension observed within the bulbar subarachnoid region suggests that CSF pressure was elevated during acute 15° HDT, as expected. The ONS distension observed in most subjects shows that the ONS can expand in response to elevated ICP; however, because of the nonlinear mechanical behavior of soft tissues, we expect that further increases in ICP would result in reduced or even negligible changes in ONS area. [26] It is possible that subjects who had little to no change in ONS cross-sectional area may have already had stiffened ONS tissues (e.g. due to elevated ICP) when in the supine position, so that ONS expansion was more difficult to detect by MRI. It is also possible that fluid communication within the subarachnoid space of the ON is different in different persons and that the trabeculae may affect pressure transmission along this path. However, we do not know the true reason why these subjects showed no change. The absence of changes in the ON cross-sectional area suggest that the ON is resistant to transmural fluid transport during acute pressure changes, such as due to acute HDT as used in this study. To our knowledge, this is the first study to measure ON area during HDT; however, ON area was also found to remain constant after long-duration spaceflight using identical methods to those reported here. [21]

ONS Young's modulus has been estimated using a variety of methods but almost exclusively *ex vivo*. However, Lee et al. used finite element modeling to estimate the *in vivo* stiffness of the ONS in the same subjects reported here, and found a mean Young's modulus of 47 kPa, [20] fairly similar to the Young's modulus we calculated in the subarachnoid region of the ONS. *Ex vivo* measurements of porcine ONS stiffness reported by Wang et al. are orders of magnitude greater (8.57 MPa vs 0.085 MPa). [27] This difference may be attributed to their use of uniaxial tensile testing in the axial direction that ignored the anisotropic nature of ONS tissue. The ONS is thought to be much more resistant to axial deformation than the circumferential deformation that was measured in this study. [28] It should be noted that the effects of the arachnoid trabecula within the subarachnoid space were not considered when estimating Young's modulus of the ONS. [29] Further, using the Law of Laplace for a thick-walled cylinder makes a number of assumptions that are not strictly satisfied, as discussed in detail by Lee et al. [20] However, it is a simple calculation and may be useful for obtaining approximate tissue properties *in vivo*.

Tortuosity and kinking of the ON has been observed in astronauts after long-duration spaceflight through the subjective analysis of postflight MR images. [7] However, the degree of change in ON tortuosity was not measured because baseline MR images were not collected in that study. More recent studies that include baseline comparisons did not identify significant changes in ON tortuosity [30] or ON deviation [21] after spaceflight. In contrast, the present study identified significant increases in ON deviation during HDT exposure, which may impose abnormal mechanical stresses on the ON and ONS. To our knowledge, this is the only study to quantify ON deviation in HDT subjects. The discrepancies in ON deviation findings between acute HDT and long-duration spaceflight show that acute HDT does not truly simulate all aspects of microgravity.

A linear mixed-effects model was used to account for the potential impact of demographics and eye unilaterality on the observed structural changes. Age was not found to be a contributing factor to any of the observed changes; however, the range of ages in this study was small. Females showed much greater change in ONS area and vitreous chamber depth when compared to males, suggesting females may be more susceptible to the effects of CSF redistribution. While BMI was higher in males than females in this study, it was only associated with changes in ON area and ON deviation and was not associated with changes in ONS area. These observations are particularly interesting and merit further study, since idiopathic intracranial hypertension is much more common in females with high BMI. [31]

HDT studies have been used to simulate the fluid redistribution experienced in microgravity. [32] One such study invasively measured ICP in rhesus monkeys under 6° HDT and found that ICP was almost immediately elevated but then slowly reduced over the course of 15 minutes. [33] This is consistent with a human study where ICP was also found to return to supine levels during prolonged 6° HDT (Table 4-1). [34] The 30-minute HDT duration in the present study may have been sufficient to result in significant reduction in ICP before scans were taken, although the observed ONS distension suggests ICP was still elevated well beyond supine levels. Tilt angle is another parameter that can affect ICP with many studies showing increasing ICP with greater tilt angles. [35, 36] This gives confidence that the 15° tilt angle used in our study resulted in significant ICP elevation. In a study by

Marshall-Goebel et al., healthy subjects were placed in 3 different HDT positions (6°, 12°, and 18°) for 3.5 hours after which ICP and IOP was non-invasively measured. ICP was found to increase significantly during 18° HDT ($p < 0.001$), while IOP increased significantly during 12° ($p < 0.001$) and 18° ($p < 0.001$) HDT. [15] The increase in IOP indicates a propensity for IOP to counteract globe flattening at lower HDT angles after an adjustment period.

While HDT conditions have shown to simulate headward fluid redistribution experienced in microgravity, the magnitude of redistribution under HDT may be greater. The peripapillary total retinal thickness identified in healthy subjects after 30 days of strict 6° HDT increased to a greater degree than astronauts after a similar flight duration. [9] Furthermore, ONS distension was not identified after long-duration spaceflight when the methods used here were applied to astronauts. [21] The significant ONS distension we identified in HDT subjects potentially supports that HDT could result in a higher ICP than would be expected in microgravity.

The methods reported here involve several limitations. Manual selection of the ONH as a reference point for the purpose of locating the ON position 3 mm posterior to the ONH inherently introduces operator error. Similar error may be introduced in manual selection of the lens center and ON centerline path. However, we considered this error to be acceptable based on an assessment of inter and intra-operator reliability of these methods performed by Rohr et al., which found intraclass correlation coefficients of 0.67 and 0.68 for inter and intra-operator reliability, respectively. [21] Lee et al. provided some preliminary results and commentary on repeatability for a single subject using the methods applied here. [20] However, an upcoming longitudinal study with multiple healthy control subjects will test the repeatability of the method and natural anatomic variation over time. Flexion of the neck during HDT was not controlled, which may have unanticipated physiological effects and which may have affected the hydrostatic pressure calculations, in turn introducing systemic error into the study. Weaker correlation between the supine and HDT ON measurements compared to the ONS measurements suggest that the automated method is not as sensitive to detecting changes in the ON area. Finally, it was not possible to directly measure the exact magnitude of ICP elevation during HDT.

Quantitative MRI-based assessment of the ON and ONS before and during HDT could help our understanding of SANS and the potential role of ICP in the physiological response of ophthalmic structures. Here we report no change in ON area, but significant increases in ON deviation and ONS area as a result of HDT. These findings suggest that CSF pressure within the bulbar subarachnoid space was elevated during acute 15° HDT. Further research is warranted to quantitatively assess ON parameters in varying HDT durations and angles.

4.5 References

1. R.S. Johnston LFD. Biomedical Results from Skylab. Washington D.C.: National Aeronautics and Space Administration; 1977.
2. Hargens AR, Bhattacharya R, Schneider SM. Space physiology VI: exercise, artificial gravity, and countermeasure development for prolonged space flight. Eur J Appl Physiol. 2013;113(9):2183-92.
3. Tanaka K, Nishimura N, Kawai Y. Adaptation to microgravity, deconditioning, and countermeasures. J Physiol Sci. 2017;67(2):271-81.
4. Adrian LeBlanc CL, Linda Shackelford, Valentine Sinitsyn, Harlan Evans, Oleg Belichenko, Boris Schenkman, Inessa Kozlovskaya, Victor Oganov, Alexi Bakulin, Thomas Hedrick, and Daniel Feeback. Muscle volume, MRI relaxation times (T2), and body composition after spaceflight. Journal of Applied Pysiology. 200;86(6):6.
5. Lee AG, Mader TH, Gibson CR, Brunstetter TJ, Tarver WJ. Space flight-associated neuro-ocular syndrome (SANS). Eye (Lond). 2018;32(7):1164-7.
6. Mader TH, Gibson CR, Pass AF, Kramer LA, Lee AG, Fogarty J, et al. Optic disc edema, globe flattening, choroidal folds, and hyperopic shifts observed in astronauts after long-duration space flight. Ophthalmology. 2011;118(10):2058-69.
7. Kramer LA, Sargsyan AE, Hasan KM, Polk JD, Hamilton DR. Orbital and intracranial effects of microgravity: findings at 3-T MR imaging. Radiology. 2012;263(3):819-27.
8. Mader TH, Gibson CR, Otto CA, Sargsyan AE, Miller NR, Subramanian PS, et al. Persistent Asymmetric Optic Disc Swelling After Long-Duration Space Flight: Implications for Pathogenesis. J Neuroophthalmol. 2017;37(2):133-9.
9. Laurie SS, Lee SMC, Macias BR, Patel N, Stern C, Young M, et al. Optic Disc Edema and Choroidal Engorgement in Astronauts During Spaceflight and Individuals Exposed to Bed Rest. JAMA Ophthalmol. 2019.
10. Macias BR, Patel NB, Gibson CR, Samuels BC, Laurie SS, Otto C, et al. Association of Long-Duration Spaceflight With Anterior and Posterior Ocular Structure Changes in Astronauts and Their Recovery. JAMA Ophthalmol. 2020.
11. Lee AG, Mader TH, Gibson CR, Tarver W, Rabiei P, Riascos RF, et al. Spaceflight associated neuro-ocular syndrome (SANS) and the neuro-ophthalmologic effects of microgravity: a review and an update. NPJ Microgravity. 2020;6:7.
12. Zhang LF, Hargens AR. Spaceflight-Induced Intracranial Hypertension and Visual Impairment: Pathophysiology and Countermeasures. Physiol Rev. 2018;98(1):59-87.
13. Chen LM, Wang LJ, Hu Y, Jiang XH, Wang YZ, Xing YQ. Ultrasonic measurement of optic nerve sheath diameter: a non-invasive surrogate approach for dynamic, real-time evaluation of intracranial pressure. Br J Ophthalmol. 2019;103(4):437-41.
14. Johannesson G, Eklund A, Linden C. Intracranial and Intraocular Pressure at the Lamina Cribrosa: Gradient Effects. Curr Neurol Neurosci Rep. 2018;18(5):25.
15. Marshall-Goebel K, Mulder E, Bershad E, Laing C, Eklund A, Malm J, et al. Intracranial and Intraocular Pressure During Various Degrees of Head-Down Tilt. Aerosp Med Hum Perform. 2017;88(1):10-6.
16. Mader TH, Gibson CR, Miller NR, Subramanian PS, Patel NB, Lee AG. An overview of spaceflight-associated neuro-ocular syndrome (SANS). Neurol India. 2019;67(Supplement):S206-S11.
17. Watenpaugh DE. Analogs of microgravity: head-down tilt and water immersion. J Appl Physiol (1985). 2016;120(8):904-14.
18. Yasumasa A, Inoue S, Tatebayashi K, Shiraishi Y, Kawai Y. Effects of head-down tilt on cerebral blood flow in humans and rabbits. J Gravit Physiol. 2002;9(1):P89-90.
19. Eklund A, Johannesson G, Johansson E, Holmlund P, Qvarlander S, Ambarki K, et al. The pressure difference between eye and brain changes with posture. Ann Neurol. 2016;80(2):269-76.

20. Lee C, Rohr J, Sass A, Sater S, Zahid A, Macias B, et al. In vivo estimation of optic nerve sheath stiffness using noninvasive MRI measurements and finite element modeling. Journal of the Mechanical Behavior of Biomedical Materials. 2020;110.
21. Rohr JJ, Sater S, Sass AM, Marshall-Goebel K, Ploutz-Snyder RJ, Ethier CR, et al. Quantitative magnetic resonance image assessment of the optic nerve and surrounding sheath after spaceflight. NPJ Microgravity. 2020;6:30.
22. Helmke K, Hansen HC. Fundamentals of transorbital sonographic evaluation of optic nerve sheath expansion under intracranial hypertension. I. Experimental study. Pediatr Radiol. 1996;26(10):701-5.
23. Buck AH. A Reference Handbook of the Medical Sciences: Embracing the Entire Range of Scientific and Practical Medicine and Allied Science: W. Wood & Company; 1894.
24. Daboul A, Schwahn C, Schaffner G, Soehnel S, Samietz S, Aljaghsi A, et al. Reproducibility of Frankfort horizontal plane on 3D multi-planar reconstructed MR images. PLoS One. 2012;7(10):e48281.
25. Xiaobin Xie XZ, Jidi Fu , Huaizhou Wang , Jost B Jonas , Xiaoxia Peng , Guohong Tian ,Junfang Xian , Robert Ritch , Lei Li , Zefeng Kang , Shoukang Zhang , Diya Yang , Ningli Wang. Noninvasive intracranial pressure estimation by orbital subarachnoid space measurement Critical Care. 2013;17(4):12.
26. Wostyn P, De Deyn PP. Optic Nerve Sheath Distention as a Protective Mechanism Against the Visual Impairment and Intracranial Pressure Syndrome in Astronauts. Invest Ophthalmol Vis Sci. 2017;58(11):4601-2.
27. Wang X, Rumpel H, Lim WE, Baskaran M, Perera SA, Nongpiur ME, et al. Finite Element Analysis Predicts Large Optic Nerve Head Strains During Horizontal Eye Movements. Invest Ophthalmol Vis Sci. 2016;57(6):2452-62.
28. Raykin J, Forte TE, Wang R, Feola A, Samuels BC, Myers JG, et al. Characterization of the mechanical behavior of the optic nerve sheath and its role in spaceflight-induced ophthalmic changes. Biomech Model Mechanobiol. 2017;16(1):33-43.
29. Killer HE, Laeng HR, Flammer J, Groscurth P. Architecture of arachnoid trabeculae, pillars, and septa in the subarachnoid space of the human optic nerve: anatomy and clinical considerations. Br J Ophthalmol. 2003;87(6):777-81.
30. Wahlin A, Holmlund P, Fellows AM, Malm J, Buckey JC, Eklund A. Optic nerve length before and after spaceflight. Ophthalmology. 2020.
31. Durcan FJ, Corbett JJ, Wall M. The incidence of pseudotumor cerebri. Population studies in Iowa and Louisiana. Arch Neurol. 1988;45(8):875-7.
32. Lanny C. Keil KHM, Michael G. Skidmore, John Hines, Walter B. Severs. The effect of head-down tilt and water immersion on intracranial pressure in nonhuman primates. Aviation, Space, and Environmental Medicine. 1992;63(3):5.
33. Kiel LC MK, Skidmore MG, Hines J, Severs WB. The effect of head-down tilt and water immersion on intracranial pressure in nonhuman primates. Aviat Space Environ Med. 1992(63):181-5.
34. Lawley JS, Petersen LG, Howden EJ, Sarma S, Cornwell WK, Zhang R, et al. Effect of gravity and microgravity on intracranial pressure. J Physiol. 2017;595(6):2115-27.
35. Petersen LG, Petersen JC, Andresen M, Secher NH, Juhler M. Postural influence on intracranial and cerebral perfusion pressure in ambulatory neurosurgical patients. Am J Physiol Regul Integr Comp Physiol. 2016;310(1):R100-4.
36. Chapman PH, Cosman ER, Arnold MA. The relationship between ventricular fluid pressure and body position in normal subjects and subjects with shunts: a telemetric study. Neurosurgery. 1990;26(2):181-9.

Chapter 5: Quantification of Posterior Globe Flattening

** This is being reviewed for publication in the Journal of Applied Physiology under the title: MRI-based quantification of posterior optic globe flattening resulting from strict 6° head-down-tilt bedrest, and the effect of "treatment(s)"*

5.1 Introduction

Ophthalmic structural and functional changes in a condition known as Spaceflight-Associated Neuro-ocular Syndrome (SANS) have been observed in astronauts after long-duration spaceflight (> 6 months). [1-4] The proportion of astronauts who are diagnosed with SANS is about 40 percent but varies over time due to the ongoing characterization of its formal designation. [5] Ophthalmic abnormalities associated with SANS include choroidal folds, optic disc edema, hyperopic shift, posterior globe flattening (Figure 3-3), and reduced visual acuity. [5] In some subjects, these changes have been shown to persist long after return to Earth. [6, 7] Headward fluid shifts that occur in the absence of a hydrostatic pressure gradient in weightlessness are thought to be a primary contributor of SANS, leading to mild but chronic elevation in intracranial pressure (ICP). [8] Increases in ICP may result in a reversal of the trans-laminar pressure gradient (TLPG), wherein ICP becomes greater than intraocular pressure (IOP), contributing to scleral flattening. [9, 10]

5.1.1 Spaceflight Analogs

Other well-known spaceflight-associated conditions, such as bone and muscle atrophy, have well defined etiologies and mitigation techniques. However, one of the challenges of developing mitigation techniques for SANS is the difficulty in studying its pathophysiology due to the prohibitive costs and physical limitations of inflight monitoring. Spaceflight analogs have been proposed to simulate the effects of microgravity on Earth. Currently, head-down tilt (HDT) studies are used as a spaceflight analog because HDT simulates fluid redistributions that are suspected to occur in microgravity. [11] However, the presence of a constant gravitational vector during HDT may elicit different physiological responses compared to spaceflight.

5.1.2 HDT Studies

Past HDT studies have tested HDT angles ranging from 4° to 15+°, but 6° is by far the most common and produces approximately -0.1 G_z. [12] Duration of bed rest in these studies varies as does the amount of movement allowed. A subjective assessment of ground-based spaceflight analogs found that HDT showed good fidelity in simulating the effects of microgravity for fluid redistribution but not for neurologic and pulmonary function. [13] HDT studies have been shown to overestimate fluid redistributions compared to microgravity. One study found 45% of participants in a strict 6° HDT for

30 days developed optic disc edema (ODE), compared to 15% found in astronauts. [14] This suggests that ophthalmic changes may be more sensitive to HDT duration than spaceflight duration, allowing for shorter study durations.

5.1.3 Mitigation Techniques

The majority of spaceflight-associated conditions are attributed to the lack of a gravitational force in space. This has led researchers to test if replacing gravitational forces with centrifugal forces could mitigate the negative effects of weightlessness. [15] In short-term HDT studies, short-arm centrifugation was an effective countermeasure for musculoskeletal deconditioning [16] and orthostatic tolerance [17] in bed rest subjects. Both studies noted that intermittent centrifugation was more effective than continuous centrifugation in reducing the effects of HDT, and daily centrifugation is well tolerated by participants. [18] However, the effectiveness of centrifugation in mitigating the neuro-ocular effects of HDT and spaceflight has yet to be determined.

5.1.4 Study Aim

The aim of this study was to quantify volume displacement of the posterior ocular globe during and after 60-day HDT bed rest, and to assess the effectiveness of continuous and intermittent centrifugation as mitigation techniques (Figure 5-1). To accomplish this, an automated MRI-based method was applied to segment the optic globe and compare follow-up posterior globe shapes to baseline, pre-bedrest globe shape.

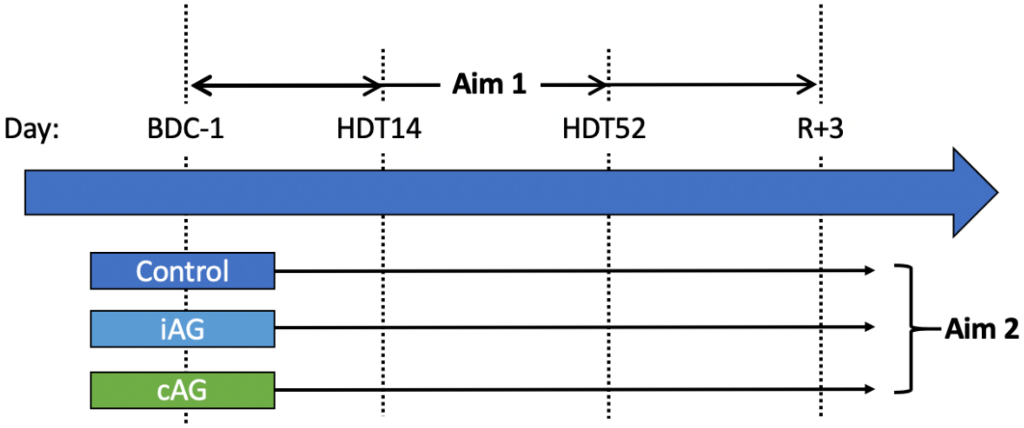

Figure 5-1. Schematic of Study Design and Aims. Subjects were split into three study groups that participated in 60 days of strict HDT. Aim 1: posterior globe volume displacement at 14 and 52 days into HDT and 3 days after HDT compared to baseline. Aim 2: differences between the control and artificial gravity groups.

5.2 Materials and Methods

In this randomized controlled study, subjects participated in a 60-day strict 6° HDT bed rest at the envihab facility of the German Aerospace Center (DLR) in Cologne, Germany. MRI scans were collected at four timepoints throughout the study. Baseline scans were collected one day before bedrest (BDC-1), scans during bedrest were collected at 14 (HDT14) and 52 (HDT52) days, and follow-up scans were collected 3 days after bedrest (R+3).

5.2.1 Participants

Written informed consent was obtained from all participants and was approved by the ethics committee of the Northern Rhine Medical Association (Ärztekammer Nordrhein, application #2018143) in Duesseldorf, Germany, as well as the Federal Office for Radiation Protection (Bundesamt für Strahlenschutz). 16 males and 8 females successfully completed the study, but two female subjects were omitted from the final data due to MRI artifacts. Subjects were randomly assigned to one of the following groups: the intermittent artificial gravity group (iAG, n = 7, 2 females, body mass index (BMI) 23.42 ± 1.57, age 35 ± 11 years), the continuous artificial gravity group (cAG, n = 8, 3 females, BMI 24.00 ± 1.71, age 32 ± 10 years), and the control group (ctrl, n =7, 1 female, BMI 25.39 ± 2.71, age 33 ±7 years) (Table 5-1).

Table 5-1. Demographics of Study Subjects by Groups. Table showing number of subjects, sex, BMI, and age for the continuous and intermittent centrifugation groups, and the control.

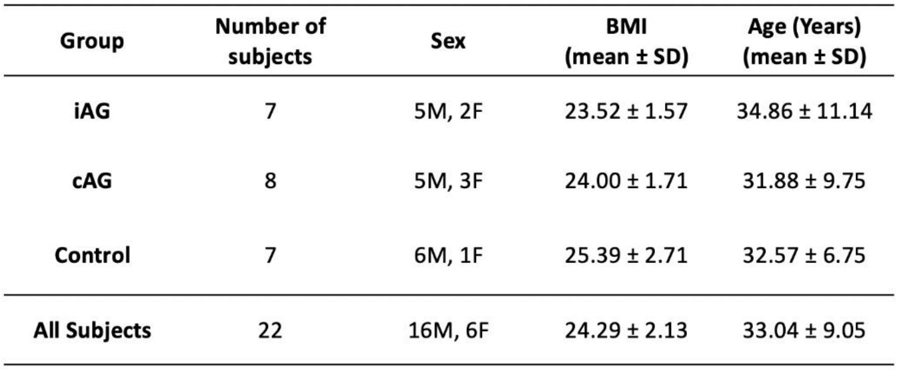

Group	Number of subjects	Sex	BMI (mean ± SD)	Age (Years) (mean ± SD)
iAG	7	5M, 2F	23.52 ± 1.57	34.86 ± 11.14
cAG	8	5M, 3F	24.00 ± 1.71	31.88 ± 9.75
Control	7	6M, 1F	25.39 ± 2.71	32.57 ± 6.75
All Subjects	22	16M, 6F	24.29 ± 2.13	33.04 ± 9.05

5.2.2 HDT Bedrest

Participants remained in a tightly controlled environment for a total of 89 days, including 29 days of acclimation and recovery, and the remaining 60 days spent in beds with the head tilted 6° below horizontal. During the 60 days of HDT, participants were required to keep one shoulder on the bed at all times and the use of pillows was not permitted to avoid confounding of results. [8] All daily activities including eating and hygiene were performed in the HDT position. Diet was strictly controlled throughout the study with a daily energy intake of 1.3 times the resting metabolic rate and daily water intake of 50 mL/kg body mass. Twenty-four-hour monitoring by trained staff ensured compliance with all protocols.

5.2.3 Artificial Gravity

Participants in the artificial gravity (AG) groups completed daily sessions of centrifugation during the bed rest portion of the study. Gravity was simulated in the DLR short-arm centrifuge (Figure 5-2) which has a radius of 3.8 m and spun at a subject-specific rotational speed to achieve an acceleration of 1 g at the center of mass and 2 g at the feet and rotational direction alternated daily.

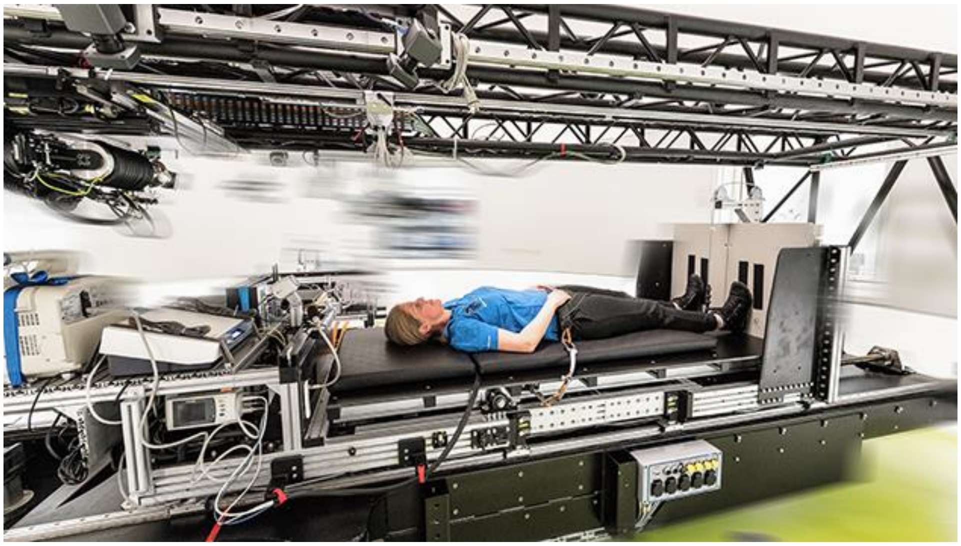

Figure 5-2. Short Arm Human Centrifuge. The centrifuge has a radius of 3.8 m and spun at a subject specific rotational speed to generate an acceleration of 1 g at the center of mass and 2 g at the feet.

The cAG group completed continuous 30-minute sessions while the iAG group completed six, five-minute bouts of centrifugation with three-minute breaks in between. Centrifugation occurred in the supine position (0° HDT) but subjects were positioned in 6° HDT immediately before and after each centrifuge run. Participants were instructed to gaze at a fixed point while on the centrifuge to avoid head movements. All AG sessions were carried out under the supervision of a medical doctor.

5.2.4 MRI Acquisition and Reformatting

T2-weighted axial spin-echo fat-suppressed MRI sequences were collected using a 3T system (Verio 3T; vB19; Siemens Healthineers, Erlangen, Germany) with 0.78 mm in plane isotropic pixel size (FOV 100 x 100), and 0.78 mm slice thickness and spacing. Additional sequence parameters included a 170° flip angle, 750 ms repetition time, 112 ms echo time, and 123.22 Hz/pixel bandwidth.

5.2.5 Point Cloud Generation and Alignment

Each globe underwent an automated multistep 3D reconstruction and displacement mapping process in MATLAB (vers 2019a, Mathworks Corp. Natick, MA.) previously described by Sater et al. In brief, each globe was radial resliced about a central rotational axis at one-degree increments in Osirix MD (version 8.0.1, Pixmeo, Geneva, Switzerland) (Figure 5-3A). Segmentation of each slice was completed using an offset global thresholding to create a contour, which were transformed into 3D coordinates to create a point cloud of the globe. A box grid filter was applied (MATLAB computer vision toolbox, pcdownsample) to ensure uniform point distribution. An iterative closest point registration algorithm with 60 iterations (MATLAB computer vision toolbox, pcregistericp) was applied to align follow up point clouds to their respective baseline (BDC-1) point clouds (Figure 5-3B). The spherical coordinates of each point on the posterior hemisphere of the globe surface were expressed in a 2D polar coordinate distance map. Circumferential and meridional angles of each point were transformed into polar angles and radial locations, respectively, and the distance between the points and the baseline point cloud's centroid was represented by a color on the distance maps. The baseline distance map was subtracted from the follow up distance map to generate a paired displacement map (Figure 5-3C). Volume displacement was calculated for the region of the distance map within 4 mm of the optic nerve head (Figure 5-3D).

5.2.4 Statistics

A linear mixed-effects model that accounts for repeated measurements from the same individual was developed:

$$y_i = \beta_0 + \beta_1 x_{1i} + \beta_2 x_{2i} + \beta_3 x_{3i} + \beta_4 x_{4i} + \beta_5 x_{5i} + \beta_6 x_{6i} + z_{0i} + z_{1i} x_{2i} + z_{2i} x_{3i} + z_{3i} x_{4i} + \epsilon_i$$

where y_i is the measurement of a parameter of interest, β_0 is the baseline (left eye of a male subject at BDC-1 and in the ctrl group), x_{1i} is the treatment group, x_{2i} is the timepoint, x_{3i} denotes the right eye, x_{4i}, x_{5i}, and x_{6i} are the age, sex, and BMI of the ith subject, respectively. While coefficient β represents fixed effect sizes, coefficient z represents the random effects and follows a multivariate normal distribution with mean of 0 and a symmetric variance-covariance matrix:

$$\begin{pmatrix} z_{0i} \\ z_{1i} \end{pmatrix} \sim N\left(\begin{pmatrix} 0 \\ 0 \end{pmatrix}, \begin{pmatrix} \sigma_0^2 & \sigma_{01} \\ \sigma_{01} & \sigma_1^2 \end{pmatrix}\right).$$

The "*fitlme*" function in MATLAB (Ver. R2019a Mathworks Corp., Natick, MA) was used to estimate the coefficients and variances in this linear mixed-effects model and test the hypotheses. This model appoints treatment group, timepoint, eye, age, BMI, and sex as fixed effects, with the corresponding coefficient indicating the effect size. We could further test whether the true effect size is significantly different from zero. If so, it means that there is a statistically significant difference on the parameter between the three treatment groups or between the two eyes, or that there is a statistically significant impact of age, BMIs, or sex on the parameter of interest. This model treats the subjects as random with repeated measurements which allows us to account for the variability across subjects and dependence between groups, timepoints, and eyes, for each subject.

Using this linear mixed-effects model, we calculated p-values for globe volume displacement. Some of these p-values were dependent due to dependence among several parameters of interest. We ignored such dependence and accounted for multiple comparison with Bonferroni correction, in order to derive more conservative results. To apply Bonferroni correction, we adjusted the threshold for p-values to be α/m, where α is the experimentwise type I error rate and m is the number of p values under consideration. With six parameters and five fixed-effect sizes per parameter, we have $m =?$, and we consider an $\alpha = 0.10$.

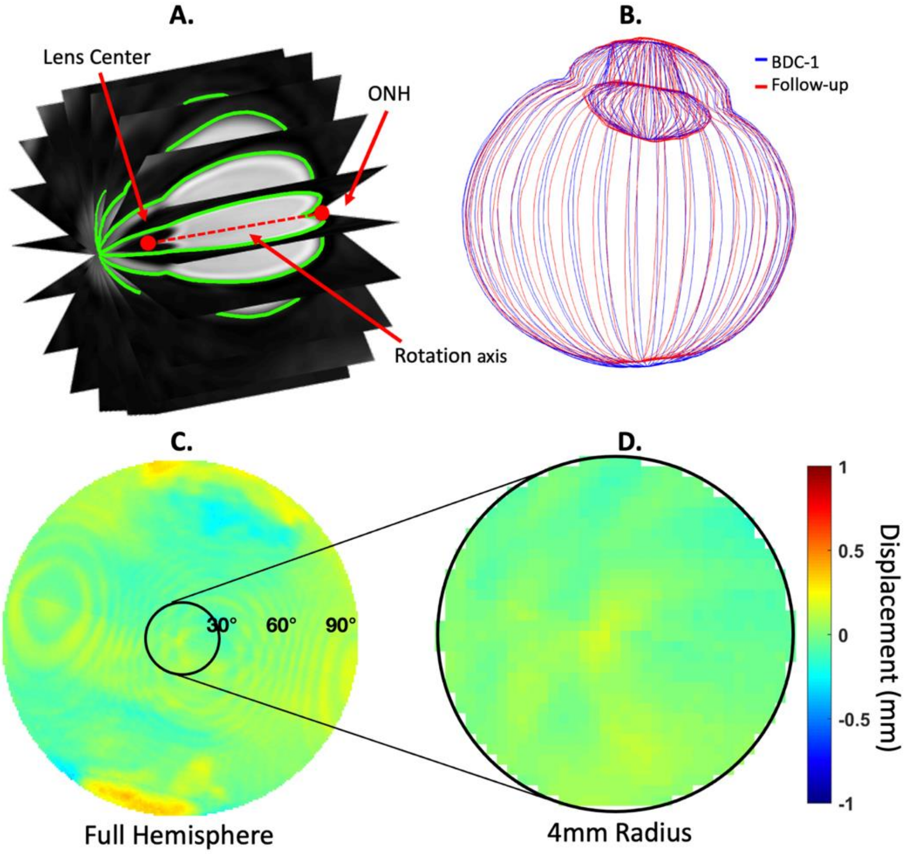

Figure 5-3. Segmentation Methods for T2-weighted Axial Ocular MRI. (A) Images were radially resliced and segmented. (B) Baseline and follow-up point clouds were aligned using closest iterative point registration. (C) Displacement maps of the posterior globe were generated for each baseline and follow up pair. (D) Posterior optic globe displacement was quantified for a region 4 mm radius of the ONH.

5.3 Results

5.3.1 Posterior Glove Displacement by Duration

HDT duration results are summarized in Table 5-2. On average, posterior globe volume displacement increased with HDT duration, and did not recover within three days post-HDT for all three study groups (Figure 5-4). For the iAG group, average volume displacement was 2.44 mm^3 (95% CI -1.80 mm^3 to 6.84 mm^3, $p = 0.252$) at HDT14, 4.74 mm^3 (95% CI -0.59 mm^3 to 10.07 mm^3, $p = 0.080$) at HDT52, and 5.47 mm^3 (95% CI -0.12 mm^3 to 11.06 mm^3, $p = 0.055$) at R+3 when compared to BDC-1 (baseline). For the cAG group, average displacement was 0.85 mm^3 (95% CI -2.59 mm^3 to 4.29 mm^3, $p = 0.620$) at HDT14, 5.05 mm^3 (95% CI 0.03 mm^3 to 10.07 mm^3, $p = 0.049$) at HDT52, and 4.23 mm^3 (95% CI 1.25 mm^3 to 7.22 mm^3, $p = 0.006$) at R+3 when compared to BDC-1. For the control group, average displacement was 1.00 mm^3 (95% CI -1.47 mm^3 to 3.47 mm^3, $p = 0.42$) at HDT14, 3.50 mm^3 (95% CI 0.76 mm^3 to 6.25 mm^3, $p = 0.013$) at HDT52, and 6.86 mm^3 (95% CI 2.96 mm^3 to 10.75 mm^3, $p = 0.001$) at R+3 when compared to BDC-1.

Table 5-2. Volume Displacement by Group at Each Timepoint. Table showing the mean and standard error (SE) of posterior globe volume displacement at HDT day 14 (HDT14), HDT day 52 (HDT52) and at three days post-HDT (R+30) for the iAG, cAG and control study groups. Note: $p<0.05$ *, $p<0.01$ **, $p<0.005$ ***

Group	HDT14 (mean ± SE, mm^3)	HDT52 (mean ± SE, mm^3)	R+3 (mean ± SE, mm^3)
iAG	2.44 ± 2.10	4.74 ± 2.64	5.47 ± 2.77
cAG	0.85 ± 1.71	5.05 ± 2.50 *	4.23 ± 4.49 **
Control	1.00 ± 1.22	3.51 ± 1.36 *	6.86 ± 1.93 ***

note: $p < 0.05$, $p < 0.01$**, $p < 0.001$****

5.3.2 Effect of Artificial Gravity on Posterior Globe Volume Displacement

On average, AG groups had less volume displacement than the control group, but these differences were insignificant. The volume displacement for the iAG group on average was 0.17 mm^3 ($p = 0.942$) less than the control group and the displacement for the cAG group on average was 1.11 mm^3 ($p = 0.633$) less than the control group (Figure 5-4A).

5.3.3 Demographic Effects and Unilaterality

Demographics and differences between eyes were assessed to see if any of the changes were associated with demographic effects or unilaterality. Age was associated with an increase in volume displacement of 0.21 mm^3 (95% CI 0.10 mm^3 to 0.32 mm^3, *p* = 0.0001). On average, females had 8.21 mm^3 more volume displacement than males (95% CI 5.82 mm^3 to 10.59 mm^3, *p* = 5.24e-10) (Figure 5-4B). All other demographic effects were insignificant and significant differences between eyes were not observed.

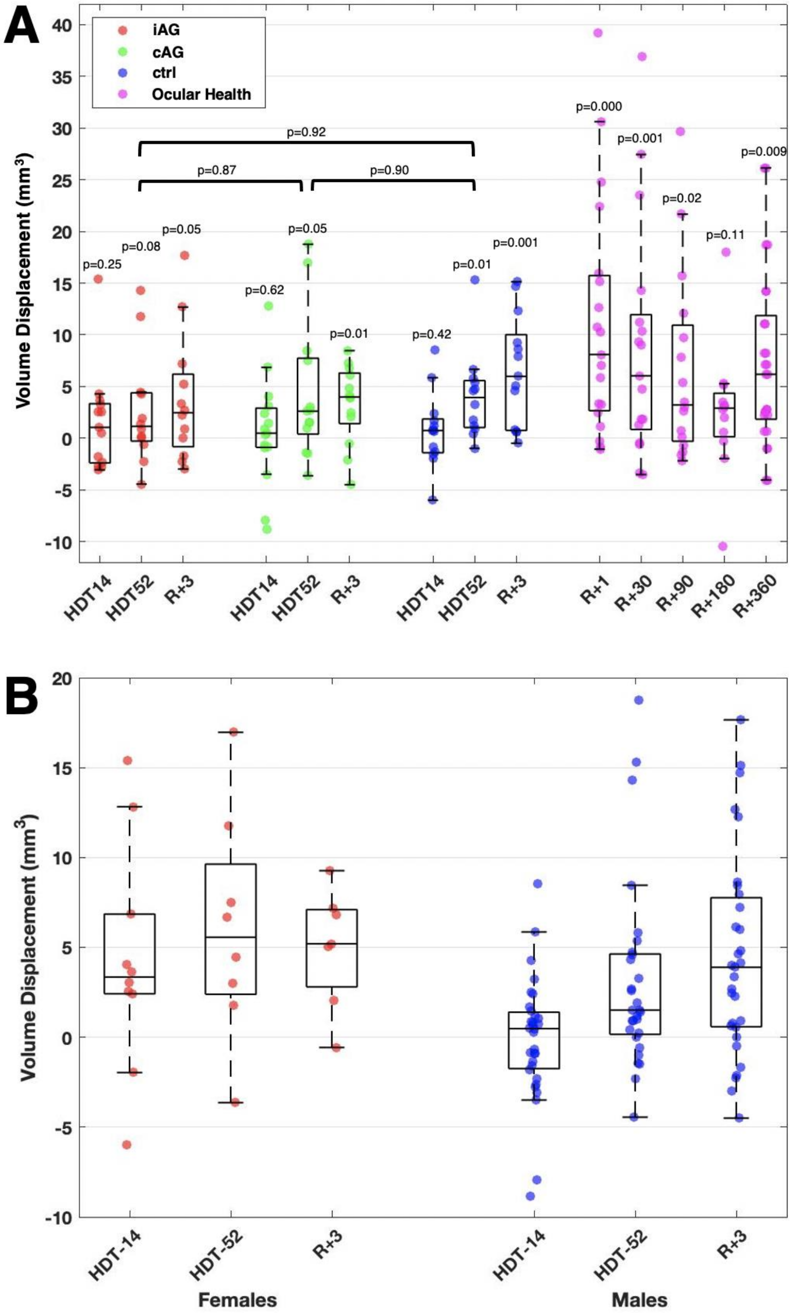

Figure 5-4. (A) Plot showing volume displacement for the iAG (red), cAG (green) and control groups (blue) at HDT14, HDT52, and R+3 with statistical significance shown. (B) Plot showing the distribution volume displacement for males (blue) and females (red) at all three timepoints. All displacements are referenced pre-HDT baseline geometries.

5.4 Discussion

Non-invasive automated techniques were applied to MR images of HDT bed rest participants to quantify posterior optic globe volume displacement over time and assess the effectiveness of centrifugation as a mitigation technique. Small, inward displacements of the peripapillary choroidal-scleral interface were found to increase with HDT duration, with no recovery within three days post-HDT. Neither continuous nor intermittent centrifugation were significantly effective in reducing these displacements when compared to a control group. Women were found to have greater posterior globe volume displacement when compared to men and older age was also associated with increased displacement.

5.4.1 Physiological Interpretation

The segmentation methods used in this study segmented the optic globe near the choroidal-scleral interface, and thus the displacements measured are likely due to a combination of scleral flattening, choroidal swelling, and retinal thickening. A previous study found that after 30 days of strict 6° HDT, total retinal thickness had increased by 53.9 μm and choroidal thickness remained unchanged. [14] This suggests that the volume displacements measured here are partially attributed to scleral flattening because they exceed that which could be explained by thickening of the retinal tissue alone.

Scleral flattening is likely caused by a multitude of factors, but a reversal of the TLPG is suspected to play a role. Invasive measurements of ICP in rhesus monkeys during 6° HDT found that ICP immediately increased but slowly recovered to near supine levels over the course of 30 minutes. [19] Even if 6° HDT results in supine-level ICP, this pressure is still elevated beyond what has been measured in the seated or standing positions. [8] Chiquet et al. measured intraocular pressure (IOP) over seven days of 6° HDT and found that after an initial increase, IOP decreased by 0.96 mmHg after five days and 1.56 mmHg after seven days. [20] If ICP is chronically elevated to supine levels, and IOP is reduced, a persistent reversal of the TLPG could be causing the scleral flattening observed in the present study.

5.4.2 Comparison to Astronauts

Significant globe volume displacement has been identified in astronauts using identical methods to those described here. This lends support to the use of strict, long-term HDT bed rest studies as a ground-based analog. Average volume displacement in the astronaut cohort was 9.88 mm^3 approximately 4 days after returning from long-duration spaceflight (167 ± 17 days), far exceeding the displacements reported here. The most probable explanation for the difference is the extended duration of spaceflight, but the presence of choroidal engorgement in astronauts likely played a contributing role.

5.4.3 Duration Interpretation

Posterior globe volume displacement tended to increase with HDT duration. At HDT14, none of the study groups showed statistically significant displacement, which suggests that the sclera is somewhat resistant to perineural forces caused by changes in the TLPG. However, by R+3, volume displacement increased significantly, suggesting that long-term alterations in the TLPG can result in remodeling of scleral tissue. This may explain why globe flattening in astronauts is not resolved within a year after returning from space.

5.4.4 Recovery Interpretation

For most subjects, volume displacement increased between HDT52 and R+3. This timeframe included eight additional days of HDT and three days of acclimation and recovery. It is likely that displacement continued to increase during the additional eight days of bed rest, but it is expected these increases would be small relative to the previous 52 days. The increase in displacement observed between the last two time-points suggests that little recovery occurred in the three days of acclimation. Laurie et al. reported an average decrease of 12.7 μm in peripapillary total retinal thickness six days after a 30-day HDT study. [14] Displacements of this magnitude would be nearly undetectable by the methods described here. If recovery is insignificant within the first few days of acclimation, astronauts' posterior globes may be largely unchanged in days following return to Earth.

5.4.5 Artificial Gravity Interpretation

Although differences between the AG groups and the control group were not statistically significant, the AG groups did have lower average volume displacements by R+3 when compared to the control group. If globe flattening is caused by mild but chronically elevated ICP, daily 30-minute centrifugation sessions may not be sufficient to significantly reduce globe flattening. The typical adult will spend at least 16 hours per day in the upright position, during which time ICP is well below supine levels. [8] A 30-minute duration is only 3.1% of the time a typical adult spends in the upright position.

5.4.6 Demographics Interpretation

Sex was shown to be a contributing factor in posterior globe volume displacement. On average, females had significantly greater volume displacement at all three timepoints when compared to males (Figure 5-4B). However, no female astronauts have been diagnosed with Frisèn grade edema, and Laurie et al. did not identify a difference between sexes in retinal thickening during

30-day HDT bed rest. [14] One study non-invasively estimated optic nerve sheath (ONS) stiffness using HDT and found the ONS stiffness to be significantly greater in males. [21] If the ONS acts as a compensatory mechanism for ICP fluctuations, [22] then a higher degree of displacement would be expected from subjects with stiffer ONSs. Females were highly underrepresented in this study, warranting further investigation into the effect of sex in the development of SANS symptoms.

5.4.7 Limitations

There are several limitations that remain unaddressed in this study. The most significant limitation is the lack of known reliability and repeatability of the methods applied, but previous applications of this method showed good agreement with ocular biometry measurements. Another limitation is the low number of subjects in the study, particularly women. Finally, the duration of centrifugation was a small fraction of the typical time spent by an adult in a lowered ICP state.

5.5 References

1. Marshall-Goebel K, Terlevic R, Gerlach DA, Kuehn S, Mulder E, Rittweger J. Lower body negative pressure reduces optic nerve sheath diameter during head-down tilt. J Appl Physiol (1985). 2017;123(5):1139-44. Epub 2017/08/19.
2. Mader TH, Gibson CR, Pass AF, Lee AG, Killer HE, Hansen HC, et al. Optic disc edema in an astronaut after repeat long-duration space flight. J Neuroophthalmol. 2013;33(3):249-55. Epub 2013/07/16.
3. Lee AG, Mader TH, Gibson CR, Brunstetter TJ, Tarver WJ. Space flight-associated neuro-ocular syndrome (SANS). Eye (Lond). 2018;32(7):1164-7. Epub 2018/03/13.
4. Mader TH, Gibson CR, Pass AF, Kramer LA, Lee AG, Fogarty J, et al. Optic disc edema, globe flattening, choroidal folds, and hyperopic shifts observed in astronauts after long-duration space flight. Ophthalmology. 2011;118(10):2058-69. Epub 2011/08/19.
5. Lee AG, Mader TH, Gibson CR, Tarver W, Rabiei P, Riascos RF, et al. Spaceflight associated neuro-ocular syndrome (SANS) and the neuro-ophthalmologic effects of microgravity: a review and an update. NPJ Microgravity. 2020;6:7. Epub 2020/02/13.
6. Macias BR, Patel NB, Gibson CR, Samuels BC, Laurie SS, Otto C, et al. Association of Long-Duration Spaceflight With Anterior and Posterior Ocular Structure Changes in Astronauts and Their Recovery. JAMA Ophthalmol. 2020. Epub 2020/04/03.
7. Mader TH, Gibson CR, Barratt MR, Miller NR, Subramanian PS, Killer HE, et al. Persistent Globe Flattening in Astronauts following Long-Duration Spaceflight. Neuro-Ophthalmology. 2020:1-7.
8. Lawley JS, Petersen LG, Howden EJ, Sarma S, Cornwell WK, Zhang R, et al. Effect of gravity and microgravity on intracranial pressure. J Physiol. 2017;595(6):2115-27. Epub 2017/01/17.
9. Marshall-Goebel K, Mulder E, Bershad E, Laing C, Eklund A, Malm J, et al. Intracranial and Intraocular Pressure During Various Degrees of Head-Down Tilt. Aerosp Med Hum Perform. 2017;88(1):10-6. Epub 2017/01/08.
10. Johannesson G, Eklund A, Linden C. Intracranial and Intraocular Pressure at the Lamina Cribrosa: Gradient Effects. Curr Neurol Neurosci Rep. 2018;18(5):25. Epub 2018/04/14.
11. Watenpaugh DE. Analogs of microgravity: head-down tilt and water immersion. J Appl Physiol (1985). 2016;120(8):904-14. Epub 2016/02/13.
12. Nelson ES, Myers JG, Jr., Lewandowski BE, Ethier CR, Samuels BC. Acute effects of posture on intraocular pressure. PLoS One. 2020;15(2):e0226915. Epub 2020/02/07.

13. Schneider SM, Lee SM, Feiveson AH, Watenpaugh DE, Macias BR, Hargens AR. Treadmill exercise within lower body negative pressure protects leg lean tissue mass and extensor strength and endurance during bed rest. Physiol Rep. 2016;4(15).
14. Laurie SS, Macias BR, Dunn JT, Young M, Stern C, Lee SMC, et al. Optic Disc Edema after 30 Days of Strict Head-down Tilt Bed Rest. Ophthalmology. 2019;126(3):467-8. Epub 2018/10/12.
15. Bukley A. PW, Clément G. . Physics of Artificial Gravity. Artificial Gravity The Space Technology Library. 2007;20.
16. Rittweger J, Bareille MP, Clement G, Linnarsson D, Paloski WH, Wuyts F, et al. Short-arm centrifugation as a partially effective musculoskeletal countermeasure during 5-day head-down tilt bed rest--results from the BRAG1 study. Eur J Appl Physiol. 2015;115(6):1233-44. Epub 2015/02/11.
17. Linnarsson D, Hughson RL, Fraser KS, Clement G, Karlsson LL, Mulder E, et al. Effects of an artificial gravity countermeasure on orthostatic tolerance, blood volumes and aerobic power after short-term bed rest (BR-AG1). J Appl Physiol (1985). 2015;118(1):29-35. Epub 2014/10/25.
18. Frett T, Green DA, Mulder E, Noppe A, Arz M, Pustowalow W, et al. Tolerability of daily intermittent or continuous short-arm centrifugation during 60-day 6o head down bed rest (AGBRESA study). PLoS One. 2020;15(9):e0239228. Epub 2020/09/19.
19. Keil LC, McKeever KH, Skidmore MG, Hines J, Severs WB. The effect of head-down tilt and water immersion on intracranial pressure in nonhuman primates. Aviat Space Environ Med. 1992;63(3):181-5. Epub 1992/03/01.
20. Chiquet C, Custaud MA, Le Traon AP, Millet C, Gharib C, Denis P. Changes in intraocular pressure during prolonged (7-day) head-down tilt bedrest. J Glaucoma. 2003;12(3):204-8. Epub 2003/06/05.
21. Lee C, Rohr J, Sass A, Sater S, Zahid A, Macias B, et al. In vivo estimation of optic nerve sheath stiffness using noninvasive MRI measurements and finite element modeling. J Mech Behav Biomed Mater. 2020;110:103924. Epub 2020/09/23.
22. Wostyn P, Mader TH, Gibson CR, Killer HE. The escape of retrobulbar cerebrospinal fluid in the astronaut's eye: mission impossible? Eye (Lond). 2019. Epub 2019/05/09.

Chapter 6: Conclusions and Future Work

The objective of this thesis was to quantify intrathecal solute transport and ophthalmic changes in long duration spaceflight astronauts using novel bioimaging techniques. In the pharmacokinetic quantification of solute transport investigation described in Chapter 2, we addressed several intrathecal drug delivery injection parameters within a completed cerebrospinal fluid system of a 3D subject specific human model. Within this model, we tested bolus volume and rate, flush volume, timing, and rate, injection location, and type of device. It was observed that flush volume had the greatest impact on increasing solute transport to the brain and all remaining parameters had a similar impact. This is critical as relatively little drug was delivered to the brain across all protocols conducted in the study. Indeed, there is a need for future studies to investigate the impact of the combination of injection parameters and validate the results of this study in vivo.

High resolution magnetic resonance imaging (MRI) sequences were collected from healthy volunteers during head down tilt in Chapter 4 to quantify changes in optic nerve sheath cross sectional area, optic nerve (ON) cross sectional area and deviation, vitreous chamber depth, and Young’s modulus. Furthermore, demographic effects were also investigated. It was observed that the ON sheath cross sectional area and the ON deviation increased, the vitreous chamber depth decreased, and the ON cross sectional area remained unchanged. These findings indicate that CSF pressure in the bulbar subarachnoid space was elevated under HDT. Furthermore, a significant effect of sex and body mass index was also observed. Future work is needed to confirm the results of this study by the development of an automated physiological selection method and measurement of the intracranial pressure during HDT. Additionally, differing HDT durations and angles should also be used to quantify ON parameters and therefore contribute a greater understanding to the pathology of spaceflight associated neuro-ocular syndrome (SANS).

Similarly, Chapter 5 studied ophthalmic changes in healthy volunteers under acute head down tilt (HDT) and investigated the effect of treatments. Of which, there were three: 1) continuous centrifugation, 2) intermittent centrifugation, and 3) control. MRI was used to acquire the scans before, during, and after HDT. On average, it was observed that all three groups displayed an increase in posterior globe flattening with an increase in HDT duration and there was no significant difference in reduction of posterior globe flattening observed between treatment groups. Sex was also found to have an effect on posterior globe flattening. These findings also suggested that strict HDT bed rest does provide a reasonable analog to microgravity and that mitigation techniques may not reduce posterior globe flattening. Future work is needed to investigate the effect of longer centrifugation as a countermeasure in addition to the effect of sex on posterior globe flattening

Appendix A: Supplementary Figures

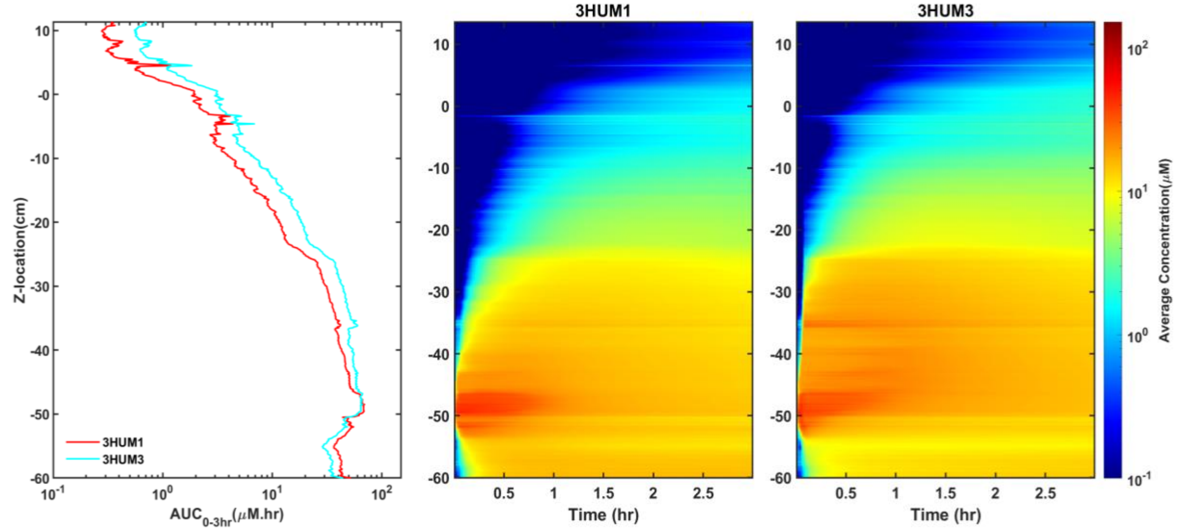

Supplementary Figure 1. Effect of flush volume by average AUC and spatial temporal distribution comparison. There is a significant difference observed between the AUC trends, as the protocol with the higher flush volume, 3HUM3, delivered more to the brain than equivalent protocol with the lower flush volume. This can also be observed in the spatial temporal trends. Immediately after injection, 3HUM3 had a steeper slope of solute distribution, thereby pushing more of the solute cranially and reaching a location of approximately -15 cm. The solute distribution did not reach the same location, -15 cm, until approximately 30 minutes after the injection.

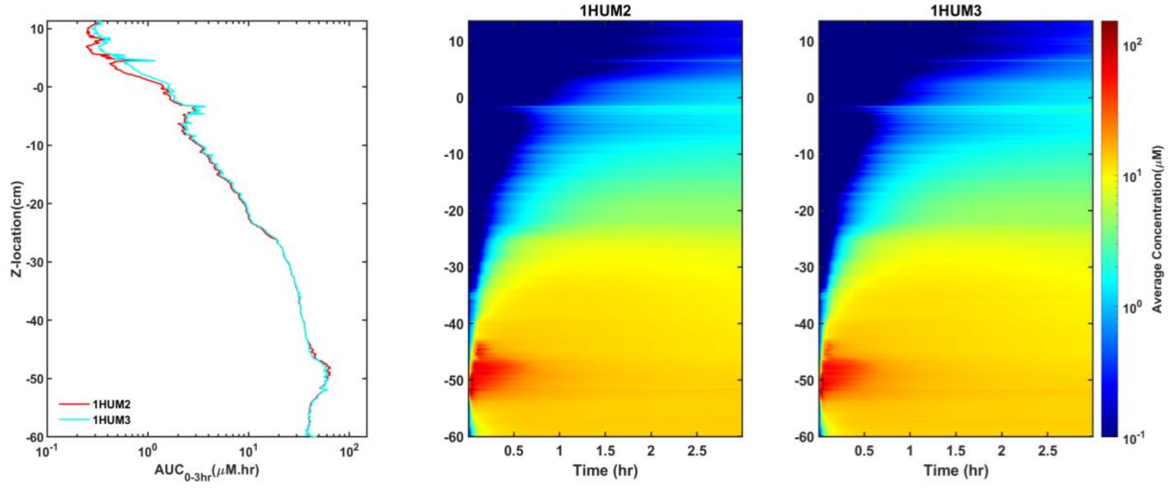

Supplementary Figure 2. Effect of flush rate by average AUC and spatial temporal distribution comparison. There is no significant difference between the AUC trends and the spatial temporal distribution plots; however, it can be observed that within the brain region (0 to 10 cm) on the AUC plot, the case with the higher flush rate, 1HUM3, delivered slightly more solute to the brain.

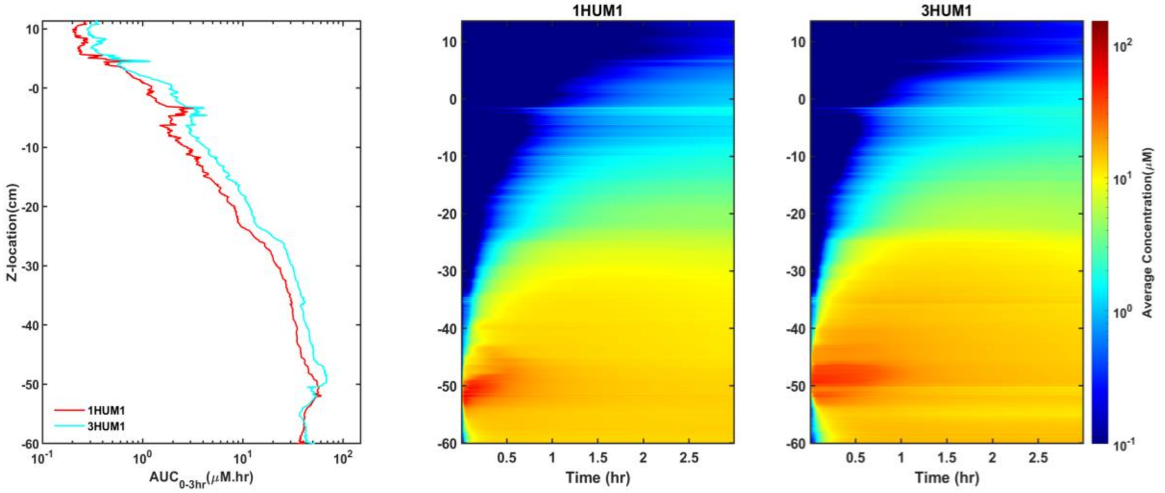

Supplementary Figure 3. Effect of device by average AUC and spatial temporal distribution comparison. There is a noticeable difference between the plots. Within the AUC trends, a significant difference can be observed in the spinal region (0 to -60 cm), however, the differences decrease in the brain region (0 to 10 cm). The spatial temporal distribution also indicates a difference in spread near the spinal region and similar distribution near the brain region.

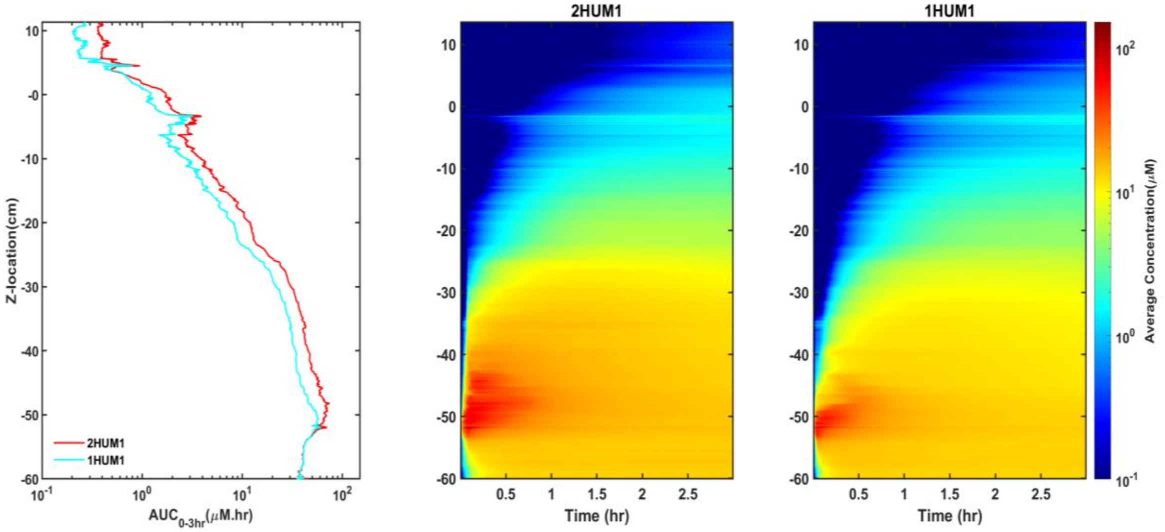

Supplementary Figure 4. Effect of bolus injection volume by average AUC and spatial temporal distribution comparison. Similar to Supplementary Figure 1, significant differences can be observed across both the AUC trends and the spatial temporal distribution. The AUC trends indicate a significant difference across all regions, with the case containing the higher bolus injection volume delivering more solute cranially towards the brain. Also, similar to Supplementary Figure 1, the case with the large bolus injection volume displays a more rapid distribution of solute immediately after injection, with the smaller bolus injection volume producing a slower distribution rate.

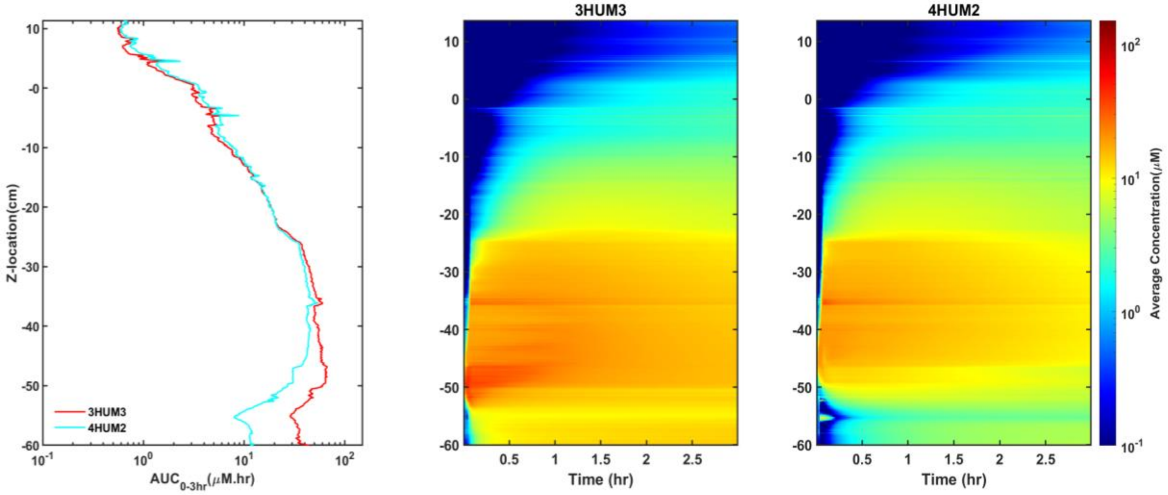

Supplementary Figure 5. Effect of injection location by average AUC and spatial temporal distribution comparison. The case with the higher injection location, 4HUM2, displayed less solute transport within the lumbar region (-50 to -60 cm), which agrees with the higher injection location, and is also observed in the 4HUM2 spatial temporal distribution plot.

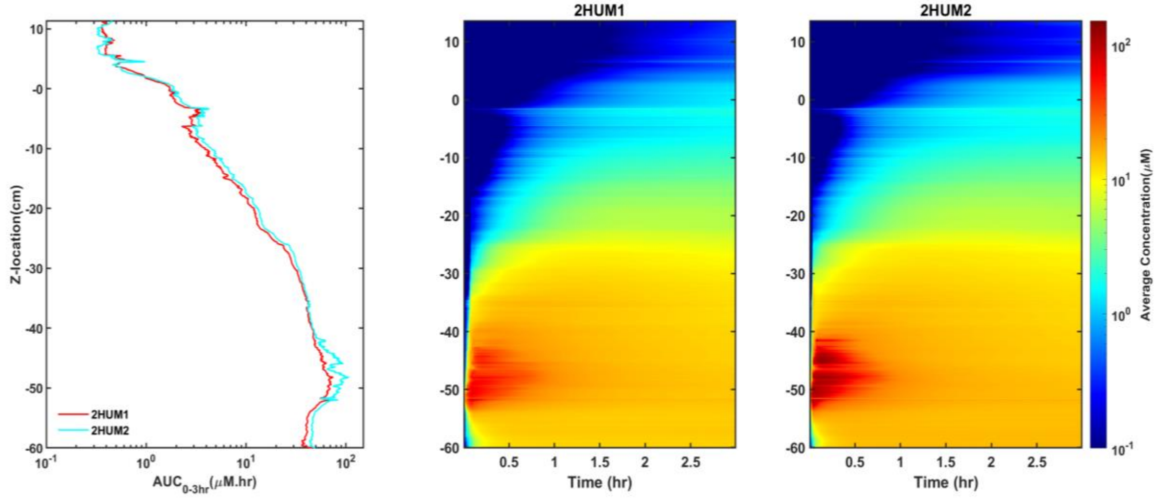

Supplementary Figure 6. Effect of bolus rate by average AUC and spatial temporal distribution comparison. Despite a higher bolus rate, no noticeable differences were observed between 2HUM1 and 2HUM2.

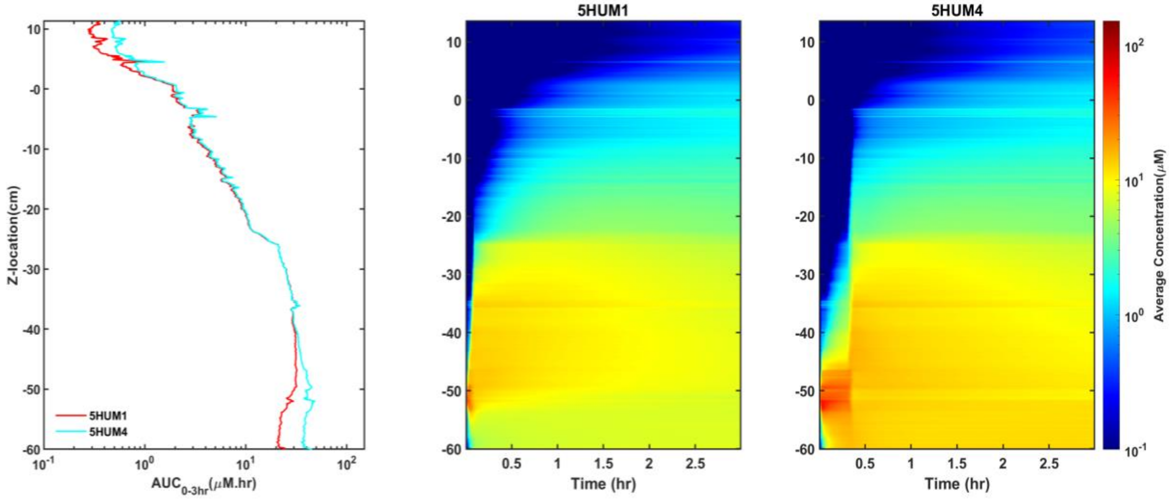

Supplementary Figure 7. Effect of flush timing by average AUC and spatial temporal distribution comparison. The decrease in solute concentration after injection in 5HUM1 is believed to be a result of dilution caused by the large flush volume. While the spatial temporal trends are difficult to compare, the AUC trends indicate little difference in the brain region.

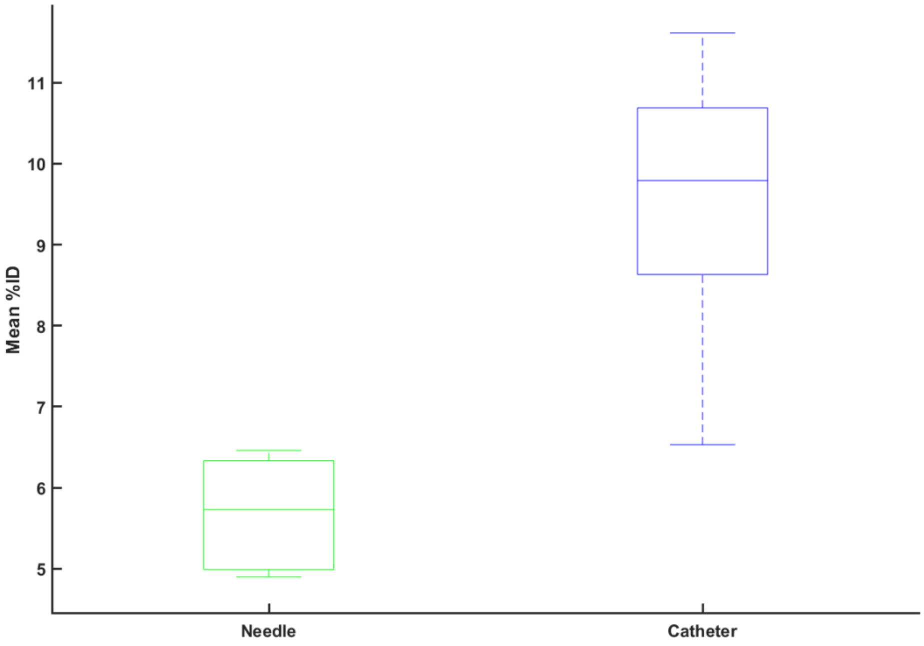

Supplementary Figure 8. Boxplots of the mean lumbar puncture needle and catheter experiments. On average, protocols conducted with a lumbar puncture catheter (3HUM1 – 4HUM2) showed nearly 2X solute transport to the brain when compared to lumbar puncture needle protocols (1HUM1 – 2HUM2).